

University of Windsor

Scholarship at UWindor

Electronic Theses and Dissertations

Theses, Dissertations, and Major Papers

1-1-2007

A MEMS non-planar ultrasonic microarray.

Matthew Meloche
University of Windsor

Follow this and additional works at: <https://scholar.uwindsor.ca/etd>

Recommended Citation

Meloche, Matthew, "A MEMS non-planar ultrasonic microarray." (2007). *Electronic Theses and Dissertations*. 7027.

<https://scholar.uwindsor.ca/etd/7027>

This online database contains the full-text of PhD dissertations and Masters' theses of University of Windsor students from 1954 forward. These documents are made available for personal study and research purposes only, in accordance with the Canadian Copyright Act and the Creative Commons license—CC BY-NC-ND (Attribution, Non-Commercial, No Derivative Works). Under this license, works must always be attributed to the copyright holder (original author), cannot be used for any commercial purposes, and may not be altered. Any other use would require the permission of the copyright holder. Students may inquire about withdrawing their dissertation and/or thesis from this database. For additional inquiries, please contact the repository administrator via email (scholarship@uwindsor.ca) or by telephone at 519-253-3000ext. 3208.

A MEMS Non-planar Ultrasonic Microarray

by

Matthew Meloche

A Thesis

Submitted to the Faculty of Graduate Studies
through Electrical and Computer Engineering
in Partial Fulfillment of the Requirements
for the Degree of Masters of Applied Science
at the University of Windsor

Windsor, Ontario, Canada
2007



Library and
Archives Canada

Bibliothèque et
Archives Canada

Published Heritage
Branch

Direction du
Patrimoine de l'édition

395 Wellington Street
Ottawa ON K1A 0N4
Canada

395, rue Wellington
Ottawa ON K1A 0N4
Canada

Your file *Votre référence*
ISBN: 978-0-494-35054-6
Our file *Notre référence*
ISBN: 978-0-494-35054-6

NOTICE:

The author has granted a non-exclusive license allowing Library and Archives Canada to reproduce, publish, archive, preserve, conserve, communicate to the public by telecommunication or on the Internet, loan, distribute and sell theses worldwide, for commercial or non-commercial purposes, in microform, paper, electronic and/or any other formats.

The author retains copyright ownership and moral rights in this thesis. Neither the thesis nor substantial extracts from it may be printed or otherwise reproduced without the author's permission.

AVIS:

L'auteur a accordé une licence non exclusive permettant à la Bibliothèque et Archives Canada de reproduire, publier, archiver, sauvegarder, conserver, transmettre au public par télécommunication ou par l'Internet, prêter, distribuer et vendre des thèses partout dans le monde, à des fins commerciales ou autres, sur support microforme, papier, électronique et/ou autres formats.

L'auteur conserve la propriété du droit d'auteur et des droits moraux qui protègent cette thèse. Ni la thèse ni des extraits substantiels de celle-ci ne doivent être imprimés ou autrement reproduits sans son autorisation.

In compliance with the Canadian Privacy Act some supporting forms may have been removed from this thesis.

Conformément à la loi canadienne sur la protection de la vie privée, quelques formulaires secondaires ont été enlevés de cette thèse.

While these forms may be included in the document page count, their removal does not represent any loss of content from the thesis.

Bien que ces formulaires aient inclus dans la pagination, il n'y aura aucun contenu manquant.


Canada

© 2007 Matthew Meloche

All Rights Reserved. No Part of this document may be reproduced, stored or otherwise retained in a retrieval system or transmitted in any form, on any medium by any means without prior written permission of the author.

Abstract

A novel discretized hyperbolic paraboloid geometry ultrasonic sensor microarray of capacitive type sensors has been developed to intrinsically provide a broadband constant beamwidth beamforming capability without any microelectronic signal processing. A mathematical model has been developed and verified to characterize the array response. A design methodology has been presented that enables the determination of array dimensions, sensor type, device modeling and behavioral analysis in a straight-forward manner. The developed theory has been used to design two ultrasonic sensor microarrays: one in the 2.3 MHz - 5.2MHz frequency regime and another in the 113 kHz-167 kHz frequency regime. Individual capacitive type sensor elements have been designed using a cross-verification method that involves lumped element modeling, 3-D electromechanical finite element analysis (FEA) modeling, and microfabrication simulation. The sensor microarray has the potential to be used in real-time automotive collision avoidance applications, medical diagnostic and therapeutic applications, as well as industrial sensing.

Dedication

To my Parents, and my Wife

Acknowledgements

First, a large thank-you to my advisor Dr. Sazzadur Chowdhury, without his help this project would not have come to completion.

Thank-you also to Ashkan Hoseinzadeh and Tara Droullaird for assistance with editing.

Andrew Tam, This was your idea. Thank-you.

Alan Castonguay and Dave Addison, thanks guys for keeping me sane and making sure I didn't forget how to have fun.

Contents

| | |
|---|------------|
| Abstract | iv |
| Dedication | v |
| Acknowledgments | vi |
| List of Figures | x |
| List of Tables | xii |
| 1 Introduction | 1 |
| 1.1 Goals | 1 |
| 1.1.1 Background | 1 |
| 1.1.2 Research Goals | 6 |
| 1.2 Target Applications | 7 |
| 1.3 Historical Context | 8 |
| 1.4 Overview of MEMS Fabrication Techniques | 10 |
| 1.4.1 Spin Coating | 10 |
| 1.4.2 Optical Lithography | 11 |
| 1.4.3 Sputtering | 14 |
| 1.4.4 Deep Reactive Ion Etching | 15 |
| 1.5 Packaging Techniques | 16 |
| 1.5.1 Adhesive Bonding | 16 |
| 1.5.2 Wirebonding | 16 |
| 1.6 Fabrication Methodologies | 17 |
| 1.6.1 Embedded Mask Methods for Large Scale Tiered Structures | 17 |

| | | |
|----------|--|-----------|
| 1.6.2 | Hand Assembly for Low Volume, Low Complexity Structures | 21 |
| 1.7 | Physical Application Requirements | 22 |
| 1.8 | Specific Research Objectives | 23 |
| 1.9 | Principle Results | 24 |
| 1.10 | Organization of Thesis | 25 |
| 2 | Non-Planar Beamforming | 26 |
| 2.1 | Theory of Hyperbolic Paraboloid Geometry Acoustical Transducer | 26 |
| 3 | Array Design | 36 |
| 3.1 | Determination of Array Sidelength | 36 |
| 3.2 | Determining the Number of Sensing Surfaces | 37 |
| 3.3 | Array Height and Tier Elevation Calculations | 38 |
| 3.3.1 | Tier Elevation | 40 |
| 3.4 | Step 4 – Sensing Surface Design | 42 |
| 3.5 | Numerical Example | 42 |
| 3.5.1 | Problem Definition | 42 |
| 3.5.2 | Solution | 43 |
| 3.6 | Array Design for IAVSS | 47 |
| 3.6.1 | Problem Definition | 47 |
| 3.6.2 | Solution | 48 |
| 4 | Transducer Modeling | 53 |
| 4.1 | MEMS Acoustic Sensors | 53 |
| 4.1.1 | Piezoelectric Transduction | 53 |
| 4.1.2 | Piezoresistive Transduction | 54 |
| 4.1.3 | Capacitive Transduction | 55 |
| 4.2 | Modeling Levels | 56 |
| 4.3 | Lumped Element Modeling | 57 |
| 4.3.1 | Reliability Study | 62 |
| 4.3.2 | Lumped Element Results | 67 |
| 4.4 | Finite Element Analysis | 69 |
| 4.4.1 | Resonant Frequency | 69 |
| 4.4.2 | Pull-In Voltage | 70 |

| | | |
|----------------------|--|------------|
| 4.4.3 | Capacitance Change Over Actuation Range | 70 |
| 4.4.4 | Maximum Displacement | 71 |
| 5 | Fabrication | 73 |
| 5.1 | Array Fabrication Details | 73 |
| 5.1.1 | Stage 1: Wafer Preparation | 74 |
| 5.1.2 | Stage 2: PVD Metal Deposition | 74 |
| 5.1.3 | Stage 3: Lithography | 75 |
| 5.1.4 | Stage 4: Metal Etching | 76 |
| 5.1.5 | Stage 5: Silicon Etch | 76 |
| 5.1.6 | Stage 6: Photoresist Strip | 78 |
| 5.1.7 | Stage 7: Buffered Oxide Etch Diaphragm Release | 78 |
| 5.1.8 | Stage 8: Array Assembly | 80 |
| 5.2 | Packaging Details | 81 |
| 6 | Conclusions | 84 |
| | References | 87 |
| A | Matlab Code | 91 |
| A.1 | Elevations Vs. Number of sensing surfaces per axis | 92 |
| A.2 | Lumped Element Simulation | 94 |
| A.2.1 | Numerical Example | 94 |
| A.2.2 | Array Design Simulation | 96 |
| A.2.3 | Support Functions | 98 |
| A.3 | Mainlobe -3dB Cross-Section Generation | 103 |
| A.3.1 | Support Functions | 106 |
| A.4 | Accuracy of Summation Vs. Integral form | 106 |
| A.4.1 | Support Functions | 108 |
| A.5 | Generation of Polar Plots | 109 |
| A.5.1 | Support Functions | 110 |
| VITA AUCTORIS | | 111 |

List of Figures

| | | |
|-----|--|----|
| 1.1 | Schematic of Constant Beamwidth Array Based on Synthesis Theory | 5 |
| 1.2 | Block Diagram of the Integrated Active Vehicle Safety System (IAVSS) | 7 |
| 1.3 | Safety Shell | 8 |
| 1.4 | Application of a Photoresist by Spinning | 12 |
| 1.5 | Optical Lithography Machine | 13 |
| 1.6 | Ion Beam Sputtering | 15 |
| 1.7 | Embedded Mask Method: Phase 1 – Mask Deposition | 19 |
| 1.8 | Embedded Mask method: Phase 2 – Pattern Transfer to Wafer | 20 |
| 1.9 | Main Steps to Create a Hand Assembled Array | 21 |
| 2.1 | Hyperbolic Paraboloid Shaped Surface | 28 |
| 2.2 | Beamforming with the Continuous Aperture Sensor | 29 |
| 2.3 | Seven Elevation Discrete Hyperbolic Paraboloid | 31 |
| 2.4 | From Continuous Aperture Transducer to Discrete Array | 31 |
| 2.5 | Main Beam -3dB Cross-Sections of Continuous and Discrete Arrays | 33 |
| 2.6 | Worst Case Passband Approximation Error | 34 |
| 2.7 | 3-D Change in Beamshape over Change in Lambda | 34 |
| 2.8 | Cross-Sectional Changes in Beamshape Over Change in Lambda | 35 |
| 3.1 | Number of Sensing Surfaces Vs. Sidelobe Intensity | 38 |
| 3.2 | Array Height and Out-of-Plane Twist | 39 |
| 3.3 | Discrete Array Height Sampling | 39 |
| 3.4 | Number of Sensing Surfaces Vs. Total Height | 40 |
| 3.5 | Number of Elevations Vs. Number of Sensing Surfaces | 41 |
| 3.6 | Illustration of Numerical Example Array and Geometry Approximation | 44 |

| | | |
|------|--|----|
| 3.7 | Array Beamshape at 2.3 MHz | 45 |
| 3.8 | Array Beamshape at 3.75 MHz | 45 |
| 3.9 | Array Beamshape at 5.2 MHz | 46 |
| 3.10 | Array Mainlobe Cross-Sections at -3 dB | 46 |
| 3.11 | Illustration of IAVSS Array and Geometry Approximation | 50 |
| 3.12 | IAVSS Array Beamshape at 113 kHz | 50 |
| 3.13 | IAVSS Array Beamshape at 140 kHz | 51 |
| 3.14 | IAVSS Array Beamshape at 167 kHz | 51 |
| 3.15 | IAVSS Array Mainlobe Cross-Sections at -3 dB | 52 |
| | | |
| 4.1 | Piezoelectric Actuator | 54 |
| 4.2 | A Schematic View of a Capacitive Sensor | 56 |
| 4.3 | Array Modeling Details: Beamforming Array - Transducer - Diaphragm | 58 |
| 4.4 | Equivalent Circuit Model | 59 |
| 4.5 | Maximum Shear Stress Theory – Safe Area for in Plane Stress | 63 |
| 4.6 | Octahedral Shear Stress Theory - Safe Area for in Plane Stress | 65 |
| 4.7 | Coulomb-Mohr Criteria – Safe Area for Plane Stress | 66 |
| 4.8 | Finite Element Pull-In Voltage Prediction using IntelliSuite | 71 |
| 4.9 | Maximum Displacement | 72 |
| | | |
| 5.1 | Fabrication Material Legend | 74 |
| 5.2 | Stage 1 Fabrication Details. | 75 |
| 5.3 | Stage 2 Fabrication Details. | 75 |
| 5.4 | Stage 3 Fabrication Details. | 76 |
| 5.5 | Stage 4 Fabrication Details. | 77 |
| 5.6 | Stage 5 Fabrication Details. | 77 |
| 5.7 | Stage 6 Fabrication Details. | 78 |
| 5.8 | Stage 7 Fabrication Details. | 79 |
| 5.9 | Stage 8 Fabrication Details. | 80 |
| 5.10 | Wirebonding Bonding Diagram | 82 |
| 5.11 | Cross-Section of Die 1, 2 and 3 Showing Arrangement of Shims | 82 |

List of Tables

| | | |
|-----|--|----|
| 1.1 | Common Wirebonding Processes | 17 |
| 1.2 | Maximum Ultrasound Exposure Levels by Frequency | 23 |
| 3.1 | Beamwidth Control Parameter K Values | 37 |
| 3.2 | Numerical Example – Results | 44 |
| 3.3 | IAVSS Array Design Performance Specifications | 47 |
| 3.4 | IAVSS Array Geometry | 49 |
| 4.1 | Gauge Factors for Differing Materials | 55 |
| 4.2 | 3×3 Array Diaphragm Design Specifications | 67 |
| 4.3 | Lumped Element Modeling Results For 3×3 Array | 68 |
| 4.4 | 29×29 Array Diaphragm Design Parameters | 68 |
| 4.5 | Lumped Element Modeling Results For 29×29 Array | 69 |
| 4.6 | Lumped Element Modeling Results For 29×29 Array | 70 |
| 4.7 | Capacitance Change Analysis | 70 |
| 5.1 | Wirebonding Diagram Details | 82 |
| 5.2 | Die Details | 83 |
| 5.3 | Number of Height Offset Wafers Required | 83 |

Chapter 1

Introduction

1.1 Goals

1.1.1 Background

Frequency independent broadband acoustical beamforming using a MEMS-based ultrasonic sensor microarray that can provide a real-time variable directional sensitivity without microelectronic signal processing can overcome the current limitations associated with ultrasonic ranging, acoustical imaging, etc [1, 2]. In typical one-dimensional or two-dimensional beamforming techniques, arrays of acoustical sensors are used to enhance the acoustical signals coming from a desired direction whereas the signals coming from the other directions are destructively cancelled out. Different beamforming algorithms, such as delay-and-sum, filter-and-sum or FFT-based techniques implemented in microelectronic based signal processing circuitry are used for this purpose. These algorithms differ in complexity, processing time, and real-time implementation issues [3, 4, 5].

The delay and sum beamforming technique applies a fixed time delay to the output of each elements in the array with respect to a reference element (typically the center element in a planar geometry) so the signals coming out from a desired direction are added up co-phasicly whereas signals from other directions are destructively cancelled out. The resulting signal is directionally sensitive. Delay and sum beamforming is limited since the fixed time delays introduced by the delay elements cause the beamforming operation to only be valid at a specific frequency. In order to obtain a wider band of operation, filter and sum beamforming is used. Filter and sum beamforming

replaces the fixed time delay between array elements with phase shifting filters. The phase shifting filters are typically set up to be inversely proportional to frequency. This makes the effective array length a constant multiple of the wavelength, thus yielding a constant response over a wide range of frequencies. Filter and sum beamformers provide additional capability at the cost of vastly more complex implementations than simple delay and sum beamforming techniques.

Due to their superior properties, the bulk of broadband beamforming research effort has been focused on filter and sum beamformers. Combined with digital signal processing, this provides a robust and flexible solution to the need for broadband beamforming. An example of this type of beamforming is the technique detailed in [6], in which several acoustic arrays are overlaid. This allows the relation between the number of transducers and frequency range to be logarithmically related. This technique, known as harmonic nesting, uses bandpass filters so that each subarray contributes only in its optimal frequency range. Here each subarray uses a finite impulse response (FIR) based filter and sum beamformer. This solution is limited as a discrete set of transducers cannot exactly implement a continuous range of aperture sizes. Also design of the elemental filters for each sensor element of each subarray is a challenging problem. This solution and its variants require significant processing power to be implemented, adding to system cost, complexity and power requirements.

The time delay associated with intensive processing requirements limits the use of such beamformers in applications where real-time implementation issues are crucial. An example of one of these applications is proximity detection for automotive collision avoidance systems. In [7], it has been determined that ultrasonic sensors can be part of an integrated automotive collision avoidance system along with other sensing schemes, such as radar, laser, and vision-based proximity detection systems.

Conventional delay-and-sum beamforming, filter-and-sum-beamforming or FFT based beamforming can also provide a beamsteering capability by progressively altering the phase angle, at the cost of additional signal processing functions, and consequently more hardware [3]. Since the width of the main beam is inversely proportional to the frequency, implementation of constant beamwidth broadband (in other words frequency independent) beamforming is a major technological challenge. Often, additional signal processing is necessary to realize a reasonably constant beamwidth for a desired frequency range at the expense of higher processing delay and memory overheads [6]. Recent progress in high performance MEMS-based acoustical sensors and single die sensor microarrays has eliminated the problem of sensitivity and frequency response mismatch that are common in arrays constructed with discretely manufactured acoustical sensors [8].

In the recent years, significant progress has been made in the design of MEMS-based acoustical sensor microarrays, both in the audio frequency and ultrasonic domain [9, 10, 11, 12]. A planar, uniformly spaced MEMS acoustical sensor microarray is presented in [13]. In this design the array features rear-vented capacitive elements to attain high sensitivities in the audio frequency range. This 3×3 array targets hearing aid instruments as an application and has an operating frequency range of 350 Hz – 18.0 kHz. Each square sensor element has a side length of 1.2 mm and a sensitivity of 10.2 mV/pa. The array uses polysilicon-germanium (Poly-SiGe) for a diaphragm material to enhance sensitivity.

Curved arrays have been well accepted into the medical diagnostic field. Approximately half of all diagnostic ultrasound heads are curvilinear [14, 15]. A commercially produced curvilinear MEMS-based ultrasonic array is presented in [14] which uses a 128 element convex geometry array. The substrate is thinned to $150\mu\text{m}$ through chemical etching and mechanical abrasion. This thinned wafer is flexible enough to be mounted to a fixed backplate which maintains the radius of curvature desired for the head. It has been shown experimentally that the effects of this substrate bending do not significantly affect the performance of the transducer array. The curvilinear sensor array has a center frequency of 4.0MHz and a bandwidth of 125% . Fabrication challenges abound for these arrays however. Extreme care is needed to model the stress in the silicon substrate during bending. Fabrication parameters must also be tightly controlled to ensure that residual stresses and film quality is consistent. Care is needed during handling and assembly to ensure that localized stresses do not cause the device to fracture. In addition, the tolerances on the backplate used to hold the array shape must be manufactured to within 0.01mm of the desired radius of curvature. Also, the offset between the transducer and the plastic nose piece is adjusted to within $7.5\mu\text{m}$ [14]. The high performance of these devices shows that the technology is able to deliver excellent results, although this method of generating a convex surface is highly challenging, causing reduced yields, and increased pricing. These arrays feature a good bandwidth, but still require an external beamforming engine to produce a coherent beam.

Shaped transducers are another practical solution which has been widely adopted in medical imaging applications. The design of an annular ring array has been presented which uses sealed piezoelectric microshell transducers. Flat elements store the majority of the energy in bending stresses. Microshell transducers take advantage of the fact that rounded structures are able to contract and expand in an almost purely tensile or compressive mode. Less energy is stored in bending, resulting in larger membrane displacements. This larger displacement translates into lower driving voltages in transmit mode, and higher sensitivities in receive mode [16].

Peizocomposite based curved arrays are available as a competing technology. Advances in piezoelectric materials have maintained this technology as mainstay in ultrasonic transducers [17].

Frequency independent constant beamwidth beamforming (FICBB) capability is highly desirable in directional speech acquisition, sonar, acoustical ranging, automotive proximity detection systems, acoustical imaging, and many other applications [6].

Only a few algorithms are available in the literature that can be used to provide a frequency independent constant beamwidth with a planar array geometry; however, they seem to be computationally expensive while real-time implementation is a concern. Additionally, it appears that integration and packaging of the sensor microarray with additional microelectronic circuitry necessary for FICBB is challenging in terms of extra die space and low-loss interconnection paths. Thus, there exists a need to investigate other techniques that could be used to minimize related circuitry. One of them is exploiting the geometrical properties of a surface that can intrinsically enable a beamforming capability.

It has been established that a continuous aperture hyperbolic paraboloid shaped transducer exhibits an intrinsic property of constant beamwidth frequency independent beamforming [18, 19]. The design was realized in macroscale and experimental results were presented. However, obtaining an accurate curvature requires very tight tolerances during the manufacturing process. More critically, maintaining a constant air gap over a curved surface proved to be a formidable challenge.

The state-of-the-art micro-fabrication technology is able to support micrometer scale tolerances and also can maintain uniform air gaps. However, micro-fabrication is a planar process and current micro-fabrication techniques are not suitable to realize curved surfaces such as a hyperbolic paraboloid. Investigation shows that this issue could be resolved by fabricating a tiered geometry using planar process steps that can approximate a discretized hyperbolic paraboloid surface. This is highly desirable as long as the desired operating frequency range is within the limit imposed by the geometric approximation.

The basic concept of intrinsic beamforming finds its root on two independent lines of thinking. One of them is the synthesis method and the other is based on the ray theory. The synthesis method is shown graphically in Figure 1.1.

In this method a number of basic $\frac{\sin(x)}{x}$ patterns which have been displaced using delay lines are superimposed in space. The centers of the superimposed beam patterns are displaced in space by an amount which increases linearly with frequency in such a way that the array response widens at the same rate that the angular beamwidth decreases. If an infinite number of strip arrays were distributed on a surface in such a manner that the time delay at the extremities increased linearly as

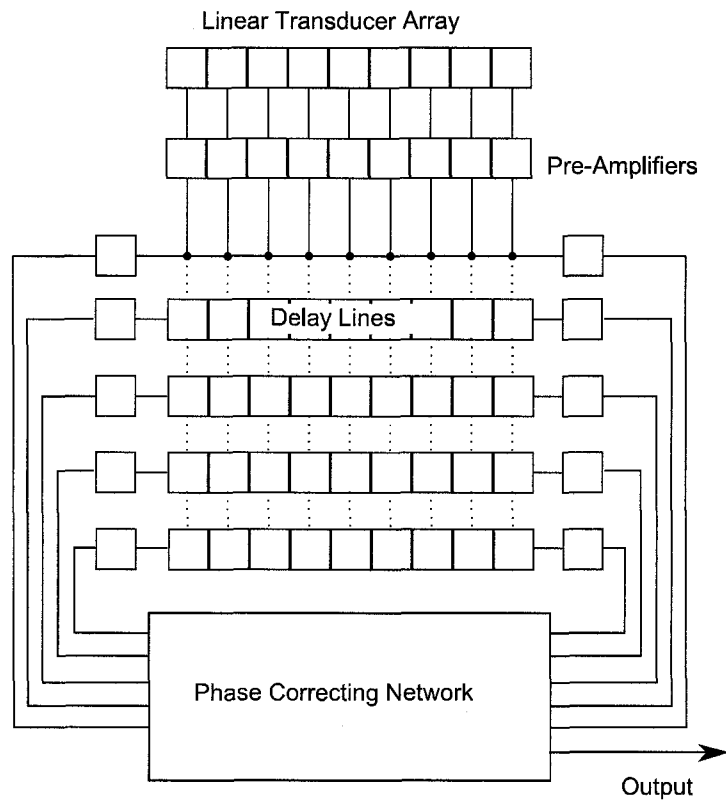


Figure 1.1: Schematic of Constant Beamwidth Array Based on Synthesis Theory

we proceed from one end of the surface to the other, then the resulting surface in three dimensions would be a hyperbolic paraboloid. A constant beamwidth broadband beamformer can be achieved through this technique. An additional feature is that the geometry is symmetric along the axis of twist, as well as along the axis at a right angle. The bandwidth ratio over which the array will operate is a function of the number of strips in the array [19, 20]. It appears that this characteristic can be exploited successfully to realize a discretized hyperbolic paraboloid surface with a desired bandwidth.

The same array can be developed by using the ray theory. If it is required to have a beamwidth of 2α , which is independent of frequency, we can consider a linear strip array having a length much greater than the wavelength. This array will have a very narrow beamwidth in the direction normal to the array. By placing a series of strip arrays so that the direction of the nominal array normal gradually varies from $-\alpha$ to $+\alpha$, a beamwidth of 2α could be achieved. If the angle of the twist is varied linearly as the surface proceeds along the axis of rotation, the resulting surface would be a linear twist.

Comparing the linear twist to the hyperbolic paraboloid, it has been shown that for the linear twist, the angle of deflection of a straight line on the surface is directly proportional to the distance traveled along the twist axis [19]. For the hyperbolic paraboloid, it is the tangent of the angle of deflection which increases linearly with distance travelled along the axis of twist. For angles less than 10° the tangent and its angle in radians are approximately equal. Therefore, for small angular twists, the two surfaces are identical and the complete beamshape could be calculated using the mathematics for either geometry. The hyperbolic paraboloid is chosen as it is a doubly ruled quadratic surface and can be constructed entirely out of straight lines.

1.1.2 Research Goals

Based on the review of the state-of-the-art in beamforming acoustical sensor arrays in terms of geometry, capability, limitations, and challenges as presented in the preceding section, the overall goal of this thesis has been set to develop a MEMS-based non-planar constant beamwidth broadband ultrasonic beamforming sensor microarray. The microarray is to be able to intrinsically provide broadband constant-beamwidth beamforming capability allowing the elimination or reduction of processing overhead from a microelectronic beamforming engine. Specifically, the hyperbolic paraboloid geometry will be explored to realize a non-planar array of ultrasonic sensors that can be fabricated using the current state-of-the-art MEMS technology.

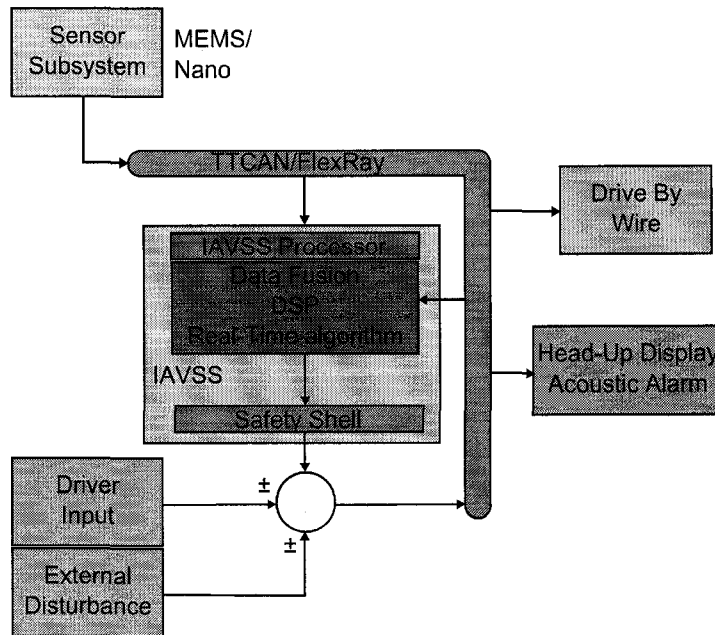


Figure 1.2: Block Diagram of the Integrated Active Vehicle Safety System (IAVSS)

1.2 Target Applications

The developed sensor microarray could be used for high frequency ultrasonic imaging applications or as an enabling sensor system for the integrated active vehicle safety system (IAVSS) as proposed in [7]. The IAVSS system includes a MEMS sensor subsystem, a controller, Drive-by-Wire subsystems, Vehicle network subsystem (TTCAN or FlexRay), and a Driver interface subsystem (head-up display/ acoustic alarm) as shown in Figure 1.2

The IAVSS subsystem compares any driver input or external disturbance as shown in Figure 1.3 with the safety shell parameters stored in the IAVSS memory. The system maintains the safety shell by compensating for any erroneous driver input or an emerging threat due to an external disturbance such as an approaching vehicle. The IAVSS has the ability to autonomously control acceleration, braking or steering (e.g. lane change or road side stop). This is necessary to avoid a collision if the driver fails to act in time or to minimize the damage during a collision by activating passive safety mechanisms such as steering wheel collapse, adjusting seat-belt tensions or to stop the fuel pump. In a post collision state the system can unlock doors and or lower windows depending on external environmental conditions to aid egress. Additionally the system could automatically engage the vehicles hazard lights as well as call 911 based on the severity of the impact.

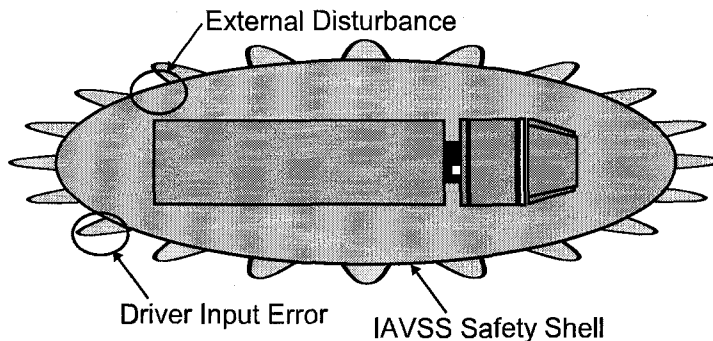


Figure 1.3: Safety Shell

The system is fundamentally different approach from other safety systems where the components work individually without any central processor taking care of vehicle safety [7]. The system has the potential to enable safe autonomous driving in the future in almost any driving scenario. One major challenge to implement IAVSS is the time delay associated with the implementation of the varied and complex algorithms as mentioned in National Highway Traffic Safety Administration (NHTSA) Report to process sensor data, threat level estimation and decision making [21]. The challenge could be better addressed by minimizing the use of complex algorithms for signal processing. The current need for these expensive algorithms indicates an area in need of improvement through the elimination of the time delay associated with conventional ultrasonic beamformers. In order for the system to obtain maximum information for decision making, frequency independent broadband beamforming is necessary. The implementation of a beamforming engine is a processor intensive operation. In order to minimize the amount of processing required, the sensing element should be able to provide this functionality intrinsically.

1.3 Historical Context

The first ultrasonic wave propagation is credited to Paul Agevin in 1917 when he transmitted ultrasonic waves in sea water [22]. However, earlier experiments and theoretical development had been ongoing since the mid 1800's with the discovery of magnetostrictive effects by J. P. Joule [22]. His results are summarized in a paper dated 1847 where he shows that a magnetic field applied to a bar of iron produces an increase in length of the bar. Nickel provides a stronger effect, while nickel chromium alloy was the most commonly used material. The first application for ultrasonics, and indeed, for many years the only application was the production of sound waves for the detection of

submarines. This work was pioneered in the First World War due to the effectiveness of German submarines at disrupting Atlantic trade [22]. Professor Paul Langevin used the piezoelectric effect to create the world's first underwater ultrasonic transducer, a quartz crystal transducer operating at 50 kHz. Unfortunately, development of the transducer was not completed until after the First World War. It is interesting to note that the initial application for this device was depth metering.

During the Second World War, ultrasonic transducers were improved by the discovery of Ammonium dihydride phosphate (ADP). ADP crystals proved to be far more suitable than the Rochelle salt piezoelectric crystals that had been used to this point. During this period, ultrasonic systems had matured to be effective at finding submarines, as well as being miniaturized enough to be mounted on torpedoes like the 'mine mark 24' [22]. These torpedoes could be launched from a submarine or airplane, and were capable of tracking a target as far away as 200 yards. Ultrasound detection and tracking proved to be a critical technology for defence against submarine based warfare. Other applications stemming from research during World War II included moving target indicator radar, where static reflections were cancelled only showing moving targets. These systems were implemented using ultrasonic delay lines to store previous scan data. 1924 saw R. W. Wood and A. L. Loomis examining the effects of high-intensity ultrasound. They were able to show many striking effects produced by high intensity ultrasound, however they remained laboratory demonstrations [22]. The second practical application of ultrasound technology was for defect detection in materials, an application that remains common today. This technology was developed independently during the Second World War in both America and Britain. During this period the first medical diagnostic applications were also developed; it was discovered that ultrasound could be used to detect cancer [22].

During the 1940's and 1950's medical applications for ultrasound underwent slow development, but during the 1960's it began to see increased clinical use, burgeoning and becoming a mainstream diagnostic and therapeutic treatment during the 1970's. Several paradigms of ultrasonic imaging are possible. A-Mode, ultrasound uses a simple time based display and allows for position measurement and dimensioning of the observed structures. B-Scan instruments couple an A-mode unit to a beam-scanning apparatus and an intensity modulated display to produce a 2-D cross sectional image of the area under inspection. This is the most common form of diagnostic ultrasound today. Finally M-Mode ultrasound uses a standard A-Mode instrument with a modified display. This allows positional monitoring of moving structures such as artery walls and heart valves [23].

Today ultrasound is well established in industry in many applications such as cleaning, defect detection and ranging. Ultrasonic cleaning uses ultrasonic waves injected into a solvent bath to

ensure removal of adhered contaminants. This technique is used in a wide range of applications; from cleaning jewellery to de-griming automotive parts to cleaning surgical implements. Ultrasonic waves can be used to detect voids in a material [24]. This ability allows for non-destructive testing for material or weld defects. Ultrasound is also able to detect changes in density. This allows the accurate measurement of coating thicknesses. Each layer can be characterized for thickness independently after all layers are deposited. This is used for quality control for automotive paint. It can also be frequently used to detect if a body panel has been repainted, as the thickness profiles will be notably different. The original application for ultrasound was ranging, and ultrasonic range sensing continues to see development. Ultrasonic range sensing allows accurate non-contact distance measurements. This sensing can be used in some applications where other non-contact sensing mechanisms such as laser cannot be used. For example level measurement in reservoirs of molten metal used for casting. Ultrasound continues to find new applications in industry, and the availability of MEMS ultrasonic sensing promises to ensure new applications continue to be found.

1.4 Overview of MEMS Fabrication Techniques

MEMS fabrication began in the early 1960's. The first commercial sensor fabricated by what is now considered MEMS techniques was produced by Honeywell in 1962 [25]. Micromachining techniques have been developing rapidly in recent years, and the variety of geometries that can be manufactured continues to grow; as does the number of materials available. The major techniques needed to fabricate the developed discretized hyperbolic paraboloid acoustic sensor microarrays and the techniques needed for assembly of the IAVSS sensor microarray are outlined in the following sections.

1.4.1 Spin Coating

Spin coating is a technique used to apply both temporary materials such as photoresist, and permanent structural materials. Spinners are found in all microfabrication labs. The spinning process can be used to deposit viscous materials over wafers without extreme topologies. Due to poor adhesion between photoresist and metals, PSG and polysilicon, wafers are typically 'primed' with Hexamethyl disilazane (HMDS) before the application of a photoresist. A primed wafer features a hydrophobic surface, which ensures that surface moisture on the wafer will not interfere with photoresist adhesion.

The priming process begins by baking the wafer. HMDS vapor is applied to create a monolayer on the wafer surface. An additional benefit of priming the wafers with HMDS prior to the application of a photoresist is the elimination of the effects of environmental humidity variation. Once the wafer

is primed, resist is applied to the center of the wafer at approximately 300 RPM (Figure 1.4.A). The spinner then rapidly accelerates to its final spin speed. This evenly spreads the resist across the wafer surface (Figure 1.4.B). Finally the spinner maintains the final spin speed for a short interval of time, typically around 1 minute (Figure 1.4.C) to allow the solvent in the resist to begin evaporating.

The main parameters for determining the thickness of the deposited film is viscosity, solvent evaporation rate and spin speed. A laboratory spinner is typically capable of speeds up to 10 000 RPM, with an accuracy of ± 1 RPM. This level of control is necessary as a 50 RPM variation from the set point can result in as much as a 10% thickness variation. Typical resist thicknesses are in the range of $1\mu\text{m}$, although this technique can be used to apply films with thicknesses between $0.1\mu\text{m}$ and $500\mu\text{m}$. At a μm thickness, spin application can obtain a film thickness uniformity of $\pm 5\text{nm}$ across the wafer. Spin speed can be used to vary the film thickness over 1 decade (ie. from $1\mu\text{m}$ to $10\mu\text{m}$); beyond this limit, a new resist formulation must be used [26, 27].

1.4.2 Optical Lithography

Optical lithography is, in its essence, photography and consists of 4 major steps:

- Photosensitive film (photoresist) application
- Alignment of mask and wafer
- Exposure of photoresist
- Development of patterns

After application of the photoresist through a spin procedure, the photomask – the photographic analog of a negative – is aligned with the wafer. Exposure to UV light causes a change in the solubility of the photoresist, allowing it to be selectively removed. The patterned resist can be used as an etch mask. Photoresist is generally not used as a structural material and is removed by an oxygen plasma ashing technique after etching is complete. Two critical factors are considered in determining the complexity of the pattern that can be transferred using these techniques: the resolution of the alignment machine, which is limited by the optics in use and diffraction at the mask edges; and the ability to accurately overlay successive patterns. In order to improve the resolution of an optical lithography system, a second optical system serving as a reducer may be used. Typical reducers operate between 4x and 10x magnification [26, 27]. A typical optical lithography system is shown in Figure 1.5.

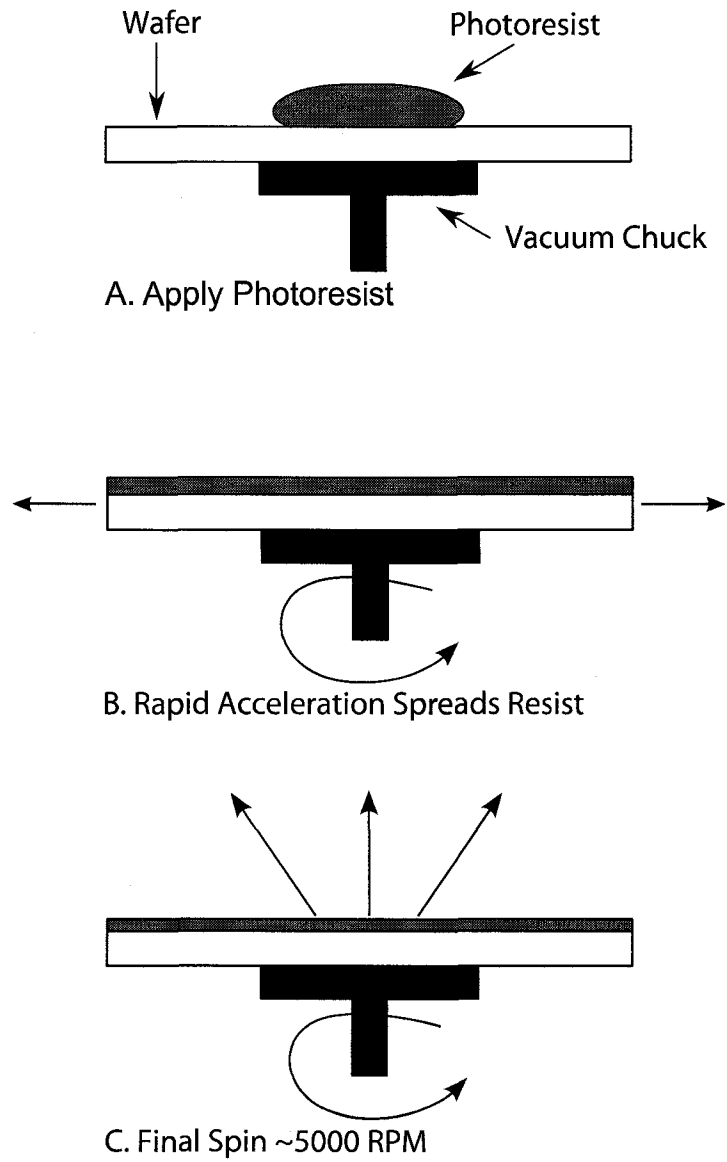


Figure 1.4: Application of a Photoresist by Spinning

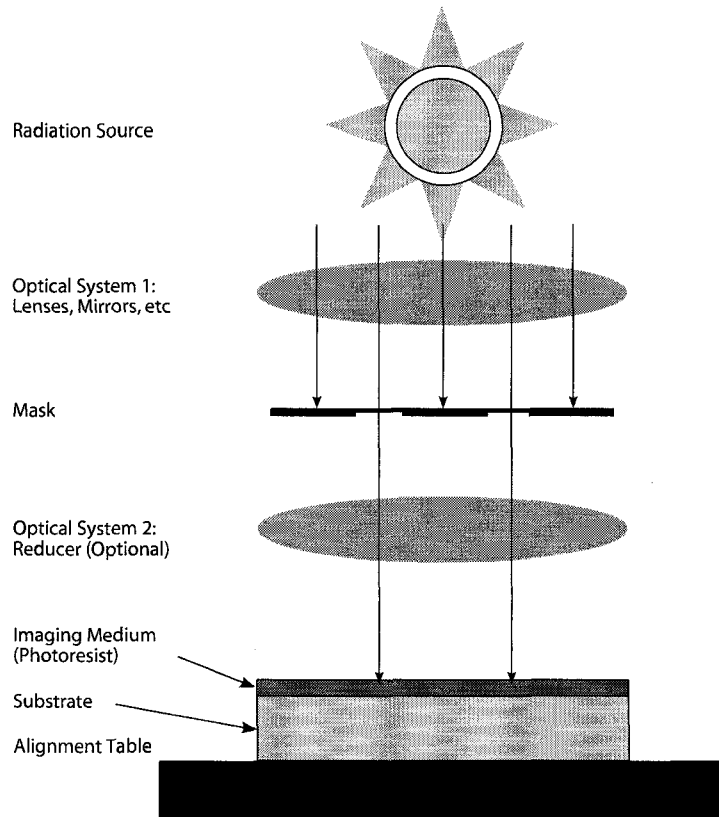


Figure 1.5: Optical Lithography Machine

1.4.3 Sputtering

Sputtering is a commercially important technique for thin film deposition. This technique is used to apply films to computer disks, liquid crystal displays, compact discs and hard-drives for computers. It is also used to apply hard coatings to cutting tools, gears, and automotive parts [27]. Sputtering is a type of physical vapor deposition and as such material is transferred directly from a source material target to the wafer. During sputtering, the source material target is charged to a high negative potential. It is then bombarded with positively charged ions from argon plasma. The target material is ejected from the source mainly by momentum transfer from neutral atoms. Ejected surface atoms are deposited onto a substrate (the wafer) placed on the anode. In order to maximize the yield of the process, ion energies in the range of 500–3000 Volts are used. Due to the large ion energies present, the deposited material is able to penetrate 1 or 2 atomic layers into the substrate, producing extremely strong adhesion. In order to sustain a DC plasma a relatively high pressure of 1×10^{-2} Torr or greater is needed. At 10^{-1} Torr, the mean-free path of the sputtered ions is approximately 1mm. Because of the multiple collisions of the atom between release and arrival, the atoms arrive at random incidence angles. This leads to excellent step coverage compared to other physical vapor deposition techniques.

A relatively recent variation called ion beam sputtering provides both excellent adhesion and a high purity deposition. The operating pressure for this technique is approximately 1×10^{-4} Torr. In this layout, an ion beam as shown in Figure 1.6 with an energy in the hundreds to thousands of electron volts (eV) is directed at the sputtering target. Both reactive and inert gases can be used for ion beam sources. The substrate is suitably located as to be isolated from the plasma generation source, this permits independent control over the substrate temperature, gas pressure and type of particle bombardment of the growing film. It is also possible to control the energy and target current density independently. Limitations of this technique include a deposition rate that is lower than traditional sputtering techniques and a relatively small deposition area.

A third variation of sputtering is Pulsed DC Sputtering. This variation features high plasma densities and deposition rates. The pulse frequency can be adjusted in the range of 25kHz to 250kHz (with an ENI RPG power supply). It does not suffer from arcing like DC sputtering and it can be used to deposit dielectric materials like RF sputtering. This method provides long term process stability, high plasma densities and high deposition rates [27, 28].

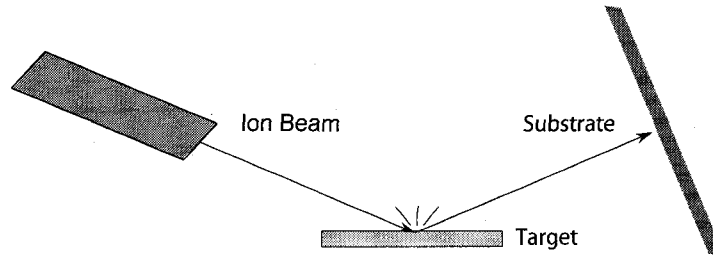


Figure 1.6: Ion Beam Sputtering

1.4.4 Deep Reactive Ion Etching

Reactive ion etching (RIE) of silicon is a well-established tool for IC fabrication and has been indispensable since the early 1980's. Deep Reactive Ion Etching (DRIE) is a specialized inductively-coupled-plasma reactive-ion-etch (ICP-RIE). DRIE overcomes several of the limitations of traditional RIE by improving the etch rate, selectivity against photoresist and SiO_2 , and the maximum aspect ratio. One of the common DRIE techniques is the Bosch DRIE. The Bosch process DRIE involves alternating between two stages. In the first stage, a thin fluorocarbon polymer film is deposited. This film acts as a protective layer for the sidewalls during the etch stage. The polymer is constructed of CF_2 molecules deposited from a C_4F_8 gas source. The second stage involves a highly directional anisotropic etch. In this stage SF_6^+ ions generated from SF_6 gas acts as an etchant. Since the particles impinge primarily perpendicularly to the wafer, the protective CF_2 layer is quickly removed along the bottom of the area to be etched, while it remains intact along the sidewalls.

The etch rate selectivity for a DRIE process is excellent. Etch selectivity between silicon and SiO_2 is 1000:1 and between silicon and photoresist is 250:1. This makes possible the ability to etch $300\mu\text{m}$ deep to over $500\mu\text{m}$ deep features in a reasonable amount of time. Another significant advantage of this process is its compatibility with both CMOS and bipolar IC processing when used in conjunction with silicon fusion bonding. A limitation of this technology is the aspect ratio dependence of the etch rate. The etch rate is diffusion-limited and drops significantly for narrow trenches. Modification of the process parameters can only partially counteract these effects [29, 26].

1.5 Packaging Techniques

1.5.1 Adhesive Bonding

Adhesive bonding of a die to a package or another die may be accomplished by depositing a film of epoxy thermoset, acrylic thermoplastic or silicone resins between the layers [30]. Although the thermal and electrical conductivity of this technique are inferior to other methods of mounting, by loading the adhesive material with silver particles the electrical and thermal conductivities of the bond can be controlled over a wide range. Adhesive bonding is a low-cost technique that lends itself easily to automation. Additional cost savings can be obtained since metal plating on bonding surfaces is unnecessary. Due to the plastics used, a low curing temperature is necessary; unfortunately these plastics also need time to outgas, and are also subject to voids. Due to the elastic properties of the bonding material, the stress in the die is reduced. The material can also be removed to allow rework of the device if necessary. Due to the nature of the bonding materials used, these devices are not suitable for use in harsh environments, and the bonding material may require special low-temperature storage of less than -40°C and mixing before use. Adhesive bonding is used for the IAVSS array design due to the ease of integrating a large number of dies into a single package [30].

1.5.2 Wirebonding

Wirebonding uses thin wires to connect bond pads on the die to the packaging interconnects. The attachment process uses a combination of heat, pressure and ultrasonic energy. The result of the bonding is a weld consisting of either electron sharing or diffusion of atoms at the bond site. Pressure during the bonding ensures intimate contact between the wire and the pad, as well as helping to break up any oxide layer or contamination present at the interface. The presence of ultrasonic energy during the bond further increases the ability to breakup the oxide or contaminants. The use of heat accelerates the process of atomic diffusion, reducing the amount of time necessary to form a connection [27]. Two distinct processes are available for wirebonding; ball and wedge. Ball bonding commonly uses gold wire less than $75\mu\text{m}$ thick. Gold is used because it deforms readily under pressure and temperature while maintaining resistance to oxide formation. Gold also remains inert after bonding, and as such, does not require hermetic sealing to prevent corrosion of the bonding wires. Ball bonding techniques require a larger bonding pad pitch of at least $100\mu\text{m}$. Wedge bonding only requires a bonding pad pitch of $50\mu\text{m}$, and is able to use both aluminum and gold wire. Wedge bonding also uses pressure, heat and ultrasonic energy to create the connection. Wedge bonding tends to be slower than ball bonding, but is more common due to its compatibility with aluminum

TABLE 1.1: COMMON WIREBONDING PROCESSES

| Bonding Process | Technique | Temp (°C) | Wire | Pad | Speed (Wires/Sec) |
|-----------------|--------------|-----------|--------|--------|-------------------|
| Ball | Thermo-Sonic | 100–150 | Au | Al, Au | 10 |
| Wedge | Thermo-Sonic | 100–150 | Au, Al | Al, Au | 4 |
| Wedge | Ultrasonic | 25 | Al | Al, Au | 4 |

wires. The aluminum wire can be processed at room temperature without the need for precious metals, greatly reducing the cost. An overview of the bonding techniques is given in Table 1.1 [26].

1.6 Fabrication Methodologies

MEMS fabrication techniques are many and varied. Very tight integration of sense electronics and mechanical components is possible. However, the non-recurring engineering cost associated with a highly integrated design is significant. For designs with millions of units per year created, these solutions offer the lowest cost per unit, making them desirable. For small production runs, prototyping and proof of concept designs, the large investment of time and money needed to create a working device is prohibitive. For these applications other techniques can be used. A system-in-package (SIP) approach places multiple dies within a single package including sense electronics while removing the complexity introduced by on die MEMS-CMOS integration. For low-volume production of multi-die designs, hand assembly is still used commercially. Two techniques are shown below that detail how array assembly may be accomplished for a large scale production and for low-volume design.

1.6.1 Embedded Mask Methods for Large Scale Tiered Structures

In order to achieve performance requirements, a relatively complex structure consisting of 10 or more unique elevations are often required. More complex arrays quickly out pace the ability to perform hand assembly during post-processing. A monolithic fabrication technique is required to first create the tiered structure, and then deposit the diaphragms directly in place. Embedded mask methods can be used to create complex tiered structures of arbitrary complexity [31, 32]. One method suitable for use with the tiered geometry required for the array is an Aluminum Delayed Mask Process (Al-DMP). The Al-DMP process presented in [31] is capable of producing multi height structures with vertical or slanted sidewalls. The DMP process involves using layers of negative photoresist and

aluminum to deposit the masks for each elevation before any etching of the structure occurs. The variation in height between each elevation is a limitation of the reactive ion etch (RIE) equipment in use. The Al-DMP process involves the following steps to create the masks:

1. Deposit 200 nm of Al and pattern
2. Pre-bake at 200°C and deposit negative photoresist
3. Develop and hardbake
4. Deposit 200 nm of Al and pattern

Steps 2–4 of the deposition process are repeated as necessary to build the total number of masks required for the process. This process is shown graphically in Figure 1.7.

Once all the masks required are in place, a second processing phase transfers the pattern to the wafer. The etch process takes the following steps:

1. Ashing of exposed resist using Al mask
2. Deep ICP-RIE etch of exposed wafer
3. Al etch to remove mask layer
4. Ashing of exposed resist

Steps 2–4 of the etch process are repeated as necessary to etch all layers. This process is shown graphically in Figure 1.8. This process can be enhanced by placing a single layer of SiO₂ under the bottom Al layer. This SiO₂ layer provides protection for the structure against damage from Al pinholes when etching deep structures.

The process uses RIE loop counting and metrology to determine etch depths at each etch stage. This can yield excellent depth control and uniformity. The presented process provides a method of creating highly complex, multilevel tiered structures with vertical sidewalls suitable for use with the tiered array geometry produced by a hyperboloid paraboloid array. Capacitive sensors can be deposited on the surfaces created by the Al-DMP process. Standard techniques for the creation of thin film diaphragms can be used for the creation of the capacitive sensors. This allows for the monolithic creation of the complete sensing array. This technique is well-suited to volume manufacturing, but requires precise and complex process control to ensure all etching and deposition steps are within the necessary tolerances. For low-volume or prototyping applications alternative fabrication techniques may be more suitable.

Deposition of Aluminum and
Lithography



Apply, Expose and Hardbake Negative
Photoresist



Deposition of Aluminum and
Lithography

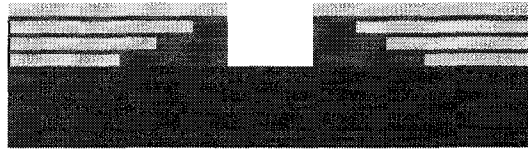


Repeat Al Deposition and Negative
Resist Layers as Required

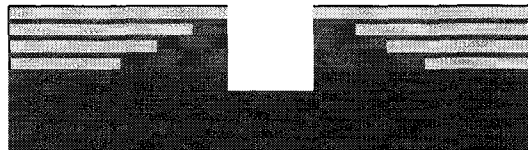


Figure 1.7: Embedded Mask Method: Phase 1 – Mask Deposition

Ashing of Exposed Photoresist Using
Aluminum Mask as Etch Stop



Deep Reactive Ion Etch (DRIE) of
Silicon Wafer



Aluminum Etch



Ashing of Exposed Photoresist



Repeat DRIE, Aluminum Etch
and Ashing for Each Layer



Figure 1.8: Embedded Mask method: Phase 2 – Pattern Transfer to Wafer

1.6.2 Hand Assembly for Low Volume, Low Complexity Structures

Hand assembly of the array from individual sensing surfaces provides a method for manufacturing low volumes of relatively simple arrays. In this method, all sensors are manufactured on a standard SOI wafer (Figure 1.9.A). By using an appropriate SOI wafer, the fabrication requires only a single mask. Optical lithography is used to transfer the etch mask to the wafer. A Bosch DRIE etch is performed to selectively expose the sacrificial SiO_2 . The wafer is then submerged in BOE to release the diaphragms (Figure 1.9.B). After diaphragm release, the wafer is diced into individual sensing surfaces (Figure 1.9.C). These sensing surfaces are assembled manually by using techniques well-established in system-in-package fabrication (Figure 1.9.D). ‘Dummy’ wafers can be used to provide fixed height offsets and therefore very accurately control the out-of-plane tolerances. Mechanical tolerances in the out-of-plane axis can be controlled within $5\mu\text{m}$. Conductive epoxies are used to ensure ground plane connectivity during assembly. By using conductive epoxies, fabrication is vastly simplified as there is no longer a need to create metalized ground pads on the top of the wafer while avoiding the necessity of to wirebond to the bottom of the wafer.

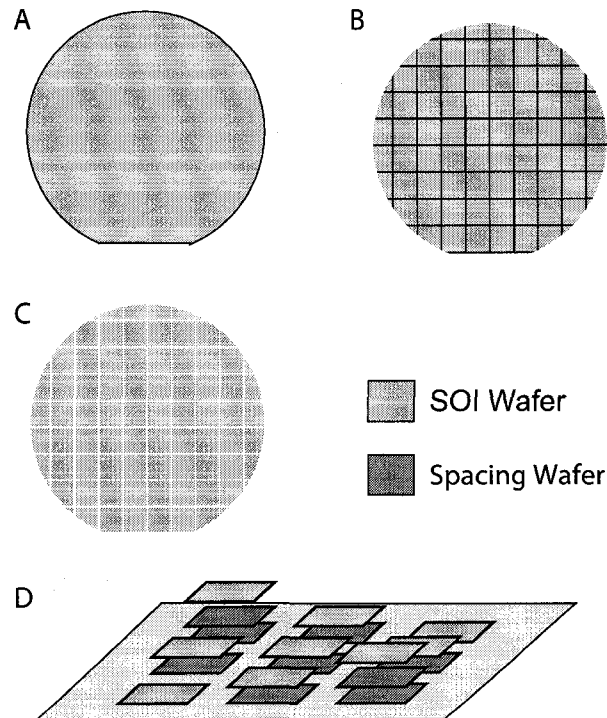


Figure 1.9: Main Steps to Create a Hand Assembled Array

1.7 Physical Application Requirements

In 2005 the NHTSA mandated the use of advanced airbags in all new motor vehicles sold in the USA. Critical to an advanced airbag system, are sensors and processing electronics to allow for automatic and tailored airbag deployment based on seat occupancy. These systems must be able to determine the contents of a seat between Adult passengers, cargo, child safety seats and empty seats. This information would allow the airbag to be automatically disabled if the seat was empty, occupied by a rear facing child safety seat or the passenger was seated too close to the airbag for safe deployment. The criteria for designing these systems also apply to an external collision avoidance system:

- The selected frequency and pressure should not affect humans or animals likely to be in proximity to a vehicle equipped with the system.
- Natural and artificial sound sources encountered while driving should not interfere with system operation.
- Vehicle crash sounds should not interfere with sensor operation.
- Ultrasound frequencies should be chosen to minimize signal attenuation in the media and maximize reflection from the target to allow a large signal to noise ratio (SNR) enabling accurate classification.

Hearing range data for many species was evaluated as well as human exposure limits. Cats and mice have some of the highest known hearing frequencies at 91 kHz and 100 kHz respectively. Consequently frequencies over 100 kHz are desirable for these applications. Ultrasonic energy guidelines are defined separately for air-coupled and contact ultrasound. For air-coupled ultrasound, the two most plausible mechanisms for non-auditory effects are heating and cavitation. It has been reported that cavitation requires sound pressure levels (SPL) above 190 dB. Harmful effects will occur in humans for sound levels above 155 dB SPL. Current Canadian guidelines for continuous exposure to ultrasonic energy are listed in Table 1.2. The Canadian guidelines specify that for occupational exposure, the level must never exceed 137 dB under any circumstances [33].

The evaluation of frequency interference based on natural and artificial sources shows that air compressors, shotguns, sirens and keys jingling can produce high frequency interfering signals up to 120 kHz [34]. These sounds tend to have driving amplitudes below 70 dB SPL. This interference should not render the system inoperative. Evaluating the system for car crash frequency response shows a single peak acoustic pressure of 94 dB SPL, with an average below 80 dB SPL. For lower

TABLE 1.2: MAXIMUM ULTRASOUND EXPOSURE LEVELS BY FREQUENCY

| Frequency (kHz) | SPL (dB) |
|-----------------|----------|
| 16 | 75 |
| 20 | 75 |
| 25 | 110 |
| 31.5 | 110 |
| 40 | 110 |
| 50 | 110 |

frequencies, the peak acoustic pressure can exceed 110 dB SPL, adding support for the use of a frequency above 100 kHz for this sensor [34].

An additional requirement for the proof of concept design is manufacturability. The design must be easily fabricated using well established manufacturing techniques. In order to ensure the design can be fabricated economically and within time allowances, the proof of concept design will be subject to strict fabrication constraints. Performance of the sensor will be optimized within these constraints.

1.8 Specific Research Objectives

1. The development and exploration of the theoretical model for a non-planar MEMS based ultrasonic sensor microarray through the expansion of the theory developed by [19]. This includes investigating the key parameters and performance of the newly expanded model.
2. Using investigation data from the new model, create a generalized array design flow to allow rapid development of arrays based on this topology. As far as it practical, this design flow will not be based on any specific fabrication technology.
3. Design a MEMS based ultrasonic sensor microarray for use as an enabling component of IAVSS system. The design will use the generalized array design flow to generate the geometry. A fabrication technology will be chosen and a detailed design of the sensing elements and array will be carried out.
4. Perform detailed analytical and 3-D finite element analysis (FEA) to verify the behaviour of the individual sensing elements and the complete array.

5. Concurrent development of a fabrication process and material selection with the sensor analytical design. The developed fabrication process is to use only standard MEMS fabrication techniques and materials to ensure manufacturability. The verified design process will be simulated to verify correct geometry and to guard against fabrication process incompatibilities.

1.9 Principle Results

The principle results of the research work presented in this thesis are summarized as follows:

1. A closed form generalized model for the array factor of a MEMS-based discretized hyperbolic paraboloid geometry ultrasonic sensor microarray has been developed by extending the theory of macroscale continuous aperture hyperbolic paraboloid geometry transducer as presented in [19]. The new model has been verified against the original model for beamforming capability and frequency response with excellent agreement. Additionally the new model supports placement of all elements parallel to the x-y plane for compatibility with MEMS fabrication techniques
2. The developed sensor microarray can intrinsically provide a broadband, constant-beamwidth, beamforming capability without any microelectronics based signal processing as necessary for conventional planar beamforming sensor arrays. This enable to sensor microarray to be used in real-time applications where split-second decisions are necessary, for example in automotive collision avoidance systems.
3. A generalized array design methodology has been developed based on the newly developed model. This provides an easy method to determine the array physical design specifications, such as: array side length and height, number of elevations (tiers), number and spacing of sensing surfaces based on the desired array response, sensing scheme selection, design and behaviour simulation of sensors and verification.
4. The developed model has been used to design two sensor microarrays: One in the frequency range of 2.3-5.2 MHz with a side length of 1.18mm sidelobe intensity of -10dB and a constant beamwidth of 20 ± 2 degrees. The array has 25 elevations and 29 sensing surfaces in each x and y directions. The other one in the 113-167 kHz frequency range with an array sidelength of 9.0 mm, -6dB side lobe intensity, and a constant beamwidth of $20 \pm 5^\circ$. The array has 3 elevations and 3 sensing surfaces in each x and y directions. The later design is intended for a proposed IAVSS system for automotive collision avoidance application.

5. MEMS-based capacitive type ultrasonic sensor have been chosen to constitute the array elements (sensing surfaces). Extensive analytical and FEA analysis has been performed to characterize and verify the behaviour of MEMS based capacitive type acoustical sensors. The analytical and 3-D coupled domain FEA results are in close agreement that verifies the design.
6. A silicon-on-insulator (SOI) based-fabrication process table has been developed in consultation with the Alberta nanofab facility and simulated using IntelliSuite to fabricate the array geometry developed for the IAVSS application. Array assembly and packaging information was determined and verified in conjunction with the CMC Microsystems.

1.10 Organization of Thesis

Chapter 2 deals with introducing the fundamentals of array based beamforming. From this foundation the extension into using shaped arrays to provide beamforming functionality is introduced. Existing work on hyperboloid paraboloid shaped arrays is presented. The existing theory is then expanded upon to include discrete arrays. A closed form model of the array factor for the discrete hyperbolic paraboloid shaped array is presented.

In Chapter 3 the beamforming theory developed previously is applied in the creation of a systematic method for hyperboloid paraboloidal MEMS compatible array design. The step by step procedure is given, as well as a numerical example. Equations based on extensive simulation data are presented to provide guidelines during array design. The procedure contained in this chapter is fabrication technology and transduction domain independent. The specific design procedure required for using the generated array geometry as a MEMS acoustic array are detailed next.

Chapter 4 introduces MEMS based acoustical sensors. The major transduction methods are reviewed. A lumped element model is used to allow the rapid determination of the design parameters for MEMS based acoustic sensors. The lumped element results are then verified against finite element analysis. The results show excellent consistency between the two methods.

Chapter 5 details fabrication related material. The array fabrication table is overviewed. Each major fabrication step is shown including simulation results. This process cumulates in the completed array.

Conclusions and final discussion take place in Chapter 6. Other applications for the beamforming technology are discussed.

Chapter 2

Non-Planar Beamforming

In contrast to planar sensor array geometries, a non-planar array refers to a one or two dimensional array where the sensor elements are distributed at different elevations along the vertical axis. The objective of constructing a non-planar array geometry is to obtain a better array response over the desired frequency range as compared to planar geometries. In this chapter the theory of a continuous aperture hyperbolic paraboloid geometry acoustical transducer is reviewed. Based on the review, a mathematical model for the array response of a discretized hyperbolic paraboloid geometry non-planar array that can be fabricated using state-of-the-art microfabrication techniques has been developed.

2.1 Theory of Hyperbolic Paraboloid Geometry Acoustical Transducer

The overall beam pattern of an array of sensors depends on five key parameters as listed below [35]:

1. The geometric configuration of the array elements (shape of the array)
2. Inter-element spacing
3. Element sensitivity
4. Signal phase at each element

5. The beam pattern of the individual elements

The array factor of a one-dimensional uniform array (array elements feature identical sensitivity, directional response and inter-element spacing) can be expressed as:

$$AF(\theta) = \sum_{n=0}^{N-1} e^{jn \left(\frac{\omega}{c} d \cdot \cos \theta \right)} \quad (2.1)$$

where N is the number of elements in the array, ω is the frequency in radians, c is the speed of sound in the medium, d is the inter-element spacing and θ is the angle of incidence.

By decoupling the array behaviour from the sensing element behaviour, the array and the sensing elements can be designed independently. This separation reduces the complexity level of the design. It also facilitates the creation of a general, technology independent methodology for hyperbolic paraboloid shaped array design.

A hyperbolic paraboloid surface as shown in Figure 2.1 satisfies the requirements for providing an intrinsic broadband constant beamwidth beamforming operation in 2 dimensions. A hyperbolic paraboloid-shaped continuous aperture transducer uses the transport delay associated with the curved nature of the sensing surface to maintain a constant beamwidth over a wide operating frequency range. No microelectronics-based signal processing is necessary for the beamforming operation. The beamwidth depends on the out-of-the plane twist of the hyperbolic paraboloid-shaped surface and is independently specified in each axis by the out-of-plane angle measured in degrees from the center of the array present at the array extremities [19, 20].

In the Cartesian coordinate system, a square footprint hyperbolic paraboloid surface can be expressed as [20]:

$$z = y \tan \left(\frac{2\alpha x}{L} \right) \quad (2.2)$$

Where x , y and z are the Cartesian coordinates, L is the sidelength in wavelengths in the x and y directions and α is the amount of out-of-plane twist in the z direction at the surface extremity measured in degrees from the center of the surface as shown in Figure 2.1.

The far-field directional response, or array factor, of a continuous aperture hyperbolic paraboloid-shaped acoustical sensor of side length L in a given direction (θ, ϕ) as referenced from the array normal is expressed as (2.3) [20]:

$$f(\theta, \phi) = \frac{1}{LY} \int_{-\frac{L}{2}}^{\frac{L}{2}} \int_{-\frac{L}{2}}^{\frac{L}{2}} e^{j2\pi t \left(x \tan \theta + y \tan \phi + \frac{2\alpha xy}{L} \right)} dy dx \quad (2.3)$$

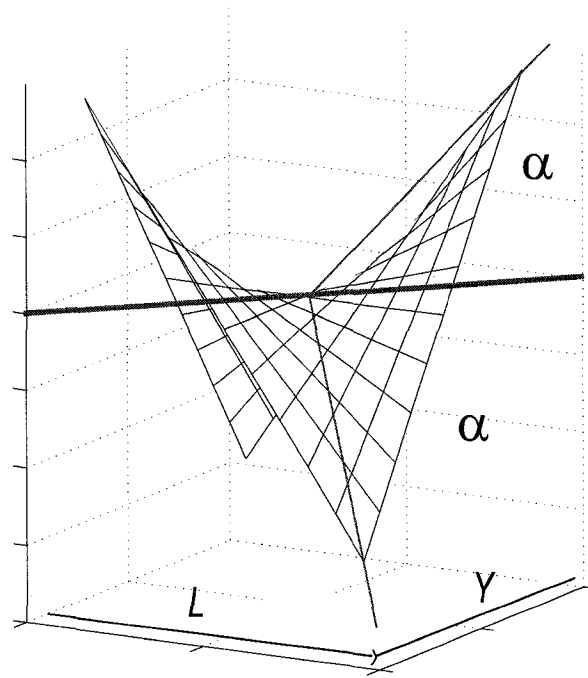


Figure 2.1: Hyperbolic Paraboloid Shaped Surface

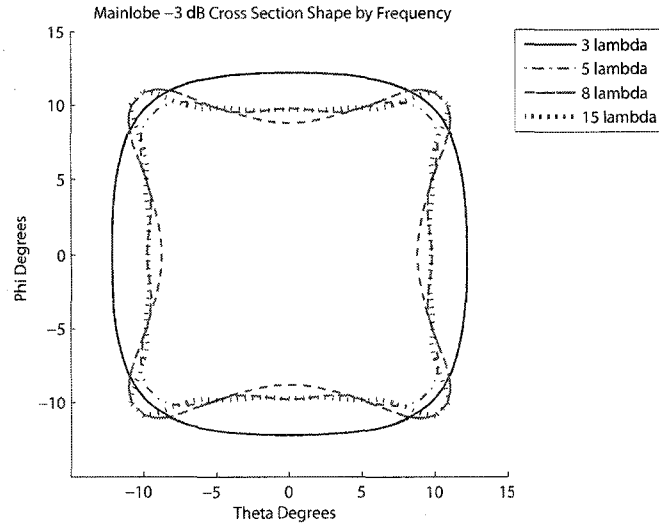


Figure 2.2: Beamforming with the Continuous Aperture Sensor

where Y is the array sidelength in the y direction, L is the array sidelength in x direction, and α is the out-of-the plane angle at the array extremities in both x and y directions, respectively. The parameter t in (2.3) is defined as:

$$t = \frac{1}{\sqrt{\tan^2 \theta + \tan^2 \phi + 1}} \quad (2.4)$$

Equation (2.3) assumes that the out-of-plane angle α is small and the sensor sidelengths L and Y are expressed in units of wavelengths of the desired acoustic frequency. It has been shown that for a large L with a small out-of-plane angle α , the directional response of the sensor has a reasonably constant value of $\frac{1}{2\alpha L}$ [20]. It has also been determined that $\alpha \leq 10^\circ$ results in a reasonably constant beamwidth of 2α whereas for $\alpha > 10^\circ$ (2.3) cannot be used to determine the beam shape accurately due to mathematical assumptions made during its derivation. Cross-sectional views of the mainbeam at -3dB are presented in Figure 2.2. This clearly shows the efficacy of the intrinsic broadband beamforming in the continuous aperture sensor.

Figure 2.2 shows that when the array size is below that of a conventional array featuring a micro-electronic beamforming engine, the beamwidth widens as is expected. As the operating frequency increases, the beampattern shrinks to obtain a minimum when $5\lambda_{op} = S$ where λ_{op} corresponds to the wavelength of the operating frequency and S refers to sensor sidelength. As the frequency increases beyond this point, the beamwidth increases monotonically until $10\lambda_{op} = S$. At all frequencies

above this, the beamwidth remains stable.

The intrinsic beamforming capability of this geometry is highly desirable for use in a microarray to minimize system power consumption and cost, while taking advantage of the scaling benefits offered by microfabrication. Due to the curved nature of the Hyperbolic Paraboloid surface, it is incompatible with the current state-of-the-art microfabrication techniques as they are based on planar operations.

Following synthesis theory commonly used in antenna design, it is possible to emulate the behaviour of a large continuous aperture sensor through the use of an array of smaller sensors [35]. The double integral expressing the array response in (2.3) can be expressed as the sum of an infinite number of discrete points separated by infinitesimal intervals using the spatial sampling technique. Each discretized value would represent a level or sensing surface in a 3-D space. This array of sensors located at different elevations (non-planar), resembling a discretized hyperbolic paraboloid surface, could be realized using the conventional planar microfabrication techniques.

The fundamental theorem of Calculus states that the double integral in (2.3) can be discretized by using the Riemann summation [36]. After performing spatial sampling using the Riemann summation, the infinite summation can be reduced to a finite one of an arbitrary number of levels. Due to the loss of sensing elements after reduction, it is expected that there may be some performance degradation of the array response. A conceptual geometry of a discretized hyperbolic paraboloid surface is shown in Figure 2.3. However, care must be taken to ensure that the geometric approximation remains suitably accurate to allow operation over the desired frequency range. This limitation is explored in depth in Chapter 3. Counter to the desire for an accurate representation of the geometry are the demands of manufacturability. Too many elevation levels may make the fabrication process complex, as each of the elevations may hold one or more sensing surfaces. The process used to generate the discrete geometry is shown graphically in Figure 2.4.

From the different variations of the Riemann summation, derivations based on the center-based Riemann summation are used due to their accuracy for non-monotonic functions, and the ability to calculate error bounds [36]. The center-based Riemann summation in one dimension can be expressed as [36]:

$$\int_a^b f(x)dx = \lim_{n \rightarrow \infty} \sum_{i=1}^n f\left(a + \left(i + \frac{1}{2}\right) \frac{b-a}{n}\right) \frac{b-a}{n} \quad (2.5)$$

where n represents the number of discretized levels. The maximum error present in this approximation is given as:

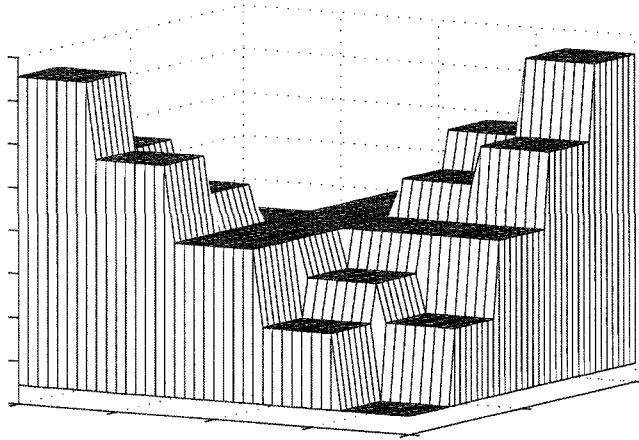


Figure 2.3: Seven Elevation Discrete Hyperbolic Paraboloid

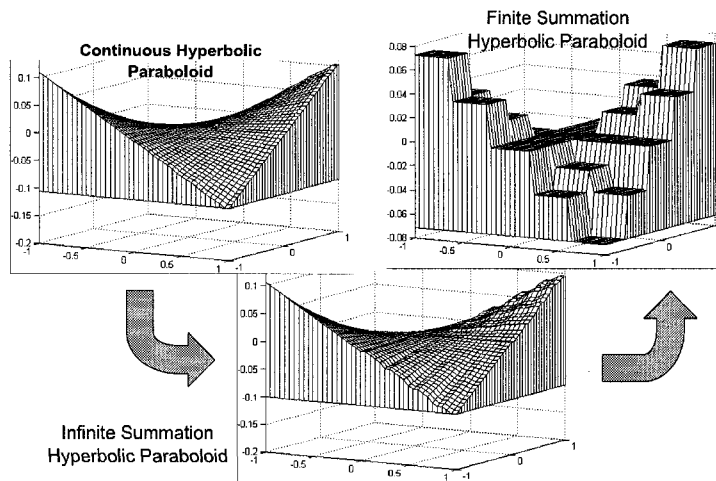


Figure 2.4: From Continuous Aperture Transducer to Discrete Array

$$\left| \int_a^b f(x)dx - A_{mid} \right| \leq \frac{M_2(b-a)^3}{12n^2} \quad (2.6)$$

where M_2 is the maximum value of $|f''(x)|$ and A_{mid} is the value of $f(x)$ at the midpoint of the interval $a-b$.

Applying (2.5) to (2.3) along the x axis yields:

$$f(\theta, \phi) = \frac{1}{MY} \lim_{M \rightarrow \infty} \sum_{m=0}^{M-1} \int_{-\frac{Y}{2}}^{\frac{Y}{2}} e^{j2\pi t \left((x') \tan \theta + y \tan \phi + \frac{2a(x')y}{L} \right)} dy \quad (2.7)$$

The transformation is then applied a second time along the y axis to obtain the discretized array response as:

$$f(\theta, \phi) = \frac{1}{MN} \lim_{M \rightarrow \infty} \lim_{N \rightarrow \infty} \sum_{m=0}^{M-1} \sum_{n=0}^{N-1} e^{j2\pi t \left((x') \tan \theta + (y') \tan \phi + \frac{2a(x')(y')}{L} \right)} \quad (2.8)$$

where:

$$x' = \left(-\frac{L}{2} + \left(m + \frac{1}{2} \right) \frac{L}{M} \right) , \quad y' = \left(-\frac{Y}{2} + \left(n + \frac{1}{2} \right) \frac{Y}{N} \right) \quad (2.9)$$

Equation (2.8) is the array response from a discretized hyperbolic paraboloid surface where the parameters M and N represent the number of sensing surfaces in the x and y directions respectively. Finally, (2.8) can be reduced to a finite summation as expressed in (2.10) where M and N are finite integers.

$$f(\theta, \phi) = \frac{1}{MN} \sum_{m=0}^{M-1} \sum_{n=0}^{N-1} e^{j2\pi t \left((x') \tan \theta + (y') \tan \phi + \frac{2a(x')(y')}{L} \right)} \quad (2.10)$$

Equation (2.10) represents the array factor for a discretized hyperbolic paraboloid geometry sensor array. The minimum sidelength S (in meters) of a square footprint hyperbolic paraboloid geometry array can be determined using the following relation:

$$S_{min} = \frac{Kc}{f_{lower}} \quad (2.11)$$

where c is the speed of sound in the media and f_{lower} is the lower bound of the operating frequency range. K is a fitting parameter based on the amount of acceptable beamshape variation.

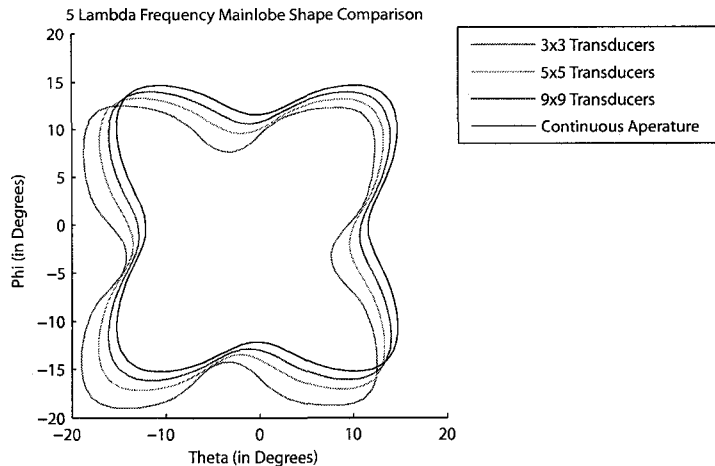


Figure 2.5: Main Beam -3dB Cross-Sections of Continuous and Discrete Arrays

Values for K can range between 3 and 10 (see section 3.1). The array response as expressed in (2.10) has been verified by comparing results from the integral model as expressed in (2.3). The results converge exceedingly well even for low values of M and N . The results converge even for $M = N = 3$ when the array sidelengths correspond to 5λ where λ is the wavelength of the lower bound of the operating frequency. The difference between the array responses from (2.3) and (2.10) for a 3 sensing surface per axis implementation averages less than 18% in the passband. Although this seems like a large error, investigation shows that the primary source of this error is a small shift of the main beam. This can be seen in the -3dB cut-off as shown in Figure 2.5. Within the passband region, the responses remain significantly identical. This error can be reduced significantly as shown in Figure 2.6, by increasing the number of tiers. From Figure 2.6, it appears that the average beamshape error can be reduced to $< 5\%$ with only a moderate number of tiers.

The 3-D beam pattern of a discretized square footprint hyperbolic paraboloid surface is shown in Figure 2.7 for a sidelength of 5λ and 15λ where λ is the wavelength of the operating frequency lower bound. Figure 2.7 clearly establishes that it is possible to construct a frequency-independent broadband beamforming sensor microarray with discrete array elements by exploiting the surface topology.

A contour plot of the beam patterns for different frequencies in a desired frequency band is shown in Figure 2.8. From Figure 2.8, it is evident that if the array has a sidelength equal to five times the wavelength of the lowest frequency in the desired frequency band, the beam patterns of the higher frequencies in the range remain reasonably identical to the lowest frequency. Having more

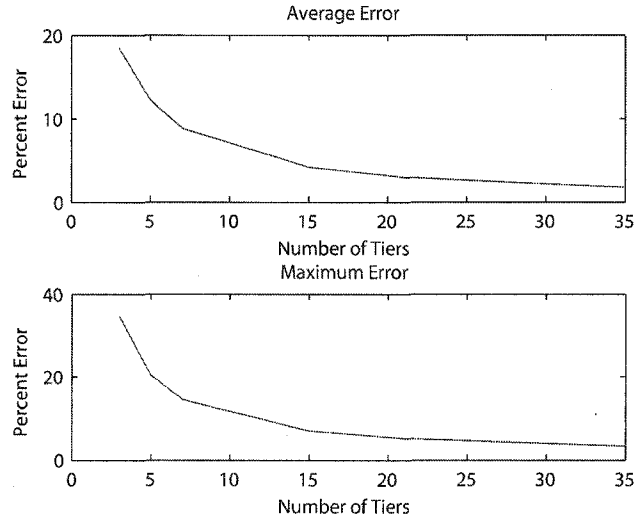


Figure 2.6: Worst Case Passband Approximation Error

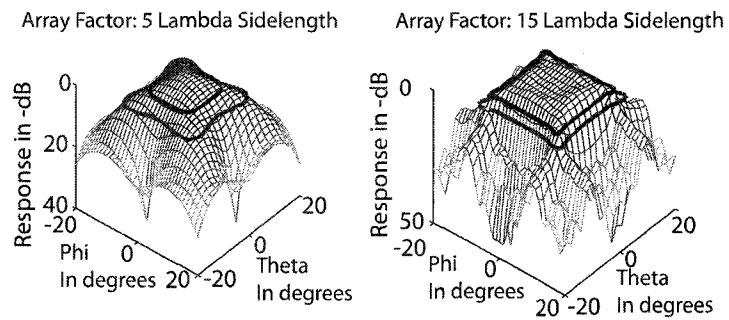


Figure 2.7: 3-D Change in Beamshape over Change in Lambda

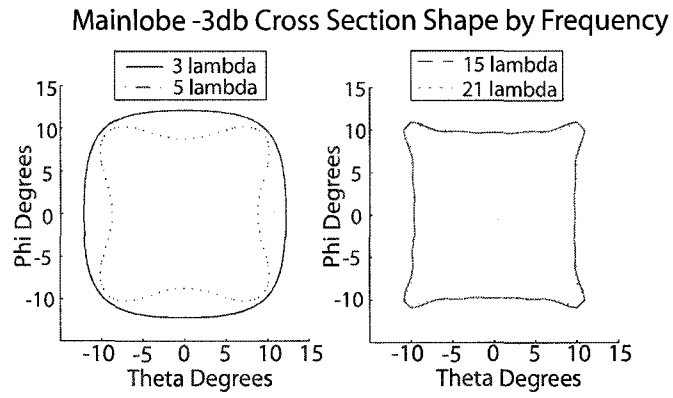


Figure 2.8: Cross-Sectional Changes in Beamshape Over Change in Lambda

sensing elements in each axis allows a better approximation and a wider operating range at the cost of increased geometric complexity.

Chapter 3

Array Design

In this chapter, the design methodology for an acoustic sensor array based on the discretized hyperbolic paraboloid geometry is presented. The methodology is based on the mathematical model developed in the previous chapter. The presented generalized methodology is fabrication technology independent and can be tailored to accommodate specific design requirements and the fabrication processes available in a standard foundry within certain limitations. Once the desired operating frequency range, beamwidth and acceptable beamwidth variation within the operating frequency range are specified, the methodology enables the determination of the geometric specifications for the array. This occurs in a straightforward manner by following a set of mathematical relations developed from an exploration of the mathematical model from Chapter 2.

3.1 Determination of Array Sidelength

The array sidelength can be determined from:

$$S_{min} = \frac{Kc}{f_{lower}} \quad (3.1)$$

Where S is the sidelength, K is an empirical parameter that specifies the acceptable variation in the beamwidth for different frequencies over the desired frequency range, c is the speed of sound in the media, and f_{lower} is the lower bound of the desired frequency range. As the beamwidth decreases with an increase in the frequency, the empirical parameter K maintains the beamwidth within a

TABLE 3.1: BEAMWIDTH CONTROL PARAMETER K VALUES

| K (unitless) | Beamwidth Variation($^{\circ}$) |
|--------------|-----------------------------------|
| 3 | 7 |
| 5 | 5 |
| 8 | 2 |
| 10 | 1 |

range of $1 - 10^{\circ}$ variations for all the frequencies in a frequency range of $\frac{f_{upper}}{f_{lower}} = 40$. This range of frequency appears to be sufficient for most applications. For example, for a value of $K = 10$, the maximum beamwidth variation for all the frequencies in the range is less than 1° whereas for $K = 3$, the maximum variation increases to 7° . Following (3.1), for a fixed f_{lower} , lowering K reduces the array sidelength at the expense of a wider beamwidth variation. Table 3.1 lists the determined beamwidth variations expected for different K values for a frequency range where $\frac{f_{upper}}{f_{lower}} \leq 40$.

3.2 Determining the Number of Sensing Surfaces

Following (2.10), the constant beamwidth property over the operating frequency range of the discretized hyperbolic paraboloid geometry array is a direct function of the number of the sensing surfaces. Typically, the Nyquist criteria for spatial sampling provides a method to determine the inter-element spacing, and by extension, the number of sensing surfaces present in the array. This criteria specifies that the main lobe power is maximized for the frequency where the inter-element spacing is equal to $\lambda/2$ where lambda is the wavelength of the operating frequency. However, for a frequency range, satisfying the Nyquist criteria isn't possible for all frequencies. Thus, applying the Nyquist criteria to determine the spacing between the sensing surfaces in the discretized hyperbolic paraboloid geometry array will predict an erroneous result, even if the wavelength associated with the center frequency in the desired frequency band is used to determine the spacing between the sensing surfaces.

It is observed, however, that a nearly linear relationship is present between the number of sensing surfaces and the maximum operating frequency for a pre-specified sidelobe power as shown in Figure 3.1. This figure illustrates the relationship as gathered from numerical simulations using MatlabTM. Based on the simulation results, an empirical relation has been developed that uses the sidelobe power as a cost function and least square data fitting techniques to ensure the sidelobe power for all

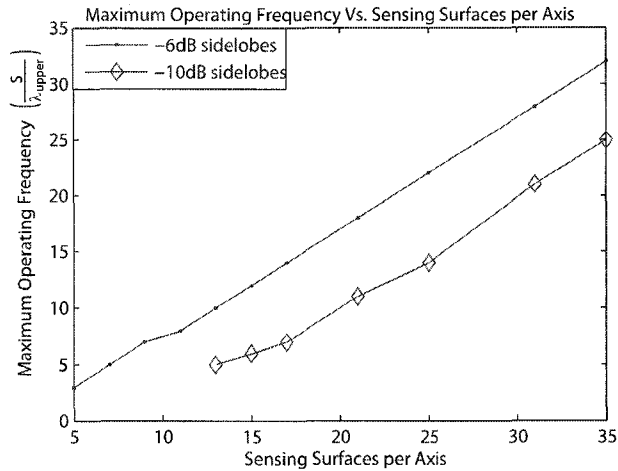


Figure 3.1: Relationship Between the Number of Sensing Surfaces in Each Axis to Sidelobe Intensity

the frequencies in the target range are below some pre-specified level while optimizing the number of sensing surfaces M and N in each direction. The resulting equations (3.2) and (3.3) specify the number of sensing surfaces per axis for a square footprint array for -10 dB and -6dB sidelobe powers, respectively.

$$M, N = \lceil 5.69 \times \left(\frac{S}{\lambda_{upper}} \right)^{0.5695} - 0.8637 \rceil \quad (3.2)$$

$$M, N = \lceil 1.49 \times \left(\frac{S}{\lambda_{upper}} \right)^{0.9029} - 0.8484 \rceil \quad (3.3)$$

3.3 Array Height and Tier Elevation Calculations

The height of the array is directly related to the out-of-plane twist present at the array extremities. The maximum height measured from the center of a continuous-aperture hyperbolic paraboloid geometry sensor can be determined from the out-of-plane angle α as $S \cdot \tan \alpha$ where S is the sidelength of the square footprint sensor geometry as shown in Figure 3.2.

For the discretized array geometry, a slight decrease in height is present due to height determination sampling occurring not at the array extremity, but at the center of the outermost sensing surface as shown in Figure 3.3

This sampling error introduces an angular error of less than 4.0% for arrays with 5 or more sensing surfaces per axis. Since the angular error introduced by the sampling process is small, the

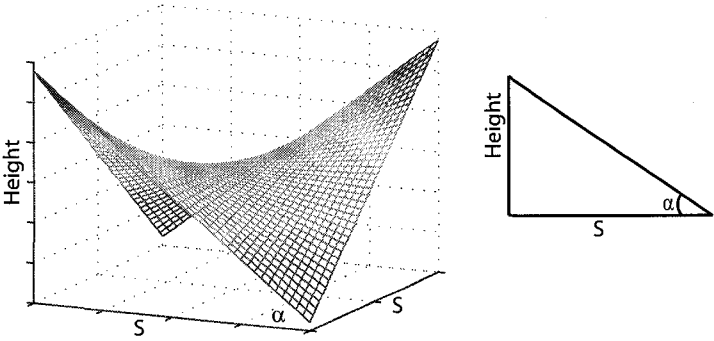


Figure 3.2: Array Height and Out-of-Plane Twist

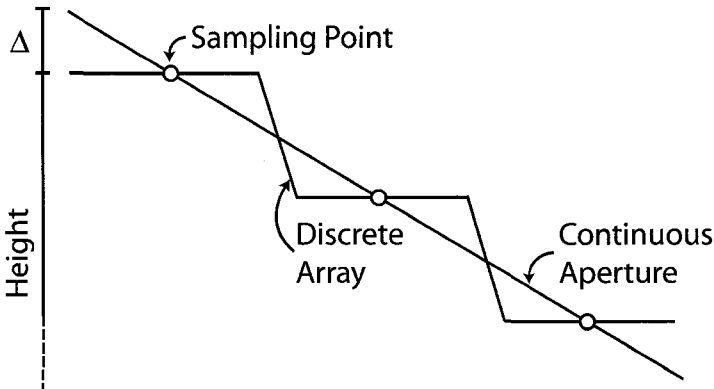


Figure 3.3: Discrete Array Height Sampling

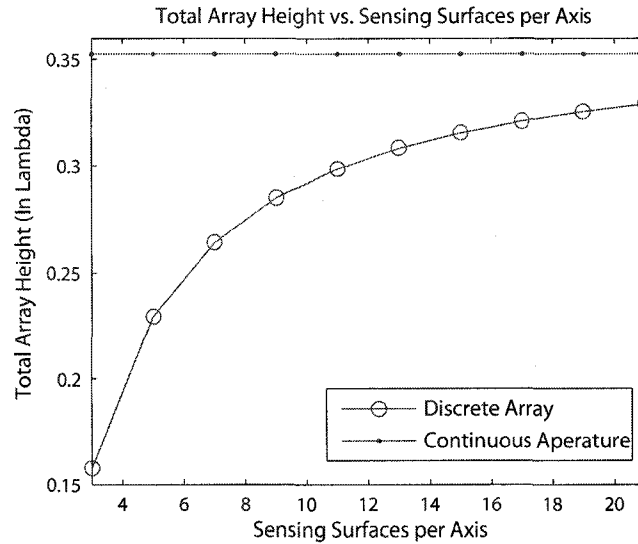


Figure 3.4: Relation Between Number of Sensing Surfaces in Each Axis and Total Height

array beamwidth is affected by $< 1^\circ$ by the sampling process. As the number of sensing surfaces per axis increases, the total height error, and as such the beamwidth error introduced decreases as the outermost sensing surface center approaches the array extremity. The total array height and the effects of increasing the number of sensing surfaces per axis are illustrated in Figure 3.4. The total height (H) for a discretized square footprint array geometry can be determined using (3.4), which has been developed using a curve-fitting technique from numerical simulation results obtained using MatlabTM for an out-of-plane twist angle of 10° .

$$H = (-0.5215 \times M^{-0.792} + 0.3762) \frac{S \cdot \alpha}{10^\circ} \quad (3.4)$$

Where M represents the number of sensing surfaces in each of the x and y directions.

From Figure 3.4, it is evident that as the number of sensing surfaces is increased, the array height or dip from the center of the hyperbolic paraboloid surface increases and approaches towards that of continuous aperture hyperbolic paraboloid sensor geometry.

3.3.1 Tier Elevation

The total number of elevations in the device varies depending on the chosen mechanical tolerances. Even accepting a grouping of elevations with heights within 1% can dramatically decrease the number

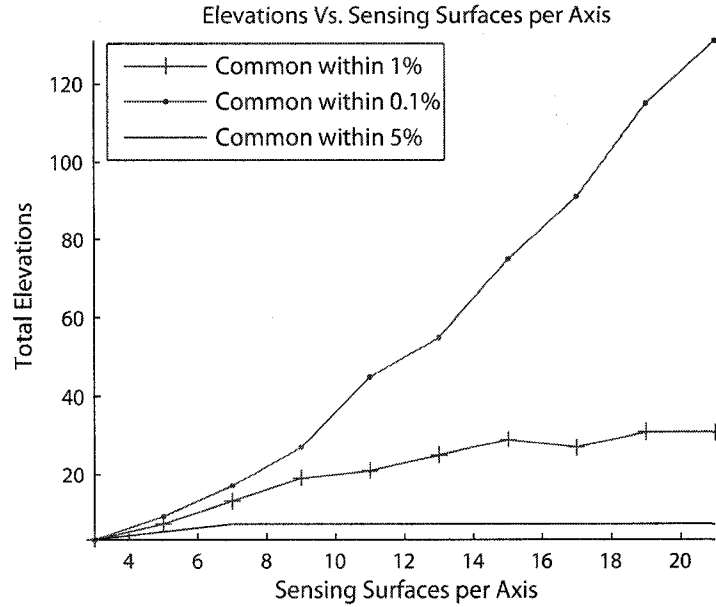


Figure 3.5: Relationship Between Number of Elevation in the Array and the Number of Sensing Surfaces in Each Axis

of distinct elevations required to fabricate the array. The number of elevations required to express the geometry for a specified number of sensors per axis can be determined from the relation:

$$N_{elevations} = \lfloor -67.46 \times M^{-0.2394} + 54.39 \rfloor \quad (3.5)$$

Equation (3.5) has been derived from numerical simulation results under the assumption that sensors with heights varying less than 1% are placed on a common elevation. The trend is shown in Figure 3.5.

Due to the nonlinear effects introduced by the grouping procedure, (3.5) is an approximation accurate to within 10% for surfaces with less than 25 post-grouping elevations. Appendix A contains Matlab™ code to positively determine the exact number of elevations. The code is based on generating a continuous hyperbolic paraboloid and sampling the elevation at the specified number of points per axis, as determined by the number of sensors per axis. The sampled elevations are compared for grouping purposes within the specified accuracy, and unique elevations are counted. The number of elevations ($N_{elevations}$), or tiers, is an important measure of the mechanical complexity of the array, as each additional elevation adds complexity to the manufacturing of the array.

3.4 Step 4 – Sensing Surface Design

The general array design undertaken so far has been fabrication technology and scale-independent, assuming that the individual sensing surfaces are generalized transducers. However, actual selection of the transduction mechanism - capacitive or piezoelectric type - depends on the sensitivity, power requirements, ease of fabrication or assembling, dynamic range, noise performance and other design requirements.

For a MEMS based implementation within the scope of this thesis, the first step in transducer selection is the determination of a possible sensor type. Capacitive-type acoustical sensors have been chosen over piezoelectric types for their robustness and ease of fabrication. Additionally, a silicon-on-insulator based fabrication process was chosen to further simplify the manufacturing of the array while simultaneously increasing sensitivity and durability of the device through the low residual stress and relatively higher thickness of the diaphragm surface. In order to avoid the complexities of depositing films at different elevations, the array is designed to be manually assembled after fabrication of each sensing surface is complete. The Canadian Microelectronics Corporation (CMC Microsystems) offers the assembling services that can provide mechanical tolerances within 1% of the sensing surface height during assembly. This approach is excellent for a low complexity design with a nominal number of sensing surfaces in each axis ($M = N = 3$); however it is labor intensive and poorly suited to complex designs or large volume applications, where monolithic array fabrication with a larger number of tiers would be greatly preferable.

Detailed design of capacitive type acoustical sensors chosen for the sensor microarray are presented in Chapter 4 and associated sensor microarray fabrication is presented in Chapter 5.

3.5 Numerical Example

3.5.1 Problem Definition

A numerical design example is presented here to illustrate the developed design methodology. It is assumed that the target tiered topology non-planar hyperbolic paraboloid geometry sensor microarray is to operate in air at standard temperature and pressure. The operating frequency range is 2.3 MHz-5.2 MHz ($f_{lower} = 2.3$ MHz and $f_{upper} = 5.2$ MHz) This frequency range is common for medical ultrasound imaging applications [14, 37]. The beamwidth is specified as $20 \pm 2^\circ$. As it a high-sensitivity application, -10dB or less sidelobe intensity is desirable to improve the signal to noise ratio. Additionally, it has been assumed that there are no fabrication constraints present.

3.5.2 Solution

The wavelength of the lower operating frequency f_{lower} can be determined from:

$$\lambda = \frac{c}{f} \quad (3.6)$$

which corresponds to $147.82\mu\text{m}$ for a speed of propagation in air $c = 340\text{m/s}$. For a permissible 2° variation of the beamwidth for all the frequencies in the range, the beamwidth parameter K can be determined from the Table 3.1 as $K \geq 8$. In order to minimize the array size, $K = 8$ has been chosen. Substituting this value of K in (3.1) yields the array sidelength S of the square footprint array as 1.1826mm . The wavelength associated with the upper frequency can be determined as $65.385\mu\text{m}$ following (3.6). The number of sensing surfaces in each axis can be determined following (3.2) as $M, N = \lceil 28.75 \rceil = 29$ to satisfy the design requirement of -10 dB maximum sidelobe intensity.

Next, the array height can be determined by using (3.4) to be $402.1\mu\text{m}$. This array height fits comfortably within the thickness of a standard thickness silicon wafer. A good compromise between geometric accuracy and the total number of elevations required for fabrication could be reached by assigning all sensors with heights varying less than 1% to a common elevation. With this approximation, use of (3.5) yields the number of distinct elevations as $N_{elevations} = \lceil 24.26 \rceil = 25$. Thus, the $402.1\mu\text{m}$ total height of the array is distributed across 25 elevations as shown in Figure 3.6. Geometric specifications of the sensor array are shown in Table 3.2. To determine the height of each elevation, a MatlabTM simulation was used to perform the quantization based on the continuous hyperbolic paraboloid. The simulation code is in Appendix A. The polar plots in Figures 3.7 – 3.9 illustrate the array response at 2.3, 3.75 and 5.2MHz respectively. From the figures, it is evident that the array exhibits excellent beamwidth stability for the frequencies in the operating frequency range and a mainlobe magnitude variation of less than 1dB over the operating range. Figure 3.10 shows cross-sections of each of the main-lobes from Figures 3.7 – 3.9 to further illustrate the beamwidth stability. The resulting values of the design are outlined in Table 3.2.

TABLE 3.2: NUMERICAL EXAMPLE – RESULTS

| Parameter | Value |
|----------------------------|---------------------|
| Lower Operating Frequency | 2.3 MHz |
| Upper Operating Frequency | 5.2 MHz |
| Maximum Sidelobe Intensity | -10 dB |
| Beamwidth | 20 ± 2 |
| Array Sidelength (S) | 1.1826 mm |
| Total Array Height | 402.1 μm |
| Sensing Surfaces Per Axis | 29 |
| Total Elevations | 25 |

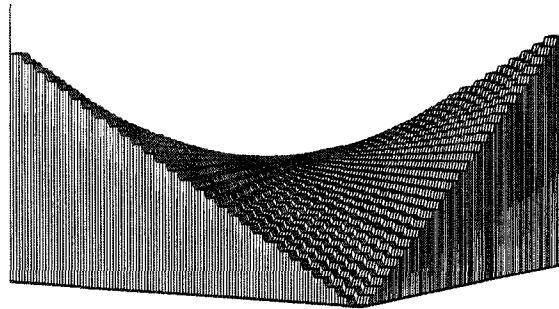


Figure 3.6: Illustration of Numerical Example Array and Geometry Approximation

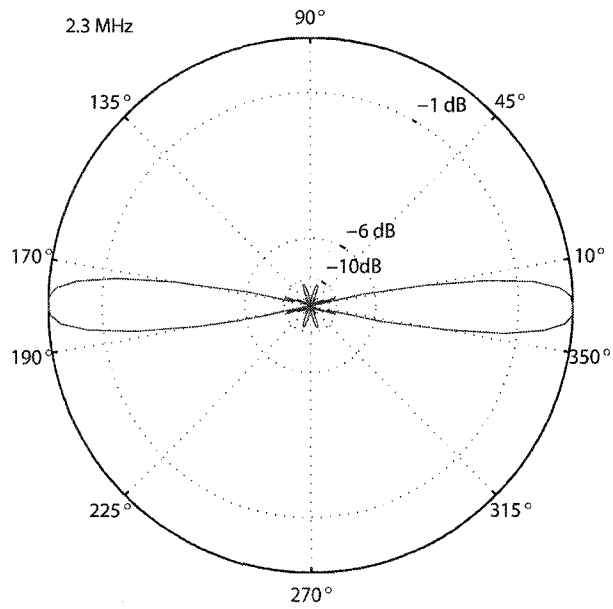


Figure 3.7: Array Beamshape at 2.3 MHz

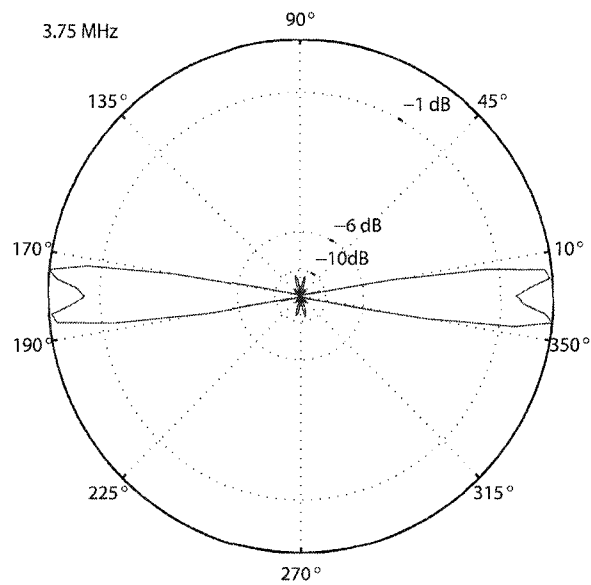


Figure 3.8: Array Beamshape at 3.75 MHz

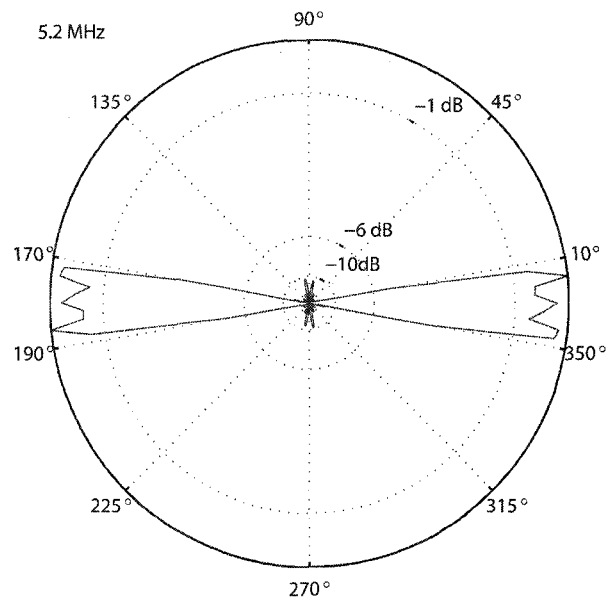


Figure 3.9: Array Beamshape at 5.2 MHz

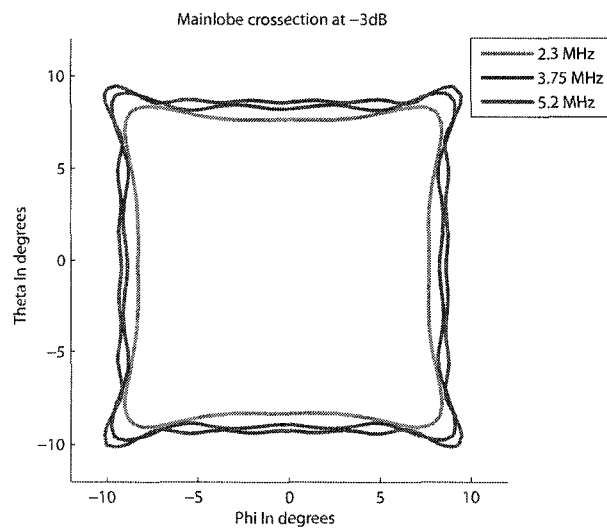


Figure 3.10: Array Mainlobe Cross-Sections at -3 dB

3.6 Array Design for IAVSS

3.6.1 Problem Definition

As it is evident from Figure 3.6, fabrication of capacitive sensors on 25 different elevations is a very challenging task with the existing microfabrication technology and might be expensive. The embedded mask method discussed in detail in Chapter 5 is capable of creating devices with an arbitrary number of elevations. The embedded mask method requires the use of deep reactive ion etching (DRIE). The DRIE procedure does not currently support etch stops. As a result, maintaining accurate etch depths for successive etching procedures is a challenging process. To further complicate fabrication, the DRIE process etches at differing rates as you vary radially outward along the wafer. Although these limitations can be overcome with current fabrication technologies, it is a slow process requiring several production runs to tune the process parameters correctly.

It has been observed that reasonably constant beamwidth can be achieved with a minimal number of tiers or elevations. Additionally, identical sensors, batch-fabricated on a single wafer, could be diced and manually assembled to realize the discretized hyperbolic paraboloid geometry. This relieves of the complexities of depositing films at different elevations. This benefit comes at the additional expense of the associated manual assembly. The Canadian Microelectronics Corporation (CMC) is able to provide mechanical tolerances within 1% of the sensing surface height during assembly. This approach is excellent for initial production of low-complexity designs such as the IAVSS array. For this manual assembly method, a silicon-on-insulator (SOI) based fabrication process for capacitive sensors further simplifies the manufacturing of the array while simultaneously increasing sensitivity and durability of the device through the low residual stress in the device layer of SOI wafers(diaphragm). The diaphragms are relatively thick compared to many non-SOI based designs. The extra thickness provides added strength to the design and was required to obtain good thickness uniformity across the wafer.

Design specifications for the simplified array geometry are listed in Table 3.3.

TABLE 3.3: IAVSS ARRAY DESIGN PERFORMANCE SPECIFICATIONS

| Parameter | Value |
|----------------------------|------------------|
| Lower Operating Frequency | 113 kHz |
| Upper Operating Frequency | 167 kHz |
| Maximum Sidelobe Intensity | -6 dB |
| Beamwidth | $20 \pm 5^\circ$ |

The microarray is to be designed for operation in air at standard pressure over a wide range of operating temperatures. The robust mechanical design of sensor combined with the specified frequency range enables the array to be used in an IAVSS. The constant broadband beamwidth of the sensor will allow for precision monitoring of the vehicle surroundings while eliminating echo from the vehicle body. This sensor provides a building block for the safety shell which is able to function even in the event of a nearby collision. By providing an intrinsic beamforming function, the sensor is able to offload this function from digital processors, reducing the processing demands while removing related latency.

The reduced number of sensors per axis mandates the use of a relatively narrow operating frequency range. Since $\frac{f_{upper}}{f_{lower}} \ll 40$, experimental results show a result of this is the beamwidth variation of the array will be reduced to $20 \pm 5^\circ$. Additional sidelobe intensity will be accepted in order to reduce the fabrication complexity. This method was also chosen due to its low time and equipment requirements. This solution tends to place strict limits on the maximum complexity of the design. A relatively narrow operating range is chosen as this is the primary cause of design complexity for this geometry.

3.6.2 Solution

The wavelength λ_{lower} associated with the lower bound of the target operating frequency range of 113 kHz can be approximated as 3.0 mm. In order to determine the array side length following (3.1), a value for K must first be chosen from Table 3.1. The values in Table 3.1 correspond to $\frac{f_{upper}}{f_{lower}} = 40$. In this application $\frac{f_{upper}}{f_{lower}} \approx 1.5 \ll 40$. As a result, Table 3.1 overestimates the amount of beamwidth variation. Experimental data shows the value of K can be chosen as 3. This meets performance requirements while reducing the array sidelength to a value of 9.00 mm.

We determine λ_{upper} via (3.1) to have a value of 2.03 mm. This provides all the information needed to determine the number of sensing surfaces per axis required to meet the design specifications. The design requirement of -6dB maximum sidelobe intensity mandates the use of (3.3) to determine the number of sensing surfaces per axis:

$$M, N = [4.868] = 5 \quad (3.7)$$

In consultation with the CMC, it was determined that 25 dies was a large number to be integrated into a single package. A 3×3 array with only 9 dies to be integrated was determined to be practical for manual assembly. Due to the extremely rough geometric approximation imposed by the fabrication

TABLE 3.4: IAVSS ARRAY GEOMETRY

| Parameter | Value |
|---------------------------|----------|
| Array Sidelength (S) | 9.00 mm |
| Total Array Height | 1.586 mm |
| Sensing Surfaces Per Axis | 3 |
| Total Elevations | 3 |

process, a baffle was added to help suppress side lobes. The baffle has been modeled as 6dB of attenuation outside the range of $\pm 25^\circ$ centered on the array normal.

The total array height is an important factor in choosing fabrication techniques that are suited to the design. For hand-assembled arrays, the total height has little effect on the suitability of various fabrication methods as the array will be manufactured in a plane.

A total height of 1.59mm is required for this design. A standard wafer can be used as a shim to provide this spacing during fabrication. For the 3×3 array, only 3 elevations are present due to symmetry. The lower elevation is assigned a height of 0. The middle elevation found across the center of the array in each axis is $793.5\mu\text{m}$. The uppermost elevation is found at 1.59mm above the surface of the array. It is important to note that when determining the thickness of the shims the substrate thickness must be accounted for. Therefore, assuming the sensing surface wafer including substrate is $500\mu\text{m}$, the shim wafer must be $293.5\mu\text{m}$ thick. It is also important to account for adhesive thicknesses during these calculations.

Geometric specifications of the sensor array are shown in Table 3.4. To determine the height of each elevation, a MatlabTM simulation was used to perform the quantization based on the continuous Hyperbolic Paraboloid. The simulation code is in Appendix A.

The polar plots in Figures 3.12 – 3.14 illustrate the array response at 113, 140, and 167 kHz respectively. From the figures, it is evident that the array exhibits excellent beamwidth stability for the frequencies in the operating frequency range and a mainlobe magnitude variation of less than 1dB over the operating range. Figure 3.15 shows cross-sections of each of the main-lobes from Figures 3.12 – 3.14 to further illustrate the beamwidth stability.

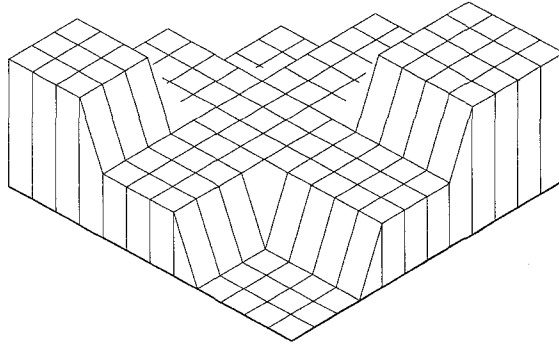


Figure 3.11: Illustration of IAVSS Array and Geometry Approximation

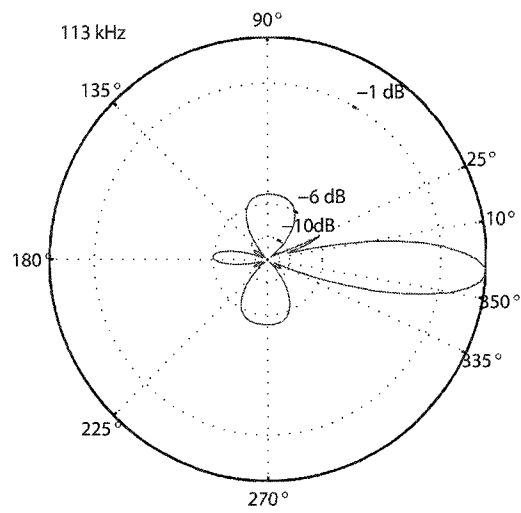


Figure 3.12: IAVSS Array Beamshape at 113 kHz

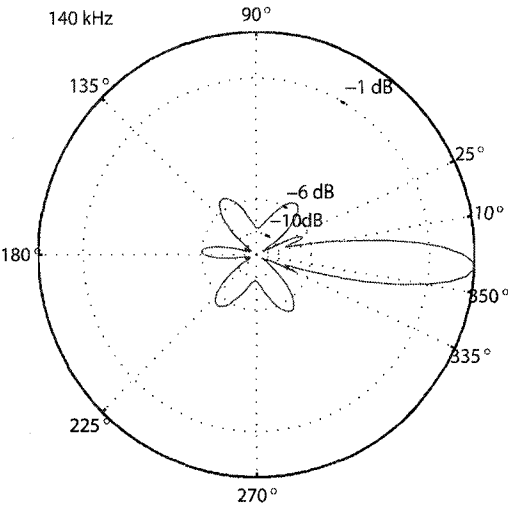


Figure 3.13: IAVSS Array Beamshape at 140 kHz

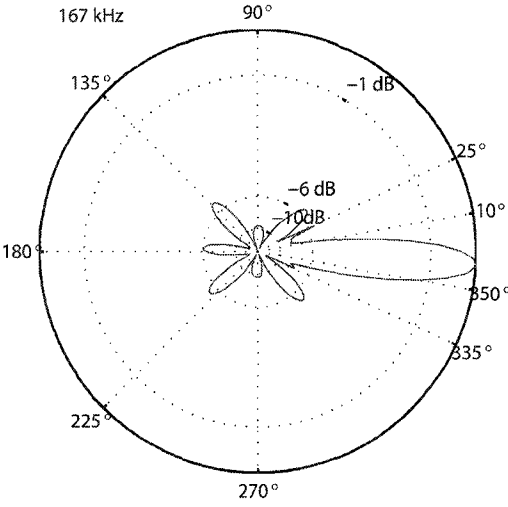


Figure 3.14: IAVSS Array Beamshape at 167 kHz

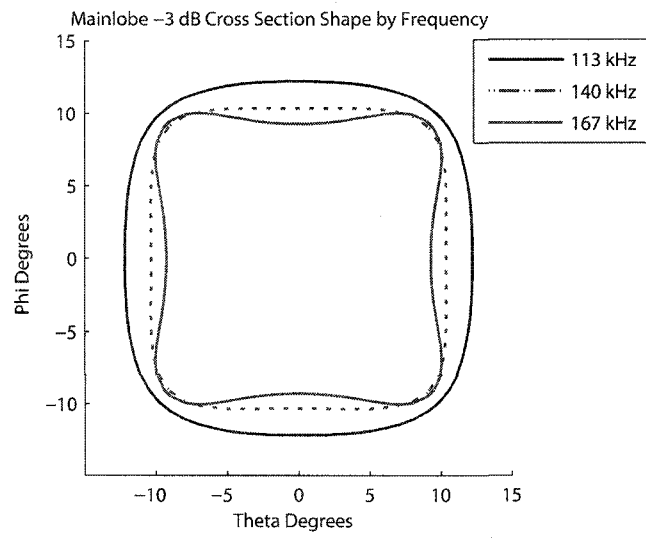


Figure 3.15: IAVSS Array Mainlobe Cross-Sections at -3 dB

Chapter 4

Transducer Modeling

This chapter describes the detailed design procedure of ultrasonic sensors. An analog electrical-equivalent circuit of the sensor has been used to determine the sensor's sensitivity; the circuit includes all electrical and mechanical design parameters. A lumped element analysis has been carried out to optimize the parameter values. Then IntelliSuite 3-D electromechanical analysis has been carried out to verify the device behavior.

4.1 MEMS Acoustic Sensors

Various Transduction mechanisms are available when performing MEMS acoustic sensing, the most popular methods are outlined below.

4.1.1 Piezoelectric Transduction

Piezoelectric thin films have been employed in several micro-scale actuation and sensing applications including various micro-manipulation tools, fluid transport, accelerometers and ultrasonic transducers. In all of these applications a piezoelectric thin film is deposited on a substrate of the specified geometry, often cantilever beams, or membranes as shown in Figure 4.1.

By applying an electric field to the film, the resulting strain (due to the direct piezoelectric effect) causes the structure to bend, producing useful work. Conversely, the flexural motion of the structure can be sensed by measuring the electrical output of the film due to the converse piezoelectric

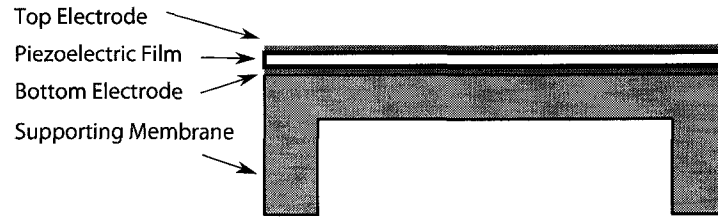


Figure 4.1: Piezoelectric Actuator

effect. Ferroelectric materials exhibit large piezoelectric constants and electromechanical coupling factors necessary to achieve large forces and displacements effectively. By applying the electric field across the thickness (the three direction), the lateral strain induces membrane bending (in the one direction) causing pressure wave propagation in the contact medium. In actuation using this scheme the thickness of the piezoactive layer does not dictate the operating frequency. Instead, the frequency is governed by the dimensions and the layering materials of the membrane. This offers design flexibility over conventional actuation, where the operating frequency is a function of the piezoactive layer thickness.

4.1.2 Piezoresistive Transduction

Piezoresistivity was first discovered in 1856 by Lord Kelvin. It's first application did not appear until the 1930's. The first application was in strain gauges. Generally strain gauges are made from a thin metal foil applied to a substrate which can be glued onto the surface which requires monitoring. The sensitivity of a strain gauge is known as the gauge factor. This dimensionless quantity is given by (4.1).

$$GF = \frac{\Delta R/R}{\varepsilon} \quad (4.1)$$

Where $\Delta R/R$ is the relative change in resistance and ε is the the applied strain. The change in resistance comes from two sources. The first is the piezoresistive effects, and the second is effects due to the geometry change due to the applied strain. The gauge factor for different materials is shown in Table 4.1 [30]:

Semiconductor strain gauges have the highest gauge factors, making them ideal materials for piezoresistive sensing. Semiconductor piezo-effects are also highly temperature dependant. As a result compensation techniques must be used to ensure accurate measurements. The change in sign present in the semiconductor materials is dependent on doping. For negative values, an N-

TABLE 4.1: GAUGE FACTORS FOR DIFFERING MATERIALS

| Material | Gauge Factor |
|-------------------------|--------------|
| Metal foil strain gauge | 2-5 |
| Thin-film metal | 2 |
| Single crystal silicon | -125 - +200 |
| Polysilicon | ± 30 |
| Thick-film resistors | 10 |

type doping is used. In this case the resistance decreases with strain instead of increasing. The gauge factor is also highly orientation dependent in semiconductors. The change in resistance is accomplished by exploiting the fact that the hole mobility is affected by the applied strain. MEMS fabrication allows the deposition of thin film strain gauges manufactured from metal or silicon directly onto the desired substrate. By becoming an integral part of the system, problems associated with the adhesives over time or temperature are eliminated. When used as MEMS sensing elements, Piezoresistive sensing provides a simple linear output at the cost of higher noise and manufacturing complexity. Another downside of piezoresistive sensing is the poor power efficiency due to the resistive nature of the sensing circuitry.

4.1.3 Capacitive Transduction

Capacitive-type ultrasonic sensor elements have been chosen to constitute the elements of the developed sensor microarray. They feature a low mechanical impedance that allows broadband operation even in immersion applications, and fabrication techniques that vastly simplify integration of driving and control electronics on die. Capacitive sensing provides a technique for the precise sensing of movement using simple structures. These structures consist of one or more fixed electrodes and one or more moving electrodes. Capacitive sensors are generally marked by a cross-dependence with temperature and non-linearity across the sensing range. A simple conceptual diagram of a capacitive type acoustical sensor is shown in Figure 4.2.

For a parallel plate capacitor (neglecting fringing fields), the capacitance is given by:

$$C = \frac{\epsilon_o \epsilon_r A}{d} \quad (4.2)$$

where C is the capacitance in Farads, ϵ_o is the permittivity of free space, ϵ_r is the relative permittivity, A is the exposed face area and d is the distance between the plates. As d varies,

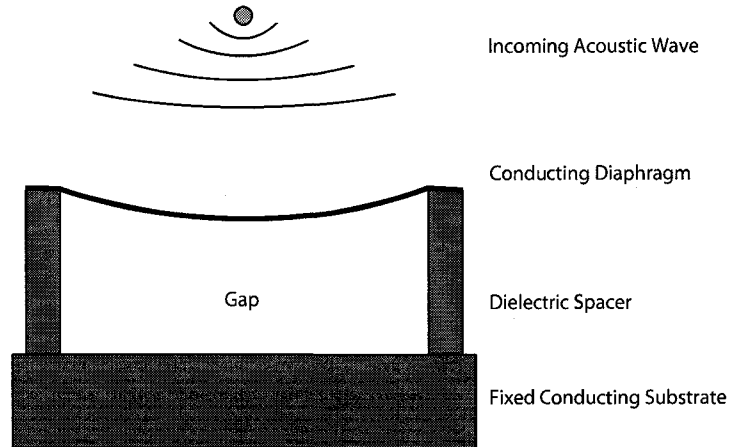


Figure 4.2: A Schematic View of a Capacitive Sensor

the capacitance will also vary non-linearly due to the $\frac{1}{d}$ term present in (4.2). A limitation of these sensors is the dependence of d , A and ϵ_r on temperature. Capacitive sensors are simple to manufacture, and sensors based on structures containing deformable membranes are typically used. Capacitive sensing techniques are intrinsically less noise-prone than piezoresistive techniques due to a lack of Johnson noise [38, 39].

The values of capacitance change found in MEMS capacitive sensors are typically extremely small, in the low femto-farad or even in the atto-farad range. There are a variety of techniques capable of measuring these small capacitive changes. As an alternative to a custom-designed sensing circuit, there are a variety of commercially available sensing IC's capable of measuring changes in this range [30].

4.2 Modeling Levels

In order to facilitate the design of a complex system such as a MEMS microarray, several different modeling levels are needed. A top down design philosophy was applied. Initially system-level modeling is used to verify array functionality and determine the desired operating parameters that form the constraints for lower level design. Here beamforming theory based on the hyperboloid paraboloid is extended to include discrete implementations, and performance criteria are developed. This stage determines overall array geometry. Modeling at this level was approached from two separate directions and both were implemented in MatlabTM. The first method is based on comparing

the resulting array factor for the discrete array against the continuous hyperbolic paraboloid. This facilitated the exploration of parameters introduced by the discretization process such as sensors per axis. The effects of geometrical approximation quality are also explored. The second method models the array to be constructed using point-source-like sensor elements with omnidirectional receiving characteristics in a 3-D space and calculates the response of an impinging plane wave based on wave propagation delay in the media. The two models provide cross verification of the array function, while the second model also allows the exploration of the effects of element misalignment and inter-element spacing.

Once the geometry of the array and the number of sensing elements are determined through array-level modeling, transducer-level modeling is used to determine the geometry of individual transducers within each sensing surface. Lumped element modeling is used to reduce geometric complexity to a manageable level for rapid simulation and specification refinement. The lumped element model uses the constraints defined by the array-level model as well as pre-existing constraints from the fabrication process limitations to determine the geometry and performance of the sensing elements. This lumped element modeling determines the total number and spacing of sensors within each sensing surface.

The lumped element modeling is able to optimize the performance of individual sensor elements. This includes modeling of all major diaphragm performance criteria such as, load-deflection characteristics, pull-in voltage, resonant frequency, damping effects, and a reliability study based on the Coulomb–Mohr criteria.

Lumped element analysis is performed using Matlab™. Once the lumped element model has been optimized, it is verified by 3-D electromechanical Finite Element Analysis (FEA) using Intellisuite™ and Adina™ where appropriate. The FEA analysis shows excellent agreement with the behavior predicted by the lumped element model in all major performance criteria.

A complete set of geometries are now available from the modeling performed. Array details are presented in Figure 4.3, illustrating the relation between modeling levels as well as the scope of each level.

4.3 Lumped Element Modeling

MEMS-based acoustical sensors typically are fabricated using a combination of surface and bulk micromachining techniques [40]. Of the different MEMS-based acoustical sensors, the capacitive-type offer the highest sensitivity while maintaining lower power consumption. Capacitive sensors operat-

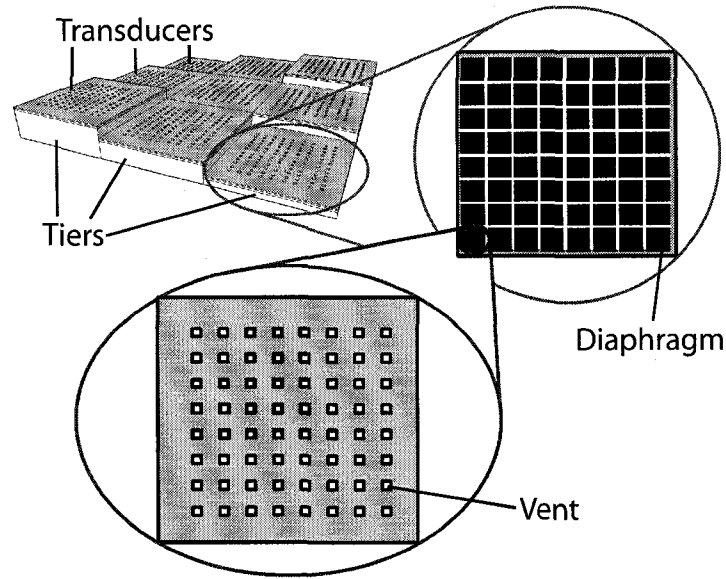


Figure 4.3: Array Modeling Details: Beamforming Array - Transducer - Diaphragm

ing in a voltage controlled regime are subject to limited dynamic range and non-linear response due to the pull-in effect. Pull-in results in diaphragm collapse as the electrostatic force from the bias voltage overcomes the elastic restoring force of the diaphragm. Additionally, MEMS-based ultrasonic transducers differ in important ways from traditional piezoelectric transducers. These include drastically different acoustic impedances leading to vastly different coupling responses. Accurate modeling of damping at the MEMS scale also becomes more important as the scale of the air gaps lead to powerful squeezed film damping effects [41].

The geometric and energy transduction complexity associated with micromachined transducers mandate the creation of a reduced-order model (lumped element) to facilitate early design decisions. This reduced-order model will allow the rapid optimization of the geometry [42, 43].

An analog electrical circuit equivalent of the capacitive type acoustical sensor shown in Figure 4.2 is shown in Figure 4.4. This circuit makes it possible to determine the sensor's mechanical and electrical sensitivity, frequency response, noise floor, and pull-in voltage in a computationally inexpensive way compared to finite element methods. The sensor's sensitivity is a strong function of both diaphragm size and residual stress [42, 44].

The acoustic force, F_{sound} is modeled as equivalent voltage source, The radiative resistance is R_r . The air mass in contact with the diaphragm subject to displacement is represented by M_r .

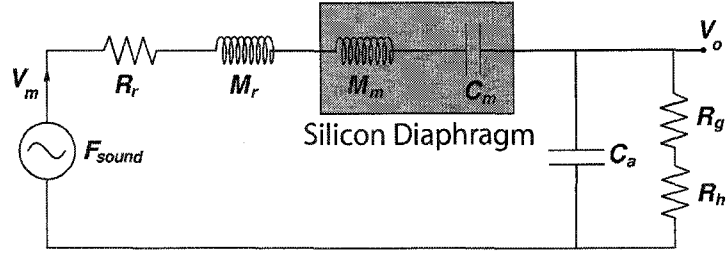


Figure 4.4: Equivalent Circuit Model

The mechanical mass of the diaphragm is M_m and the diaphragm compliance, the inverse of the diaphragm stiffness (spring constant), is expressed as C_m . The air gap and vent losses are represented by the viscous resistances R_g and R_h , and air gap compliance is represented by C_a . These parameters are defined as:

$$R_r = \frac{\rho_o a^4 \omega^4}{2\pi c} \quad (4.3)$$

$$M_r = \frac{8\rho_o a^3}{3\pi\sqrt{\pi}} \quad (4.4)$$

Where ρ_o is the air density, a is the diaphragm side length, ω is the angular vibration frequency ($2\pi f$) and c is the velocity of sound in the media at the frequency ω .

$$C_m = \frac{32a^4}{\pi^6(2\pi^2 D + a^2 T)} \quad (4.5)$$

$$M_m = \frac{\pi^4 \rho(2\pi^2 D + a^2 T)}{64T} \quad (4.6)$$

where D is the flexural rigidity, and T is the tensive force per unit length. Viscosity losses in the air gap R_g , vent holes R_h , and the gap compliance C_a , are given as:

$$R_g = \frac{12\eta a^2}{nd^3\pi} \left(\frac{\alpha}{2} - \frac{\alpha^2}{8} - \frac{\ln(\alpha)}{4} - \frac{3}{8} \right) \quad (4.7)$$

$$R_h \approx \frac{8\eta h a^2}{\pi n r^4} \quad (4.8)$$

$$C_a = \frac{d}{\rho_o c^2 \alpha^2 a^2} \quad (4.9)$$

where n is the hole density in the backplate, α is the surface fraction occupied by the holes, η is the air viscosity coefficient, d is the average air gap distance, h is the vent height and r is the effective radius of the vent holes. From these definitions we can express the equivalent impedance of the circuit as:

$$Z_t = R_r + j\omega(M_r + M_m) + \frac{1}{j\omega C_m} + \frac{R_g + R_h}{1 + j\omega(R_g + R_h)C_a} \quad (4.10)$$

The total sensitivity of the system is the output voltage under the presence of the acoustical pressure loading, or

$$S_t = \frac{V_o}{P} = \frac{V_b \cdot a^2}{j\omega d Z_t} \quad (4.11)$$

where P is the sound pressure and V_b is the bias voltage.

The sensitivity presented above lumps the electrical and mechanical components of the system together. This illustrates how the sensitivity scales linearly with bias voltage, but does not clearly show the mechanical sensitivity. By separating the sensitivity model between the mechanical and electrical components of the transducer, each component can be evaluated and optimized independently [45]. The mechanical sensitivity can be given in $\mu\text{m}/\mu\text{N}$ as:

$$S_z = \frac{1}{\frac{1}{C_a} + \frac{1}{C_m}} \quad (4.12)$$

In order to accurately determine the capacitance change from an impinging acoustic wave, the biased capacitance must be known. When the bias voltage is applied, the diaphragm deforms slightly under the electrostatic force, changing the air gap. In order to solve for the capacitance accurately, the air gap of the biased diaphragm must be known. This can be determined by solving (4.13) and (4.14) for its largest stable root ($Z_m < 1/3d_o$); where d_o is the unbiased air gap [45].

$$F_z(V_o) = \frac{\epsilon_o V^2 b^2}{2(d_o - Z_m)^2} \quad (4.13)$$

$$F_z = K Z_m \quad (4.14)$$

$$K = \frac{1}{C_a} + \frac{1}{C_m}$$

Once the mechanical force is known, along with the diaphragm displacement due to bias voltage, the capacitance change due to the bias voltage can be determined as:

$$\Delta C = \frac{\epsilon b^2 S_z}{d_o^2} F_z \quad (4.15)$$

Voltage-controlled, electrostatically-actuated diaphragms suffer from non-linear effects that limit their dynamic range. This effect, known as “pull-in,” results from the electrostatic force overcoming the mechanical-restoring force. The pull-in voltage is a critical performance metric for capacitive sensors. The pull-in voltage for an ideal parallel-plate sensor is given as (4.16).

$$V_{pi} = \sqrt{\frac{8Kd^3}{27\epsilon A}} \quad (4.16)$$

where K is the equivalent spring constant, ϵ is the permittivity of the media, and A is the diaphragm area. Unfortunately equation 4.16 provides only a rough estimate and frequently suffers from greater than 30% error. Due to the importance of this parameter on overall system performance an accurate value for pull-in is required. The pull-in voltage can be expressed accurately within 4% as [46]:

$$V_{pi} = \sqrt{\frac{6d_o^2}{5\epsilon} \left(C_1 \frac{t_d \sigma}{b^2} \left(\frac{d_o}{3} \right) + C_2(v) \frac{t_d \hat{E}}{b^4} \left(\frac{d_o}{3} \right)^3 \right)} \quad (4.17)$$

where t_d is the diaphragm thickness, E is the Young’s modulus, ν is the Poisson’s ratio, σ is the residual stress, and b is half the diaphragm side length. C_1 and C_2 are numerical fitting parameters defined as:

$$C_1 = 3.45 \quad (4.18)$$

$$C_2 = 1.994(1 - 0.271\nu)/(1 - \nu)$$

When using square-clamped diaphragms, the effective Young’s modulus is used. This is given as:

$$\hat{E} = E/(1 - \nu^2) \quad (4.19)$$

Another key factor in designing a capacitive sensor for high-frequency use is to control the damping in the airgap. Each damping source introduces a source of mechanical noise proportional to the damping [38]. One of the better known mechanisms for mechanical-thermal noise is *Brownian motion*. *Brownian motion* is the random motion of objects due to collisions with molecules in the media. Here observable agitation of the diaphragm is caused by molecular collisions within the

surrounding media. The agitation is directly related to the viscosity and temperature of the media. While in many designs it is assumed that preamplifier noise will dominate the sensor noise floor, this is not always true in microsystems and in particular capacitive-type acoustical MEMS sensors. Although several schemes are available for decreasing electrical noise by adjusting the driving circuit of a transducer, the effect of mechanical-thermal noise must be addressed during the design stage. As the operating frequency increases, squeeze-film and other damping effects can become severe, and must be addressed. In order to determine the effects of mechanical-thermal noise in the system, the total mechanical damping is determined, and the equivalent noise pressure can be calculated as:

$$P_n = \sqrt{4K_b T_k R_{ac} F_c} \quad (4.20)$$

Acoustic Noise Floor in dB/SPL:

$$NF_{ab/SPL} = 20 \log \left(\frac{P_n}{20 \times 10^{-6}} \right) \quad (4.21)$$

Given:

$$R_n = R_g + R_h \quad (4.22)$$

$$R_{ac} = \frac{R}{(a^2)^2} \quad (4.23)$$

$$F_c = \frac{\pi \omega}{2 \cdot 2\pi} \quad (4.24)$$

Where R_n is the damping contributing to noise, R_{ac} is a measure of the damping vs. the diaphragm area, and F_c is the cut-off frequency for noise analysis.

4.3.1 Reliability Study

In order to ensure that the diaphragms are able to withstand the strain associated with the total applied electrostatic and mechanical forces, a study of the applied stress was included in the lumped element analysis [47]. In MEMS mechanical analysis there are two relatively well-accepted yield criteria, the maximum shear stress criterion (also known as Tresca criteria) and the octahedral shear stress criterion (also known as Maximum Distortional Energy or Von Mises criteria). The simplest yield criteria states that yield failure is expected when the greatest shear stress reaches the shear strength of the material. From this, we can state the maximum shear stress yield criterion as (4.25).

$$\text{MAX} \left[\left| \tau_{12} = \frac{(\sigma_1 - \sigma_2)}{2} \right|, \left| \tau_{13} = \frac{(\sigma_1 - \sigma_3)}{2} \right|, \left| \tau_{23} = \frac{(\sigma_2 - \sigma_3)}{2} \right| \right] \geq \left(\tau_o = \frac{\sigma_o}{2} \right) \quad (4.25)$$

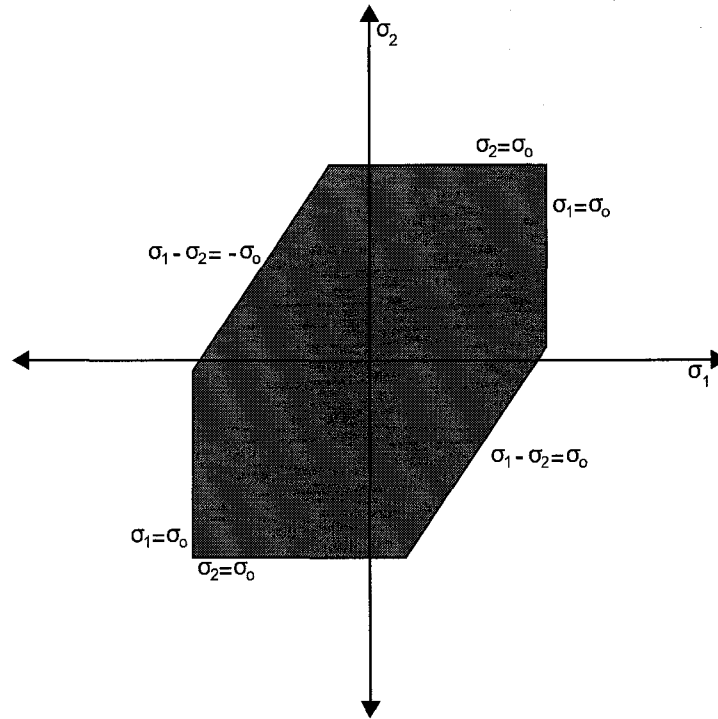


Figure 4.5: Maximum Shear Stress Theory – Safe Area for in Plane Stress

where σ_1 , σ_2 and σ_3 are principal stresses, σ_o is the yield stress, τ_o is the shear stress at yield, and the MAX function returns the largest listed value. If the inequality in (4.25) is satisfied, the structure under test will fail.

In order to ensure safe operation, devices are designed to operate using only a fraction of their yield strength. This operating fraction is referred to as the safety factor, and can be defined by expressing (4.25) as (4.26):

$$FS = \frac{\left(\tau_o = \frac{\sigma_o}{2} \right)}{\text{MAX} \left[\left| \tau_{12} = \frac{(\sigma_1 - \sigma_2)}{2} \right|, \left| \tau_{13} = \frac{(\sigma_1 - \sigma_3)}{2} \right|, \left| \tau_{23} = \frac{(\sigma_2 - \sigma_3)}{2} \right| \right]} \quad (4.26)$$

Graphically, the yield criteria for an in plane stress state ($\sigma_3 = 0$, σ_1 and σ_2 are the ordinate and abscissa directions respectively) can be expressed as Figure 4.5. For all combinations of σ_1 and σ_2 which plot within the parallelogram are considered 'safe'. The perimeter is considered the yield point. The safe area of the maximum shear stress criterion is shown shaded for comparison.

When performing this analysis, three cases arise; both stresses are compressive, one stress is

tensile and the other compressive, and both stresses are tensile. These cases are shown in (4.27), (4.28) and (4.29) respectively.

$$\sigma_1 > \sigma_2 > 0 \quad \tau_{max} = \frac{\sigma_1 - 0}{2} = \frac{S_{UT}}{2} \text{ or } \sigma_1 = \sigma_o \quad (4.27)$$

$$\sigma_1 > 0 > \sigma_2 \quad \tau_{max} = \frac{\sigma_1 - \sigma_2}{2} = \frac{S_{UT}}{2} \text{ or } \sigma_1 - \sigma_2 = \sigma_o \quad (4.28)$$

$$0 > \sigma_1 > \sigma_2 \quad \tau_{max} = \frac{0 - \sigma_2}{2} = \frac{S_{UT}}{2} \text{ or } \sigma_2 = -\sigma_o \quad (4.29)$$

The octahedral shear stress criterion provides another method of predicting the yield failure in ductile materials. In this criteria, failure is expected when the octahedral shear stress (τ_h) of the structure reaches the octahedral shear yield stress (τ_{ho}) of the material. This criterion can be specified as (4.30).

$$\left(\tau_{ho} = \frac{\sqrt{2}}{3} \sigma_o \right) \leq \left(\tau_h = \frac{1}{3} \sqrt{(\sigma_1 - \sigma_2)^2 + (\sigma_2 - \sigma_3)^2 + (\sigma_3 - \sigma_1)^2} \right) \quad (4.30)$$

Where τ_{ho} is defined in terms of the uniaxial yield strength. Graphically, the safe area is shown in Figure 4.6. Here, any stress combination which plots within the ellipse is considered safe, and the perimeter is the yield point.

For Ductile materials such as steel and aluminum, the actual failure point falls between the maximum shear stress and the octahedral shear stress criteria envelopes. The maximum difference between the two criteria is approximately 15%. It is often advisable to use the more conservative value provided by the maximum shear stress criterion.

The Intellisuite™ FEA environment supports the Von-Mises criterion for determining if a structure is at risk of rupture. This criterion is designed for use with ductile materials, and as such is of limited value in this analysis. It is based on the determination of the distortion energy in a given material. This energy is the energy associated with a change in shape for the material (as opposed to a change in volume). As long as the energy remains below the distortion energy per unit volume associated with yield for that material the structure is considered safe.

Brittle materials exhibit a non-distinct point of yielding (plastic deformation). In terms of ultimate strength, brittle materials tend to fail in tension mode when loaded in tension. Conversely when loaded in compression, they tend to fail in a shear mode [48]. Additionally the required loading for failure in compression is generally higher than for tension. In order to accommodate this, the maximum-shear stress theory is modified to the Coulomb-Mohr theory of failure.

The Coulomb-Mohr criterion is a graphical method used to predict the effects of a given plane

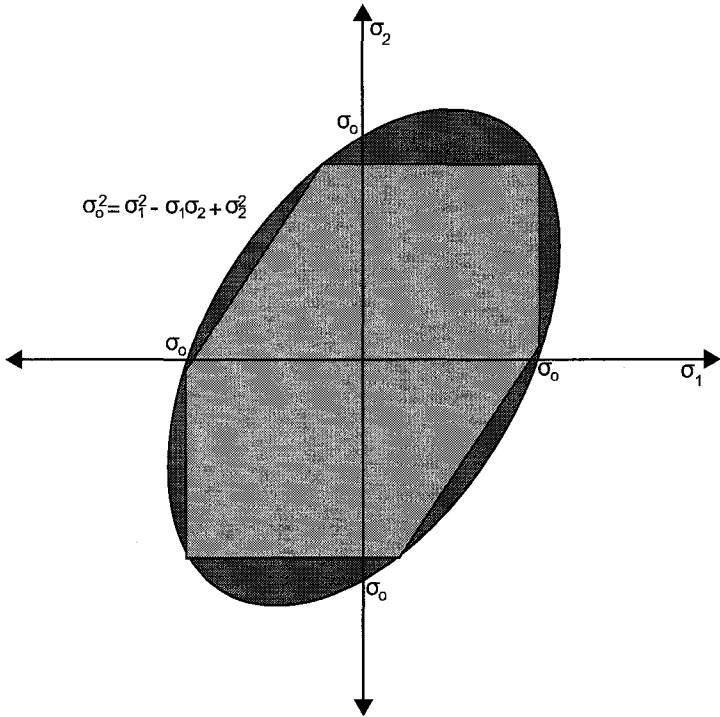


Figure 4.6: Octahedral Shear Stress Theory - Safe Area for in Plane Stress

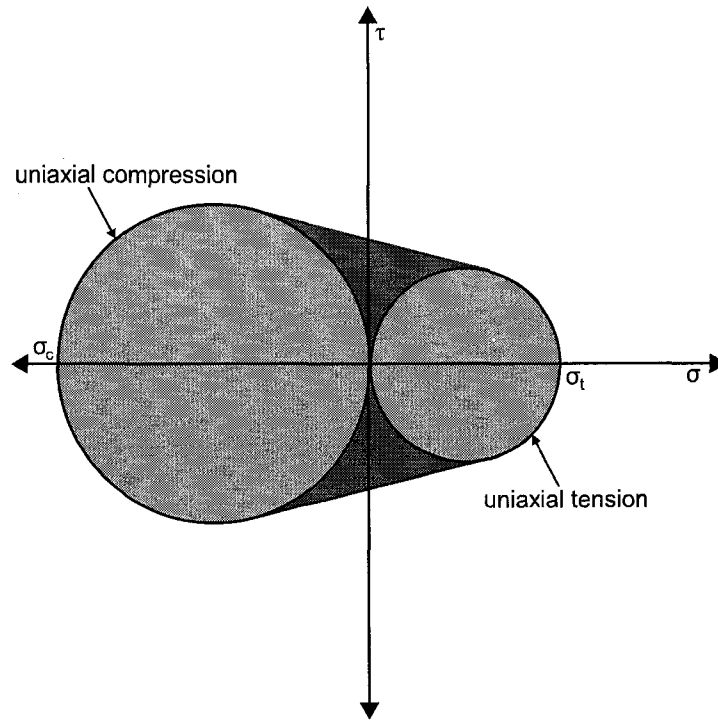


Figure 4.7: Coulomb-Mohr Criteria – Safe Area for Plane Stress

stress on a brittle material. In order to use this criteria, the ultimate stress (stress at rupture) in compression (σ_c) and tension (σ_t) must be known. The accuracy of this method can be enhanced if additional test data such as a torsional test is available for the material. The method is shown in Figure 4.7. Stresses in all shaded areas are considered safe.

This technique tends to predict conservative results [48]. For conditions where the plane stress is positive along both axes the Coulomb-Mohr criteria can be stated as (4.31). For conditions where the plane stress is negative along both axes, equation (4.32) is to be used. In the event the stress in the axes have opposite signs, a full analysis is required including results from the torsional material test [49, 50].

$$\sigma_x < \sigma_t \quad (4.31)$$

$$\sigma_y < \sigma_t$$

$$|\sigma_x| < |\sigma_c| \quad (4.32)$$

$$|\sigma_y| < |\sigma_c|$$

In the analysis performed on the sensor elements a safety factor of 2 was used for all calculations to ensure safe operation even under abnormal operating conditions.

4.3.2 Lumped Element Results

The lumped element model presented in the previous section was simulated using MatlabTM. Complete code is available in Appendix A. The 3×3 array uses the dimensions listed in Table 4.2. Use of the lumped element model on these dimensions produces a design with the performance specifications shown in Table 4.3.

TABLE 4.2: 3×3 ARRAY DIAPHRAGM DESIGN SPECIFICATIONS

| Specification | Value |
|----------------------|-------------------|
| Diaphragm Thickness | 2.0 μm |
| Diaphragm Airgap | 1.0 μm |
| Diaphragm Sidelength | 300 μm |
| Vent Hole Radius | 10 μm |
| Number of Vent Holes | 64 |
| Tier Sidelength | 3.0 mm |
| Diaphragms per Tier | 64 |
| Bias Voltage | 12.0 V |

For the 29×29 element array, a monolithic fabrication process is required due to the small area available for each sensing element, and the high number of sensing surfaces present in the array. Capacitive sensors using silicon nitride (Si_3N_4) diaphragms have a proven record operating at these dimensions and so are chosen for use here [51]. Estimated sensor surface parameters are shown in Table 4.4. Applying the lumped element model presented earlier this chapter to this design yields performance results summarized in Table 4.5.

TABLE 4.3: LUMPED ELEMENT MODELING RESULTS FOR 3×3 ARRAY

| Parameter | Value | Unit |
|--|--------|------------------------|
| Pull-in Voltage | 20.63 | V |
| Unbiased Tier Capacitance | 50.97 | pF |
| Resonant Frequency | 323.5 | kHz |
| Maximum Stress at Operating Pressure | 6.457 | kPa |
| Coulomb-Mohr Rupture Limit (factor of safety: 2) | 12.39 | MPa |
| Mechanical Sensitivity | 374.76 | $\mu\text{m}/\text{N}$ |
| Capacitance Change per Tier | 2.265 | pF/Pa @ 140 kHz |
| Total Tier Sensitivity | 35.41 | mV/Pa |
| Percentage of Diaphragm Occupied by Vent Holes | 7.11 | % |

TABLE 4.4: 29×29 ARRAY DIAPHRAGM DESIGN PARAMETERS

| Specification | Value | Unit |
|--------------------------------|-------|---------------|
| Diaphragm Thickness | 0.15 | μm |
| Diaphragm Airgap | 0.40 | μm |
| Diaphragm SideLength | 40 | μm |
| Vent Hole Radius | 1 | μm |
| Number of Vent Holes | 225 | |
| Diaphragms per Sensing Surface | 1 | |
| Bias Voltage | 25.0 | V |

TABLE 4.5: LUMPED ELEMENT MODELING RESULTS FOR 29×29 ARRAY

| Parameter | Value | Unit |
|--|--------|------------------------|
| Pull-in Voltage | 31.30 | V |
| Unbiased Tier Capacitance | 0.0354 | pF |
| Resonant Frequency | 31.661 | MHz |
| Maximum Stress @ Operating Pressure | 20.04 | MPa |
| Coulomb-Mohr Rupture Limit (Safety Factor:2) | 7.10 | MPa |
| Mechanical Sensitivity | 853.0 | $\mu\text{m}/\text{N}$ |
| Capacitance Change per Diaphragm | 2.40 | fF/Pa @ 3.75 MHz |
| Total Array Sensitivity | 160.3 | mV/Pa |
| Percentage of Diaphragm Occupied by Vent Holes | 14.1 | % |

4.4 Finite Element Analysis

Finite element analysis (FEA) is a detailed and accurate method to simulate arbitrary geometries. This capability was used to permit more accurate modeling of device behavior based on the results of the lumped element model. Several areas of interest were examined, including resonant frequency, pull-in voltage, capacitance change and mechanical operating strain.

4.4.1 Resonant Frequency

The resonant frequency provides a method to determine the frequencies of maximum mechanical sensitivity. Actuation at these frequencies will see the largest displacement-to-force ratios, but also tend to be vulnerable to ringing effects. Actuation significantly below this frequency tends to yield acceptable sensitivity numbers, however above the resonant frequency damping effects grow extremely quickly resulting in extremely poor sensitivities. Finite element analysis was performed using both the IntelliSuiteTM and AdinaTM finite element suites. Results are shown in Table 4.6.

From the data presented in Table 4.6, it can be seen that the resonant frequency is well above the operating frequency. This ensures that acceptable sensitivities will be obtained while reducing ringing effects. The FEA results support the analytical model within 2.5%.

TABLE 4.6: LUMPED ELEMENT MODELING RESULTS FOR 29×29 ARRAY

| First Resonant Frequency | | |
|--------------------------|-----------------|-------------|
| Analysis Package | Frequency (kHz) | % Variation |
| Intellisuite | 632.54 | 2.23 |
| Adina | 631.02 | 2.47 |
| Lumped Element | 647.00 | - |

| Second Resonant Frequency | | |
|---------------------------|-----------------|-------------|
| Analysis Package | Frequency (kHz) | % Variation |
| Intellisuite | 1290.90 | - |
| Adina | 1284.90 | -0.47 |

| Third Resonant Frequency | | |
|--------------------------|-----------------|-------------|
| Analysis Package | Frequency (kHz) | % Variation |
| Intellisuite | 1290.90 | - |
| Adina | 1284.90 | -0.47 |

4.4.2 Pull-In Voltage

Equation (4.17) predicted the pull-in voltage extremely well as shown in Figure 4.8. The venting holes did not present a significant source of discrepancy between the lumped-element and FEA analysis as was present in the mechanical stress analysis. The lumped element model predicts a pull-in voltage of 20.6V. The two numbers were found in agreement within 4%.

4.4.3 Capacitance Change Over Actuation Range

The predicted capacitance change over the actuation range is shown in Table 4.7 for the lumped element model as well as for the Intellisuite simulations. This shows the total capacitance change is easily large enough to be measured with good accuracy.

TABLE 4.7: CAPACITANCE CHANGE ANALYSIS

| Analysis Method | Capacitance Change | Variation |
|----------------------|--------------------|-----------|
| Lumped Element Model | 17.94 fF | - |
| Intellisuite | 42.30 fF | 3.7 dB |

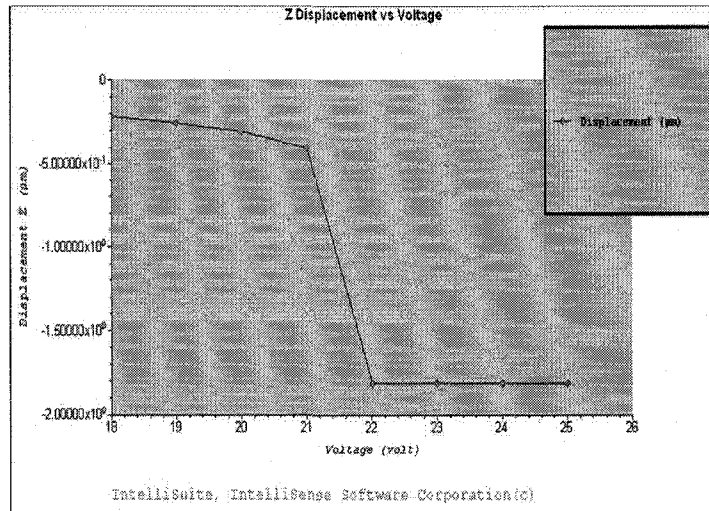


Figure 4.8: Finite Element Pull-In Voltage Prediction using IntelliSuite

4.4.4 Maximum Displacement

The maximum displacement at the operating pressure and bias voltage is an important measure of how close to collapse the diaphragm is. This is due to the dynamic range restriction imposed by the voltage-based control methodology used for the sensing scheme. The unbiased gap is $1 \mu\text{m}$ nominally. Intellisuite simulations show that the bias voltage causes a displacement of $0.026 \mu\text{m}$. This accounts for 7.7% of the dynamic operating range. The displacement is shown in Figure 4.9.

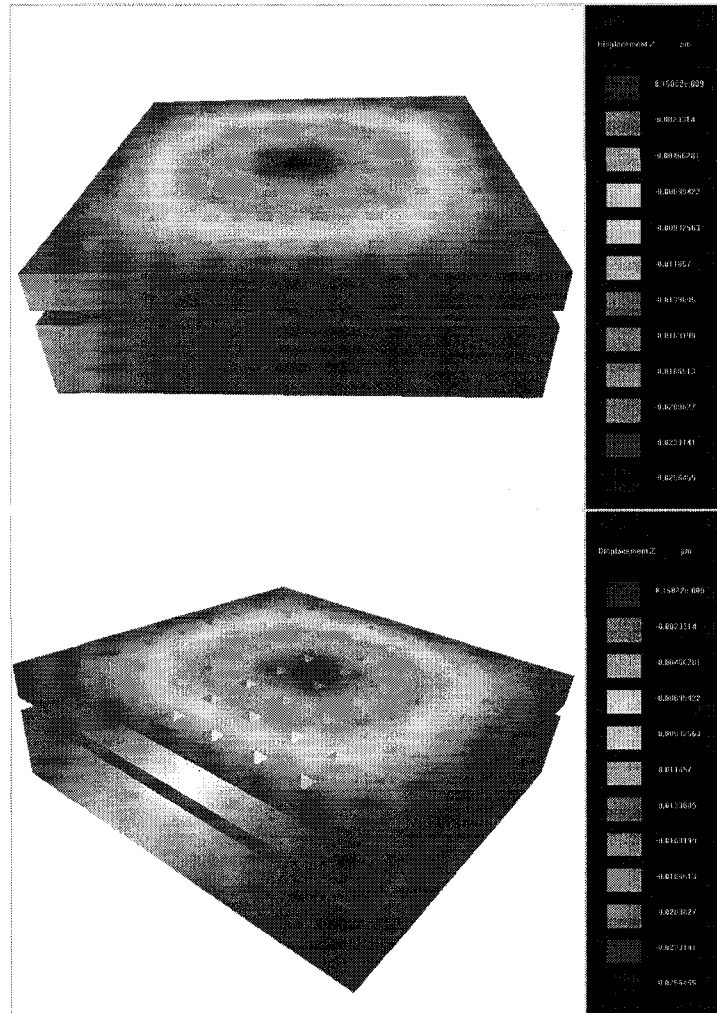


Figure 4.9: Maximum Displacement

Chapter 5

Fabrication

This chapter presents the fabrication methodology developed to fabricate the sensor microarray. The methodology incorporates standard foundry processes available in microfabrication facilities. Fabrication process tables and necessary mask sets have been developed and simulated in IntelliSuite to check for process and geometry compatibility. After simulating the process table, a 3-D model of the sensor geometry has been generated and is in excellent agreement with design requirements. A brief overview of the major fabrication processes has been presented followed by a detailed description of the fabrication process needed for the array. The step-by-step fabrication process is described with 3-D cross-sectional images generated by IntelliSuite. The 3-D cross-sections are cross-verified with the conceptual geometry design.

5.1 Array Fabrication Details

This section describes the fabrication process for the IAVSS array design as described previously. The array is designed to have 3 sensing surfaces in both the x and y direction. The nine sensing surfaces are fabricated on SOI wafers. After dicing, the sensing surface dies are to be assembled using shim wafers in order to ensure appropriate elevations are met. The wafers used are $\langle 100 \rangle$ oriented silicon-on-insulator (SOI) wafers with a 2-side polish, and a conductivity of less than $100\Omega/\text{cm}$. The wafer handle, insulating layer and device layer are $525 \pm 10\mu\text{m}$, $1 \pm 5\%\mu\text{m}$, and $2 \pm 0.1\mu\text{m}$ thick respectively. The complete fabrication process consists of 8 major steps. The fabrication process

involves the deposition of silicon, chromium, gold, and photoresist. The colors associated with these materials are shown in Figure 5.1.

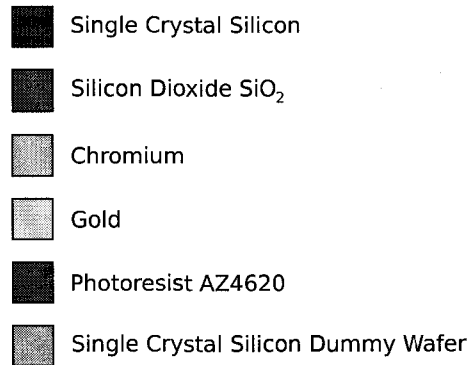


Figure 5.1: Fabrication Material Legend

5.1.1 Stage 1: Wafer Preparation

Upon delivery the wafers are subject to a three-stage RCA cleaning procedure. The first stage will remove all organic contamination. The wafers are submerged in a 5:1:1 solution of H₂O:H₂O₂:NH₄OH at 75°C for 10 minutes then rinsed by submersion three times. The second stage strips the native oxide from the wafer surfaces. The amount of material removed is suitably small so as not to damage the insulating layer. For this stage the wafers are submerged in a 50:1 solution of H₂O:HF at 25 C for 15 seconds then rinsed by submersion three times. Finally, the wafer is subjected to an ion strip clean to remove any ionic or heavy metal contamination. The wafer is submerged in a 6:1:1 solution of H₂O:H₂O₂:HCl at 75°C for 10 minutes and then rinsed [52].

5.1.2 Stage 2: PVD Metal Deposition

Starting with the cleaned wafers, a 10 nm seed layer of chromium is deposited by a sputtering to provide an adhesion layer for the gold conducting layer. The chamber pressure for the deposition is 1×10^{-5} Torr with an argon flow rate of 30 sccm and a pressure of 7 mTorr. The RF power used is 300 watts. After this deposition is complete 200 nm of gold is deposited using the same recipe [53]. Figure 5.3.a shows a conceptual cross-section of the device and Figure 5.3.b shows a 3-D model of the structure at this stage after simulating the fabrication process steps described above.

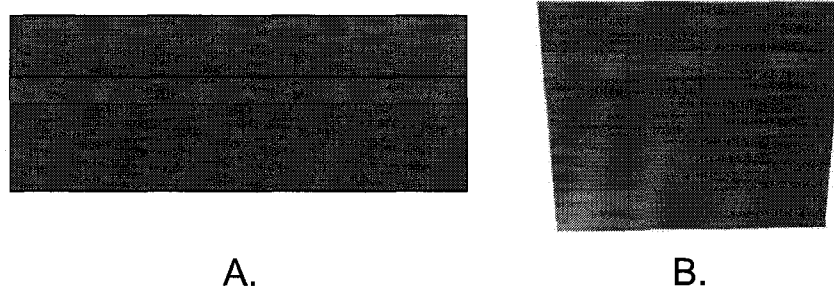


Figure 5.2: Stage 1 Fabrication Details. (A) Conceptual Cross-Section, (B) IntelliSuite Generated 3-D model After Simulating the Described Fabrication Process Steps

5.1.3 Stage 3: Lithography

AZ4620, a positive photoresist, is used to provide the pattern for the diaphragms during all subsequent etch steps. 8.0 ml of AZ4620 photoresist is spun onto the wafer during a 10 second 500 RPM spread stage. The wafer is then spun for 25 seconds at 2000 RPM to create a uniform $12.5 \mu\text{m}$ thick resist layer. The wafer is then floated on a N_2 cushion over a hotplate at 100°C for 90 seconds. Following this, the wafer is affixed to the hotplate via a vacuum chuck and baked for an additional 60 seconds. The wafers are then placed in a humid environment at room temperature for 2 hours to allow rehydration of the photoresist. Wafers are then optically aligned on contact lithography apparatus and exposed to a 730 mJ dose of UV radiation. The photoresist is then developed using a developer solution of 1:4 AZ400K: H_2O for 1 minute, 20 seconds. The resulting resist thickness maintains a uniform sidewall profile for features down to $2 \mu\text{m}$, well below our minimum feature size

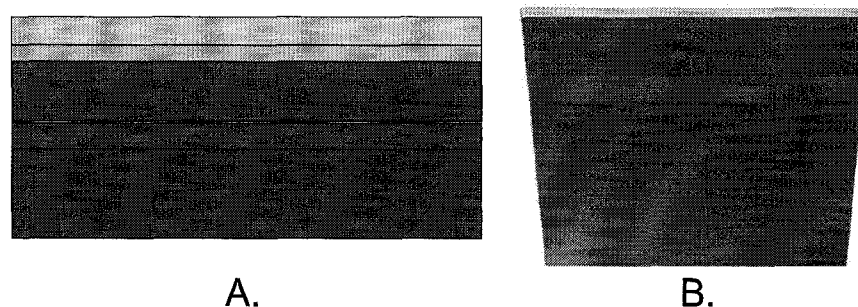


Figure 5.3: Stage 2 Fabrication Details. (A) Conceptual Cross-Section, (B) IntelliSuite Generated 3-D model After Simulating the Described Fabrication Process Steps

of $10\ \mu\text{m}$ [54].

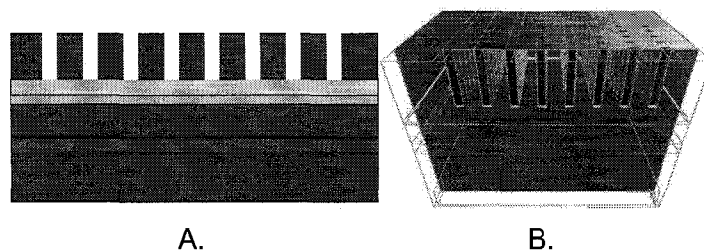


Figure 5.4: Stage 3 Fabrication Details. (A) Conceptual Cross-Section, (B) IntelliSuite Generated 3-D model After Simulating the Described Fabrication Process Steps

5.1.4 Stage 4: Metal Etching

The gold and chromium layers are now etched in preparation for etching the vent holes in the diaphragm. The gold is etched by submerging the wafer in a solution of potassium iodine (5:10:85 I:K:H₂O) for 50 seconds at 20°C. The wafer is rinsed for 1 minute in a low-pressure stream of de-ionized (DI) water. The chromium seed layer is then etched by submerging the wafer in a solution of dilute aqua regia (3:1:2 HCl:HNO₃:H₂O) for 10 seconds at 30°C. The wafer is again rinsed for 1 minute in a low-pressure stream of DI water [55]. The result of this step is shown in Figure 5.5.

5.1.5 Stage 5: Silicon Etch

The device layer is then etched to provide vents for static pressure equalization within the diaphragm as well as reducing damping from squeeze film effects. This also provides an avenue to allow for SiO₂ removal during the release stage. The silicon is etched using Bosch process DRIE. The Bosch DRIE process allows an anisotropic etch using a fluorine-based chemistry. The etch process consists of several cycles, each with 2 stages. In the first stage, the entire surface is coated with a Teflon-like polymer formed from C₄F₈ plasma for 10 seconds. In the second stage, SF₆ plasma etches quickly through the polymer and silicon vertically, while having a greatly reduced etch rate horizontally. The SF₆ etch stage lasts 15 seconds per cycle. The wafer is subjected to 6 cycles. The process is carried out in an Oxford ICP-RIE machine. For both stages the chamber pressure is held to 30 mTorr, RF power is 450 W, SF₆ and C₄F₈ flow rates are both 50 sccm. The deposition RF V_{bias} is held to less than 100 V [56]. The result of this stage is shown in Figure 5.6.

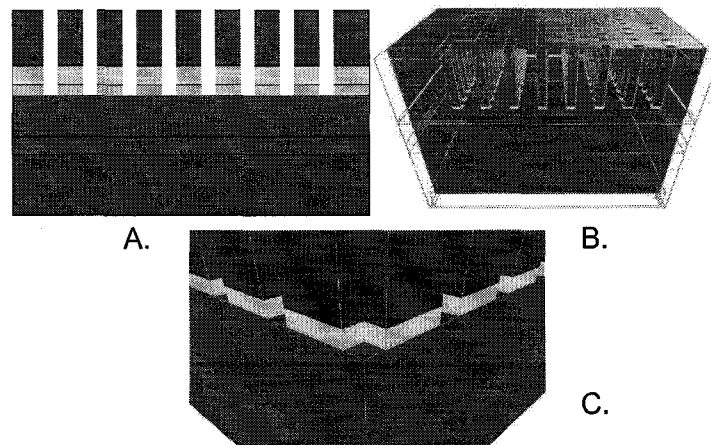


Figure 5.5: Stage 4 Fabrication Details. (A) Conceptual Cross-Section, (B) IntelliSuite Generated 3-D model After Simulating the Described Fabrication Process Steps, (C) Detail View of 3-D IntelliSuite Model

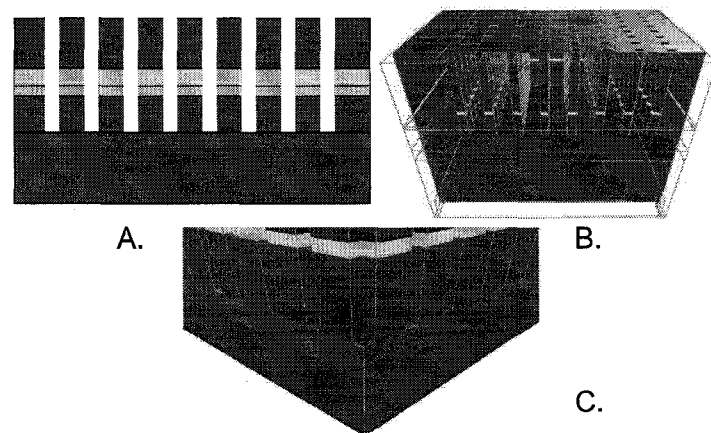


Figure 5.6: Stage 5 Fabrication Details. (A) Conceptual Cross-Section, (B) IntelliSuite Generated 3-D model After Simulating the Described Fabrication Process Steps, (C) Detail View of 3-D IntelliSuite Model

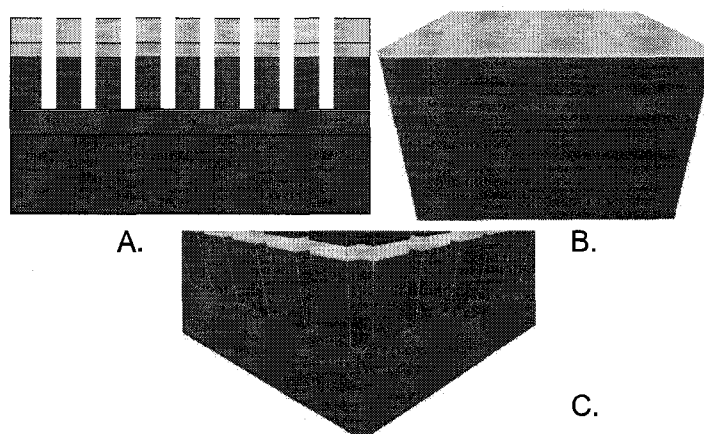


Figure 5.7: Stage 6 Fabrication Details. (A) Conceptual Cross-Section, (B) IntelliSuite Generated 3-D model After Simulating the Described Fabrication Process Steps, (C) Detail View of 3-D IntelliSuite Model

5.1.6 Stage 6: Photoresist Strip

Following both metal etching and the Bosch DRIE etch, the remaining photoresist is removed by an ashing process. The wafer is placed in a Plasmalab RIE chamber and exposed to oxygen plasma for 2 minutes. The result of this process step is shown in Figure 5.7.

5.1.7 Stage 7: Buffered Oxide Etch Diaphragm Release

The cleaned, etched wafer is then submerged in a Buffered Oxide Etch (BOE) solution – a solution of HF buffered with NH_4F to avoid the depletion of fluoride ions. BOE selectively etches SiO_2 without significantly etching single crystal Si. Removal of the SiO_2 layer will release the diaphragms. In order to accomplish this, significant undercut is necessary. BOE has a horizontal etch rate in thermal SiO_2 of 45 nm/min at room temperature [57]. The wafer is submerged in BOE for 5 hours 34 minutes without agitation. Upon completion, the wafers are rinsed by submersion in five baths of DI water while minimizing the amount of time the wafers are exposed to the air. The rinsed wafer is then submerged in isopropyl alcohol (IPA) for storage until drying. In order to avoid stiction issues, the wafer is transferred from the IPA into a CO_2 critical point dryer for drying. The result of this stage is shown in Figure 5.8.

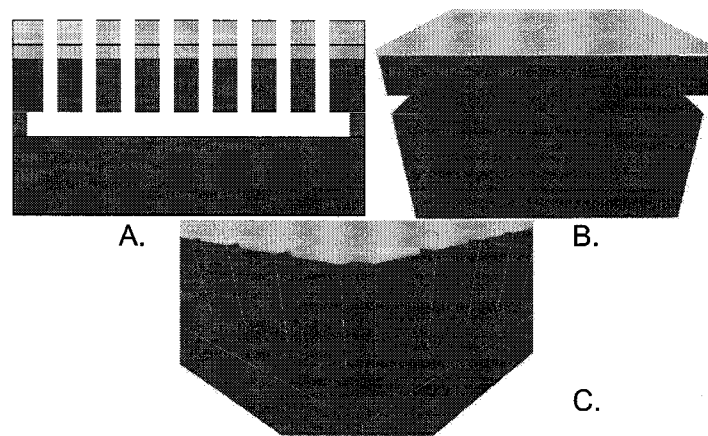


Figure 5.8: Stage 7 Fabrication Details. (A) Conceptual Cross-Section, (B) IntelliSuite Generated 3-D model After Simulating the Described Fabrication Process Steps, (C) Detail View of 3-D IntelliSuite Model

5.1.8 Stage 8: Array Assembly

After the wafers are dried, the wafers are to be diced and the individual dies are to be tested using a Wentworth probe station. After testing, the dies are assembled by using a silicon wafer to provide the required vertical offset for each tier. The handle is grounded by using conductive epoxy as the bonding materials. The individual tiers are assembled with an altitude and in-plane tolerances of $\pm 55 \mu\text{m}$. The completed array is then to be packaged in a PGA68 ceramic package with a $12\text{mm} \times 12\text{mm}$ die opening. Wirebonding is performed and the completed package is ready for final testing.

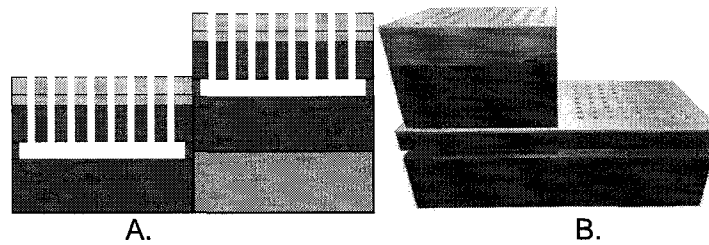


Figure 5.9: Stage 8 Fabrication Details. (A) Conceptual Cross-Section, (B) IntelliSuite Generated 3-D model After Simulating the Described Fabrication Process Steps.

5.2 Packaging Details

A requirement for packaging is the definition of bonding pads. These provide a connection point for wirebonding to the packaging, allowing external signals to be connected to the chip. The IAVSS element dies have their top layer covered in gold, which provides a suitable material for bonding. Unlike a traditional integrated circuit, where a specific bonding pad location is defined, a bonding ring $100\mu\text{m}$ wide is defined for bonding to the sensing elements. The ring is shown as the shaded region in Figure 5.10. Note that adjacent dies have electrically isolated metal layers. The actual connection can take place at any point along the ring. Additionally, due to the low number of I/O present in the design, each die is bonded to several pins. This increases the robustness of the design, because if a single bonding wire is damaged, the chip can continue to function normally through the alternate bonding sites. This is important, as the chip will be exposed to the environment without the benefit of a cover plate during testing. This is a requirement due to the acoustic sensing performed by the chip. The design of an acoustically-transparent cover plate that functions over a wide frequency range is exceedingly challenging and beyond the scope of the research undertaken. The gold (Au) wire thermo-sonic ball wirebonding technique outlined earlier in this chapter will be used for bonding on the sensor elements.

The IAVSS array will be hand assembled using the technique outlined earlier in the chapter. The IAVSS array is to be placed in a 68PGA package with a standard $10.2\text{ mm} \times 10.2\text{ mm}$ internal cavity. This package is available through the CMC. The dies are to be assembled as shown in Figure 5.10. The wirebonding details shown in Figure 5.10 are listed in Table 5.1. The dimensions of each die are given in Table 5.2. The array will be constructed on a silicon substrate. The individual dies used in the assembly of the array will each require a vertical offset. This vertical offset will be provided by additional sections of appropriately-sized silicon wafer. A cross-sectional view of die 1, 2 and 3 is shown in Figure 5.11. The wafers used to provide the vertical offset are to be $550 \pm 10\ \mu\text{m}$ thick. The bond height uniformity of the epoxy is to be $\pm 5\ \mu\text{m}$. This creates a maximum height variability of less than 3% of the height of a single sensor die. The number of height offset wafers required for each sensor die is detailed in Table 5.3.

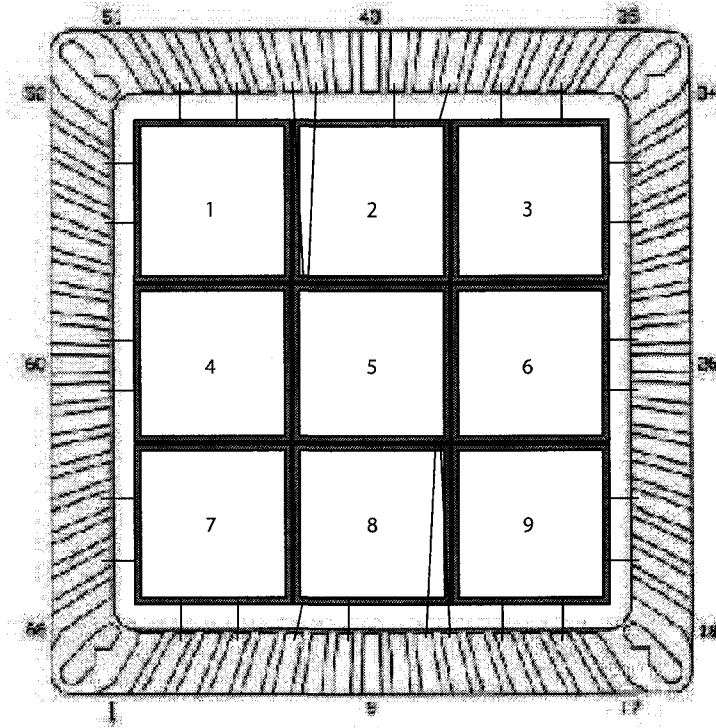


Figure 5.10: Wirebonding Bonding Diagram



Figure 5.11: Cross-Section of Die 1, 2 and 3 Showing Arrangement of Shims

TABLE 5.1: WIREBONDING DIAGRAM DETAILS

| Pin | Die # |
|-----|-------|-----|-------|-----|-------|-----|-------|
| 2 | 7 | 16 | 9 | 36 | 3 | 50 | 1 |
| 4 | 7 | 19 | 9 | 28 | 3 | 53 | 1 |
| 6 | 8 | 21 | 9 | 40 | 2 | 55 | 1 |
| 8 | 8 | 25 | 6 | 42 | 2 | 59 | 4 |
| 11 | 5 | 27 | 6 | 45 | 5 | 61 | 4 |
| 12 | 5 | 31 | 3 | 46 | 5 | 65 | 7 |
| 14 | 9 | 33 | 3 | 48 | 1 | 67 | 7 |

TABLE 5.2: DIE DETAILS

| Axis | Dimensions (mm) |
|------------------|--------------------------|
| X (in plane) | 3.0 |
| Y (in plane) | 3.0 |
| Z (out of plane) | $550 \pm 10 \mu\text{m}$ |

TABLE 5.3: NUMBER OF HEIGHT OFFSET WAFERS REQUIRED

| Die | Offset wafers | Total Height |
|-----|---------------|---------------------------|
| 1 | 0 | $0 \mu\text{m}$ |
| 2 | 1 | $550 \pm 15 \mu\text{m}$ |
| 3 | 2 | $1100 \pm 30 \mu\text{m}$ |
| 4 | 1 | $550 \pm 15 \mu\text{m}$ |
| 5 | 1 | $550 \pm 15 \mu\text{m}$ |
| 6 | 1 | $550 \pm 15 \mu\text{m}$ |
| 7 | 2 | $1100 \pm 30 \mu\text{m}$ |
| 8 | 1 | $550 \pm 15 \mu\text{m}$ |
| 9 | 0 | $0 \mu\text{m}$ |

Chapter 6

Conclusions

In this thesis, the design and MEMS implementation of a frequency independent broadband ultrasonic beamforming sensor microarray has been presented. The main advantage of the developed sensor microarray is that unlike other planar or curved sensor microarrays, this device can provide a real-time beamforming capability without any microelectronic signal processing. This unique feature enables the device to be used in applications where real-time implementation issue is crucial, for example, in automotive collision avoidance applications.

The scientific approach of the proposed research work is based on a previous work done in 1965 in England where a hyperbolic paraboloid geometry continuous aperture ultrasonic transducer has been demonstrated to provide such a beamforming capability. In this thesis, the theory of large scale continuous aperture constant beamwidth beamforming has been extended to exploit the potential of MEMS technology in realizing microscale sensors while accommodating the limitations of planar fabrication capabilities of today's' microfabrication techniques. The developed robust, high sensitivity, low power, batch fabricatable sensor microarray has the geometry of a discretized hyperbolic paraboloid surface and capacitive sensing has been used as the transduction mechanism to realize a cost-effective solution for microscale directional sound acquisition.

The discretized hyperbolic paraboloid geometry exploits the transport delay in the medium to accomplish the beamforming operation that is analogous to an electronic filter-and-sum operation by spatially distributing the sensors.

Major challenges in the research work have been: (1) development of a mathematical model

for a discretized hyperbolic paraboloid geometry and model verification, (2) sensor type selection, modeling and behavior verification, and (3) development of a fabrication procedure using standard microfabrication technology that ensures manufacturability. All of these challenges have been met with excellent results.

Initially an overview of different beamforming methods currently in use is provided. In conventional MEMS or non-MEMS based planar arrays complex microelectronic circuitry are used to enable a beamforming capability. Use of complex microelectronic circuitry makes these systems expensive to build and subject to processing time latency. The developed discretized hyperbolic paraboloid shaped sensor microarray eliminates the need for complicated processing circuitry that brings down the system cost dramatically eliminating the associated processing time. The trade off is that the array geometry becomes more complicated than the traditional planar array. To partially compensate for this, array elements of low mechanical complexity have been selected.

A generalized math model describing the behavior of the hyperbolic paraboloid geometry array was proposed. The model uses idealized point sensors to predict the main lobe size, direction and shape, as well as sidelobe positions and intensities. This model takes into account quantization effects due to the geometric approximation used to represent the hyperbolic paraboloid surface. A direct result of the geometric approximation is the imposition of a limited frequency range for the array as predicted by the synthesis theory.

Based on the math model, a methodology for defining the geometry of the array was then proposed. The proposed methodology is scale independent and is suitable for a variety of Macro/Micro/Nano fabrication technologies. The inputs to the process are the upper and lower operating frequency of the array, desired beam width, acceptable beam width variation and acceptable side lobe intensity. The output of the system is a fabrication technology independent geometry which defines the array. The defined geometry includes array sidelength, required sensing elements per axis, number of unique elevations, and the total height of the array.

Following the developed beamforming theory and design methodology, a 29×29 element array has been designed for the purpose of illustration. This array operates over the frequency range of 2.3 MHz – 5.2MHz which is a common frequency range for medical ultrasound imaging applications. Also a 3×3 element array has been designed specifically for the SOI based MEMS technology available in Alberta Nano fabrication facility. The 3×3 element array has been verified by CMC and Alberta Nano fab process engineers and is ready to be fabricated. The designed array targets the need for low latency sensors used in automotive collision avoidance systems, such as the proposed IAVSS system.

In order to complete the detailed design of the array, transducers must be designed for operation on the defined geometry. This indicates a transition from the generalized point transducer used previously to a technology specific design which is ready to be fabricated. The use of MEMS processing for fabrication sets limitations on the transducer design based on the current state-of-the-art. Limitations include fabrication related parameters and geometry limitations such as minimum feature size, maximum die size, and thin film thickness. These parameters are used to ensure successful fabrication. The geometry details, material selection and performance of the transducer elements used in the arrays were determined by using a lumped element model. Results from the lumped element analysis were verified through finite element analysis (FEA) results which are in close agreement.

Concurrent with the detailed design of the transducer was the development of a fabrication process for the 3×3 array. This included the detailed steps required to build the designed device. The fabrication process includes determination of the doping levels, etching times and chemistries, definition of the masks used for etching, array assembly details and final packaging.

The developed design methodology will enable one to tailor the MEMS sensor microarray for various other applications such as, 3-D ultrasound imaging for medical diagnostics, underwater surface mapping, avalanche detection, and many others in a cost effective and robust manner. Through the elimination of microelectronic signal processing, less power will be required in the system level as well as lower packaging and interconnection complexities. Additional information available due to broadband operation would allow more accurate characterization of detected targets.

A prototype device will be fabricated and tested as soon as a sponsor is available.

References

- [1] J. C. Chen, K. Yao, and R. E. Hudson, "Source Localization and Beamforming," *IEEE Signal Processing Magazine*, vol. 16, no. 2, pp. 30–39, March 2002.
- [2] B. D. V. Veen and K. M. Buckley, "Beamforming: A versatile approach to Spatial Filtering," *IEEE ASSP Magazine*, vol. 5, no. 2, pp. 4–24, April 1998.
- [3] A. D. George, J. Markwell, and R. Fogarty, "Real-Time Sonar Beamforming on High-Performance Distributed Computers," *Parallel Computing*, vol. 26, no. 10, pp. 1231–1252, 2000.
- [4] C. Tarran, M. Michell, and R. Howard, "Wideband Phased Array Radar with Digital Adaptive Beamforming," in *High Resolution radar and Sonar, IEE Colloquium*, vol. 1, May 1 1999, pp. 1–7.
- [5] S. Weizz and I. Proudler, "Comparing Efficient Broadband Beamforming Architectures and their Performance Trade-Offs," in *14th International Conference on Digital Signal Processing, 2002 (DSP 2002)*, vol. 1, July 1–3 2002, pp. 417–423.
- [6] T. C. Chou, "Broadband Frequency-Independent Beamforming," Master's thesis, Massachusetts Institute of Technology, 1995.
- [7] S. N. Rohr, R. C. Lind, R. J. Myers, W. A. Bauson, W. K. Kosiak, and H. Yen, "An Integrated Approach to Automotive Safety Systems," in *SAE transactions*, vol. 109, 2000, pp. 453–459.
- [8] R. Etienne-Cummings and M. Clapp, "Architecture for Source Localization with a Linear Ultrasonic Array," *The 2001 IEEE International Symposium on Circuits and Systems (ISCAS)*, vol. 3, no. 2, pp. 181–184, May 6–9 2001.
- [9] J. Weigold, T. Brosnihan, J. Bergeron, and X. Zhang, "A MEMS Condenser Microphone for Consumer Applications," in *19th IEEE International Conference on Micro Electro Mechanical Systems, 2006. MEMS 2006 Istanbul*, 22–26 January 2006, pp. 86–89.
- [10] D. Greve, J. Neumann, I. Oppenheim, S. Pessiki, and D. Ozevin, "Robust Capacitive MEMS Ultrasonics Transducers for Liquid Immersion," in *Ultrasonics, 2003 IEEE Symposium on*, vol. 1, 5–8 October 2003, pp. 2137–2140.
- [11] A. Firas, T. Myers, J. D. Fraser, S. Bose, and I. Bandyopadhyay, "Development of Piezoelectric Micromachined Ultrasonic Transducers," *Sensors and Actuators A*, vol. 111, no. 2–3, pp. 275–287, March 2004.
- [12] A. Caronti, G. Caliano, A. Lula, and M. Pappalardo, "An Accurate Model for Capacitive Micromachined Ultrasonic Transducers," *Ultrasonics, Ferroelectrics and Frequency Control, IEEE Transactions on*, vol. 49, no. 2, pp. 159–168, February 2002.

-
- [13] S. Chowdhury, "A MEMS Acoustical Sensor Array and Associated Micropackage," Ph.D. dissertation, University of Windsor, Canada, 2003.
- [14] K. A. Wong, S. Panda, and I. Laudabaum, "Curved Micromachined Ultrasonic Transducers," in *2003 IEEE Symposium on Ultrasonics, Ferroelectrics and Frequency Control*, vol. 1, October 2003, pp. 572–576.
- [15] S. Panda, C. Daft, P. Wagner, and I. Laudabaum, "Microfabricated Ultrasonic Transducer (cMUT) Probes: Imaging Advantages Over PZT Probes," in *AIUM presentation*, May 2003.
- [16] M. Mescher, K. Houston, K. Bernstein, G. Krikos, C. Jinrong, and L. Cross, "Novel MEMS Microshell Transducer Arrays for High-Resolution Underwater Acoustic Imaging Applications," *Proceedings of IEEE Sensors, 2002.*, vol. 1, pp. 541–546, 2002.
- [17] O. Clade, N. Felix, and E. Lacaze, "Linear and Curved Array with Advanced Electroacoustic and Acoustic Properties," in *2002 IEEE Ultrasonics Symposium Proceedings*, vol. 2, October 2002, pp. 1127–1130.
- [18] M. Meloche and S. Chowdhury, "A MEMS Non-Planar Constant Beamwidth Ultrasonic Sensor Microarray," in *Proceedings of NEWCAS 2006*, June 2006.
- [19] J. Morris, "Broad-band Constant Beam-width Transducers," *Journal of Sound Vibration*, vol. 1, pp. 28–36, 1964.
- [20] J. Morris, "Broad-Band Echo-Location," Ph.D. dissertation, University of Birmingham, England, 1964.
- [21] "Automotive Collision Avoidance System Field Operational Test," National Highway Traffic Safety Administration (NHTSA), Tech. Rep. DOT HS 809 600, may 2003.
- [22] W. P. Mason, "Sonics and Ultrasonics: Early History and Applications," *IEEE Transactions on Sonics and Ultrasonics*, vol. 23, no. 4, pp. 224–231, July 1976.
- [23] K. R. Erikson, F. J. Fry, and J. P. Jones, "Ultrasound in Medicine – A Review," *IEEE Transactions on Sonics and Ultrasonics*, vol. 21, no. 3, pp. 144–170, July 1974.
- [24] I. Oppenheim, A. Jain, and D. Greve, "MEMS Ultrasonic Transducers for Testing of Solids," *Ultrasonics, Ferroelectrics and Frequency Control, IEEE Transactions on*, vol. 50, no. 3, pp. 305–311, March 2003.
- [25] O. Tufte and G. Long, "Silicon Diffused Element Piezoresistive Diaphragms," *Journal of applied physics*, vol. 33, pp. 3322–3327, 1962.
- [26] S. Franssila, *Introduction to Microfabrication*. John Wiley & Sons, Ltd, 2004, reprinted February 2005.
- [27] M. Madou, *Fundamentals of Microfabrication*, 1st ed. CRC Press, 1998.
- [28] X. Nie, "Material Science of Thin Films & Coatings," 2006, class Notes From 88-590, Chapter 4.
- [29] J. G. Korvink and O. Paul, EDS., *MEMS: A Practical Guide to Design, Analysis, and Applications*. William Andrew Publishing, 2005.
- [30] S. Beeby, G. Ensell, M. Kraft, and N. White, *MEMS Mechanical Sensors*. Artech House, Inc., 2004.
-

-
- [31] Y. Mita, M. Mita, A. Tixer, J. P. Gouy, and H. Fujita, "Embedded-mask-methods for mm-scale multi-layer vertical/slanted Si structures," in *The Thirteenth Annual International Conference on Micro Electro Mechanical Systems, 2000. (MEMS2000)*, January 2000.
- [32] B. Alderman, C. M. Mann, D. P. Steenson, and J. M. Chamberlain, "Microfabrication of Channels Using an Embedded Mask in Negative Resist," *Journal of Micromechanics and Microengineering*, vol. 11, no. 6, November 2001.
- [33] S. Bly and D. Morison, "Safety Code 24 – Guidelines for the Safe Use of Ultrasound: Part II – Industrial and Commercial Applications," Health Canada, Tech. Rep. H46-2/90-158E, 1991. [Online]. Available: http://www.hc-sc.gc.ca/ewh-semt/alt_formats/hecs-sesc/pdf/pubs/radiation/safety-code.24-securite/safety-code.24-securite.e.pdf
- [34] R. Seip, B. Adamczyk, and D. Rundell, "Use of Ultrasound in Automotive Interior Occupancy Sensing: Optimum Frequency, Beamwidth, and SNR from Empirical Data," in *1999 IEEE Ultrasonics Symposium*, vol. 1, Ceasars Tahoe, NV, USA, 1999, pp. 741–752.
- [35] C. A. Balanis, *Antenna Theory*. Harper & Row, Publishers, New York, 1982, ch. 6.
- [36] J. Stewart, *Calculus: Early Transcendentals*, 5th ed. Brooks Cole, 2002.
- [37] O. Oralkan, A. S. Ergun, J. A. Johnson, M. Karaman, U. Demerci, K. Kaviani, T. H. Lee, and B. T. Khuri-Yakub, "Capacitive Micromachined Ultrasonic Transducers: Next-Generation Arrays for Acoustic Imaging?" *IEEE Transactions on Ultrasonics, Ferroelectrics and Frequency Control*, vol. 49, no. 11, pp. 1596–1610, November 2002.
- [38] T. B. Gabrielson, "Mechanical-Thermal Noise in Micromachined Acoustic and Vibration Sensors," *IEEE Transactions on Electron Devices*, vol. 40, no. 5, pp. 903–909, May 1993.
- [39] I. Laudabaum, "Surface Micromachined Capacitive Ultrasonic Transducers," *IEEE Transactions on Ultrasonics, Ferroelectrics, and Frequency Control*, vol. 45, no. 3, pp. 679–690, 1999.
- [40] S. D. Senturia, *Microsystem Design*. Kluwer Academic Publishers, 2001.
- [41] I. J. Oppenheim, A. Jian, and D. W. Greve, "Electrical Characterization of Coupled and Uncoupled MEMS Ultrasonic Transducers," *IEEE Transactions on Ultrasonics, Ferroelectrics and Frequency Control*, vol. 50, no. 3, pp. 297–304, March 2003.
- [42] P.-C. Hzu, C. Mastrangelo, and K. Wise, "A High Sensitivity Polysilicon Diaphragm Condenser Microphone," in *The Eleventh Annual International Workshop on Micro Electro Mechanical Systems, 1998 (MEMS98)*, Heidelberg, Germany, 1998, pp. 591–596.
- [43] S. Chowdhury, "Microelectromechanical (MEMS) VLSI Structures for Hearing Instruments," Master's thesis, University of Windsor, Canada, 2000.
- [44] J. Slipeenbeek, "MEMS Microphone Design," Master's thesis, University of Windsor, Canada, 2003.
- [45] R. Puers and D. Lapadatu, "Electrostatic Forces and their Effects on Capacitive Mechanical Sensors," *Physical Sensors and Actuators A*, vol. 56, no. 3, pp. 203–210, 1996.
- [46] S. Chowdhury, M. Ahmadi, and W. Miller, "A New Analytical Model for the Pull-in Voltage of Clamped Diaphragms Subject to Electrostatic Force," *Sensor Letters*, vol. 2, no. 2, pp. 106–112, June 2004.
-

-
- [47] M. Pedersen, W. Olthuis, and P. Pergveld, "On the mechanical behavior of thin perforated plates and their application in silicon condenser microphones," *Physical Sensors and Actuators A*, vol. 54, no. 1, June 1996.
- [48] R. G. Budynas, *Advanced Strength and Applied Stress Analysis*. McGraw-Hill, 1977.
- [49] F. P. Beer and E. R. J. Jr., *Mechanics of Materials*, 1st ed. McGraw-Hill, 1981.
- [50] K. F. Man, B. H. Stark, and R. Ramesham, "A Resource Handbook for MEMS Reliability," Jet Propulsion Laboratory, California Institute of Technology, Tech. Rep. JPL D-16171, Rev. A, December 1998.
- [51] A. Kaushik, H. Kahn, and A. Heuer, "Wafer-Level Mechanical Characterization of Silicon Nitride MEMS," *Microelectromechanical Systems, Journal of*, vol. 14, no. 2, pp. 359–367, April 2005.
- [52] C. Wolden, "RCA Clean," University of Mines, Colorado, Tech. Rep., November 2006. [Online]. Available: http://www.mines.edu/fs_home/cwolden/chen435/clean.htm
- [53] K. Westra, "Electron Beam and Sputter Deposition: Choosing Process Parameters," University of Alberta NanoFab, Edmonton, Tech. Rep., November 2006. [Online]. Available: http://www.nanofab.ualberta.ca/downloadable_files/processes/ChoosingSputteringETC.doc
- [54] H. Rourke, "AZ4620 Protocol," University of Alberta NanoFab, Tech. Rep., November 2006. [Online]. Available: http://www.nanofab.ualberta.ca/downloadable_files/processes/AZ4620_protocol.pdf
- [55] K. R. Williams, K. Gupta, and M. Wasilik, "Etch Rates for Micromachining Processing – Part II," *Journal of Microelectromechanical Systems*, vol. 12, no. 6, pp. 761–778, December 2003.
- [56] K. Westra, "A Deep Silicon RIE Primer: Bosch Etching of Deep Structures in Silicon," University of Alberta NanoFab, Tech. Rep., April 2002. [Online]. Available: http://www.nanofab.ualberta.ca/downloadable_files/processes/primer_DeepSiliconRIE.doc
- [57] "BOE Standard Operating Procedures," 2006, document version 0.9.
-

Appendix A

Matlab Code

A.1 Elevations Vs. Number of sensing surfaces per axis

```

% Determine Total Height and Number of Elevations
% Coded By Matthew Meloche, Oct 2006
%
% Array Height For Discrete Arrays Follows the following equation (based on
% Curve Fitting the resulting Data:
% Height = -0.5215*tiers^(-0.792)+0.3762
%
% Display a Hyperbolic Paraboloid
clear;
alpha=10*pi/180;
tiers2=3:2:21;
elevations=zeros(length(tiers2),1);
% Generate Reference Mesh
height=zeros(length(tiers2),1);
disp('M,N: tiers:height ');
for jkl = 1:length(tiers2)
    clear ZR X Y
    tiers=tiers2(jkl);
    X = -1:1/(2*tiers):1;
    Y = -1:1/(2*tiers):1;
    ZR = zeros(length(X),length(Y));
    for a=1:length(X)
        for b=1:length(Y)
            ZR(a,b)=X(a)*tan(2*alpha*Y(b))/(max(Y)-min(Y));
        end
    end
end

% Generate Tier Elevations
xinc=(max(X)-min(X))/tiers;
yinc=(max(Y)-min(Y))/tiers;
Z1=zeros(tiers,tiers);
for a=1:tiers
    for b=1:tiers
        X1(a)=xinc*(a-1)+xinc/2+min(X);
        Z1(a,b)=(xinc*(a-1)+xinc/2+min(X))*tan(2*alpha*...
            (yinc*(b-1)+yinc/2+min(Y)))/(max(Y)-min(Y));
    end
    Y1(b)=yinc*(b-1)+yinc/2+min(Y);
end

% Determine Discretized Elevation for each grid point
for a=1:length(X)
    for c=1:tiers
        if (X(a) < xinc*(c)+min(X))&&(X(a)>=(xinc*(c-1))+min(X))
            xl=c;
            break;
        end
    end
end

```

```

    end
    for b=1:length(Y)
        for c=1:tiers
            if (Y(b) < yinc*(c)+min(Y))&&(Y(b)>=(yinc*(c-1))+min(Y))
                y1=c;
                break;
            end
        end
        Z(a,b)=Z1(x1,y1);
    end
end

height(jkl)=max(max(Z))-min(min(Z));
elevations(jkl)=length(unique(round(Z*100))); % 1.0 percent accuracy
elevations2(jkl)=length(unique(round(Z*1000))); % 0.1 percent accuracy
elevations3(jkl)=length(unique(round(Z*20))); % 5.0 percent accuracy
% Angural Error - Determine distance between outermost sensor centers
% Then use array height to calculate an angle. compare to alpha.
error(jkl) = abs((alpha-atan(height(jkl)/((max(X)-min(X))-...
    2*(max(X)-min(X))/tiers))/alpha));
disp([num2str(tiers) ':\n' num2str(elevations(jkl)) ':\n' ...
    num2str(height(jkl)) ':\n' num2str(error(jkl))]);
end

MN=tiers2;

hold on;
semilogy(MN,elevations,'+b');
semilogy(MN,elevations2,'-r');
semilogy(MN,elevations3,'-k');
legend('Common_within_1%', 'Common_within_0.1%', 'Common_within_5%');
axis tight;
xlabel('Sensing_Surfaces_per_Axis');
ylabel('Total_Elevations');
title('Elevations_Vs_Sensing_Surfaces_per_Axis');

% Plot Height and Reference Line
figure
Href = ones(length(MN),1)*2*tan(alpha);
plot(MN,height,'o-b')
hold on;
plot(MN,Href,'-r')
axis tight;
ylim([0.15 0.36]);
xlabel('Sensing_Surfaces_per_Axis');
ylabel('Total_Array_Height_(In_Lambda)');
title('Total_Array_Height_vvs_Sensing_Surfaces_per_Axis');
legend('Discrete_Array','Continuous_Aperature');

```

A.2 Lumped Element Simulation

A.2.1 Numerical Example

```

%% Lumped Model Simulation.
% Version 3.2
% Matthew Meloche, Sept 06.
% This Provides lumped element model simulation of an individual diaphragm.
% It provides information on mechanical and electrical sensitivity,
% Resonant frequency, Maximum operating stress, Capacitance and pull-in
% voltages.

% Clean up workspace and command window
clc;
close all;
clear;
%% Fillout Physical Parameters for Input into Lumped Element Value Generator
% Physical Parameters:
physical.rho0 = 1.21; % Air Density
physical.eta = 17.1e-6; % Air Viscosity
physical.eps0 = 8.85e-12; % Electrical Permittivity.
physical.a = 40.0e-6; % Diaphragm Side Length
physical.omega = 2*pi*(3.75e6); % Operating Frequency in rad/sec
physical.omegaLower = 2*pi*(2.3e6); % Lower Operating Frequency
physical.omegaUpper = 2*pi*(5.2e6); % Upper Operating Frequency
physical.td = 0.15e-6; % Diaphragm Thickness
physical.dg = 0.4e-6; % Airgap Thickness
physical.tb = physical.td; % Perforated plate Thickness
physical.v = 0.35; % Poisson's Ratio of Diaphragm
physical.E = 2.90e11; % Younges Modulus of Diaphragm
physical.c = 343; % Velocity of Sound in Air
physical.rho = 3000; % Density of Diaphragm Material
physical.rbh = 1e-6; % Radius of perforated plate holes
physical.holes = 15*15; % ## of holes in Perforated Plate
physical.resStress = 250e6; % Residual Stress in Diaphragm
physical.Vb = 25.0; % Bias Voltage
physical.P = 1; % Acoustic Pressure (in Pa)
physical.elements = 1; % Elements per tier
physical.Temp = 90; % System Temperature in Celcius
%% Determine Accurate Pull-In Voltage
% Pull in voltage is determined by the S. Chowdhury method for clamped
% Diaphragms
disp('Lumped_Element_Model_Results');
disp('-----');
Vpi = PullIn(physical);
disp(['The Pull-In Voltage is:_' num2str(Vpi) '_Volts']);

%% Generate Lumped Model Parameters From Physical Parameters
% Generate Lumped model parameters from physical geometries and properties.

```

```

% Lumped Elements parameters generated are for the Mastrangelo model of a
% capacitive diaphragm.
param = genparameters(physical);

%% Generate Resonant Frequency and Steady State Response
% Determine mechanical steady state response with respect to Frequency as
% well as the undamped resonant Frequency.
[freq, Resp, Fres, Sop] = freqresponse(physical, param);
% Determine the Electrical Sensitivity as per Mastrangelo Paper.
% Express in mV/Pa
Smast = abs(mastrangelo(physical))*10^3;
% Determine Capacitance of tier based on parallel plate approximation
Cdia = (physical.eps0*physical.a^2/physical.dg)*physical.elements;
% Determine Mechanical Sensitivity and capacitance change by Puers method
Spuers = puers(physical);

% Perform Mechanical Noise Floor Calculations as per Gabrielson
NoiseFloor = noise(physical, param);

% Verify Maximum Operating stress is within Coulomb–Mohr Rupture Criteria
% as per Budynas method
stress = coulombmohr(physical);

% Generate a simple text report based on the resulting numbers.
disp(['Diaphragm_Side_Length:_' num2str(physical.a*10^3) '_mm']);
disp(['Unbiased_Tier_Capacitance:_' num2str(Cdia*10^12) '_pF']);
disp(['Resonant_Frequency:_' num2str(Fres/10^3) '_kHz']);
disp(['Maximum_Stress_in_Diaphragm_at_operating_Pressure:_' ...
      num2str(stress.max/10^6) '_MPa_(' ...
      num2str(20*log10(physical.P/(20e-6))) '_dB/SPL')']);
disp(['Coulomb–Mohr_Rupture_Limit:_' ...
      num2str(stress.rupturepressure/10^6) ...
      '_MPa_(' num2str(20*log10(stress.rupturepressure/(20e-6))) ...
      '_dB/SPL)_Safety_Factor:2_']);
disp('—_Sensitivity_Figures_—');
disp(['Mechanical_Sensitivity_by_Puers_Method:_' ...
      num2str(Spuers.Sz*10^6) ...
      '_um/N_@_' num2str(physical.omega/(2*pi*10^3)) '_kHz']);

disp(['Capacitance_Change_by_Puers_Method:_' ...
      num2str(Spuers.deltaC_AC*10^15) ...
      '_fF/Pa_@_' num2str(physical.omega/(2*pi*10^3)) '_kHz']);

disp(['Diaphragm_Total_Sensitivity_by_Resonance_Method:_' ...
      num2str(Sop*10^3) '_(mV/Pa)/element_@_' ...
      num2str(physical.omega/(10^3*2*pi)) '_kHz']);
disp(['Diaphragm_Total_Sensitivity_by_Mastrangelo_Method:_' ...
      num2str(Smast) ...

```

```

    '(mV/Pa)/element_@_' num2str(physical.omega/(10^3*2*pi)) '_kHz'];
disp(['Total Array Sensitivity predicted between:_' ...
    num2str(physical.elements*Smast*29^2) '_-' ...
    num2str(physical.elements*Sop*10^3*29^2)...
    '(mV/Pa)_@_' num2str(physical.omega/(10^3*2*pi)) '_kHz'];
disp(['The Mechanical Noise Floor at_' num2str(physical.Temp) 'C is:_' ...
    num2str(NoiseFloor) '_dB/SPL at_' ...
    num2str(physical.omega/(2*pi*10^3)) '_kHz']);
disp(['Percentage of space occupied by vent holes:_' ...
    num2str(param.alpha*100) '%']);

```

A.2.2 Array Design Simulation

```

%% Lumped Model Simulation.
% Version 3.2
% Matthew Meloche, Sept 06.
% This Provides lumped element model simulation of an individual diaphragm.
% It provides information on mechanical and electrical sensitivity,
% Resonant frequency, Maximum operating stress, Capacitance and pull-in
% voltages.

% Clean up workspace and command window
clc;
close all;
clear;
%% Fillout Physical Parameters for Input into Lumped Element Value Generator
% Physical Parameters:
physical.rho0 = 1.21; % Air Density
physical.eta = 17.1e-6; % Air Viscosity
physical.eps0 = 8.85e-12; % Electrical Permittivity.
physical.a = 0.3e-3; % Diaphragm Side Length
physical.omega = 2*pi*(140e3); % Operating Frequency in rad/sec
physical.omegaLower = 2*pi*(80e3); % Lower Operating Frequency
physical.omegaUpper = 2*pi*(200e3); % Upper Operating Frequency
physical.td = 2e-6; % Diaphragm Thickness
physical.dg = 1e-6; % Airgap Thickness
physical.tb = physical.td; % Perforated plate Thickness
physical.v = 0.35; % Poisson's Ratio of Diaphragm
physical.E = 1.60e11; % Younges Modulus of Diaphragm
physical.c = 343; % Velocity of Sound in Air
physical.rho = 2300; % Density of Diaphragm Material
physical.rbh = 10e-6; % Radius of perforated plate holes
physical.holes = 8*8; % ## of holes in Perforated Plate
physical.resStress = 30e6; % Residual Stress in Diaphragm
physical.Vb = 12.0; % Bias Voltage
physical.P = 1; % Acoustic Pressure (in Pa)
physical.elements = 8*8; % Elements per tier
physical.Temp = 90; % System Temperature in Celcius
%% Determine Accurate Pull-In Voltage
% Pull in voltage is determined by the S. Chowdhury method for clamped

```

```

% Diaphragms
disp('Lumped_Element_Model_Results ');
disp('-----');
Vpi = PullIn(physical);
disp(['The Pull-In Voltage is: ' num2str(Vpi) ' Volts']);

%% Generate Lumped Model Parameters From Physical Parameters
% Generate Lumped model parameters from physical geometries and properties.
% Lumped Elements parameters generated are for the Mastrangelo model of a
% capacitive sensor.
param = genparameters(physical);

%% Generate Resonant Frequency and Steady State Response
% Determine mechanical steady state response with respect to Frequency as
% well as the undamped resonant Frequency.
[freq, Resp, Fres, Sop] = freqresponse(physical, param);
% Determine the Electrical Sensitivity as per Mastrangelo Paper.
% Express in mV/Pa
Smast = abs(mastrangelo(physical))*10^3;
% Determine Capacitance of tier based on parallel plate approximation
Cdia = (physical.eps0*physical.a^2/physical.dg)*physical.elements;
% Determine Mechanical Sensitivity and capacitance change by Puers method
Spuers = puers(physical);

% Perform Mechanical Noise Floor Calculations as per Gabrielson
NoiseFloor = noise(physical, param);

% Verify Maximum Operating stress is within Coulomb-Mohr Rupture Criteria
% as per Budynas method
stress = coulombmohr(physical);

% Generate a simple text report based on the resulting numbers.
disp(['Diaphragm Side Length: ' num2str(physical.a*10^3) ' um']);
disp(['Unbiased Tier Capacitance: ' num2str(Cdia*10^12) ' pF']);
disp(['Resonant Frequency: ' num2str(Fres/10^3) ' kHz']);
disp(['Maximum Stress in Diaphragm at operating Pressure: ' ...
      num2str(stress.max/10^6) ' MPa (' ...
      num2str(20*log10(physical.P/(20e-6))) ' dB/SPL)']);
disp(['Coulomb-Mohr Rupture Limit: ' ...
      num2str(stress.rupturepressure/10^6) ...
      ' MPa (' num2str(20*log10(stress.rupturepressure/(20e-6))) ...
      ' dB/SPL) Safety Factor: 2']);
disp('--- Sensitivity Figures ---');
disp(['Mechanical Sensitivity by Puers Method: ' ...
      num2str(Spuers.Sz*10^6) ...
      ' um/N @ ' num2str(physical.omega/(2*pi*10^3)) ' kHz']);

disp(['Capacitance Change by Puers Method: ' ...

```

```

num2str(Spuers.deltaC_AC*10^15) ...
'_fF/Pa_@_' num2str(physical.omega/(2*pi*10^3)) '_kHz']);

disp(['Diaphragm_Total_Sensitivity_by_Resonance_Method:_' ...
num2str(Sop*10^3) '(mV/Pa)/element_@_' ...
num2str(physical.omega/(10^3*2*pi)) '_kHz']);
disp(['Diaphragm_Total_Sensitivity_by_Mastrangelo_Method:_' ...
num2str(Smast) ...
'(mV/Pa)/element_@_' num2str(physical.omega/(10^3*2*pi)) '_kHz']);
disp(['Tier_Total_Sensitivity_predicted_between:_' ...
num2str(physical.elements*Smast) '_-' ...
num2str(physical.elements*Sop*10^3)...
'(mV/Pa)_@_' num2str(physical.omega/(10^3*2*pi)) '_kHz']);
disp(['The_Mechanical_Noise_Floor_at_' num2str(physical.Temp) 'C_is:_' ...
num2str(NoiseFloor) '_dB/SPL_at_' ...
num2str(physical.omega/(2*pi*10^3)) '_kHz']);
disp(['Percentage_of_space_occupied_by_vent_holes:_' ...
num2str(param.alpha*100) '%']);

```

A.2.3 Support Functions

```

function [f,S,fres,Sop] = freqresponse(physical,param)
%% Derive Lumped Parameters from Physical Data
% This code takes reduced structural data and lumped element data for a
% clamped square diaphragm and calculates the steady state frequency
% response as well as The first resonant Frequency.
% Coded July 06, Matthew Meloche.
%
% Based on the model Presented by Mastrangelo
%

% Calculate The Undamped Resonant Frequency
rho1 = 1/(physical.rho*physical.td);
T = physical.resStress*physical.td;
D = physical.E*physical.td^3/(12*(1-physical.v^2));
TT = D*pi^2/physical.a^4+T/(2*physical.a^2);
% Undamped Resonant Frequency.
fres.undamped = sqrt(rho1*TT);

% Generate response at 2000 points in the specified frequency range
f = physical.omegaLower:(physical.omegaUpper-physical.omegaLower)/2000:...
physical.omegaUpper;

% Generate Equivalent Impedances for steady state mechanical analysis
Zt = zeros(length(f),1);
S = zeros(length(f),1);
for a=1:length(f)
w=f(a);
physical.omega=w;
param=genparameters(physical);

```

```

    Zt(a) = param.Rr+(j*w)*(param.Mm+param.Mr)+1./(j*w*param.Cm)+...
            (param.Rg+param.Rh)./(1+j*w*(param.Rg+param.Rh)*param.Ca);
    S(a) = physical.Vb.*physical.a^2./(j*w*physical.dg.*Zt(a));
end

% Estimate Damped Resonant Frequency (Within sampled Range)
mm = max(S);
for a=1:length(S)
    if (S(a) == mm)
        break;
    end
end
% If a local maxima cannot be found within the sampled frequency range,
% then assume the resonant frequency exists outside the sampled range,
% return the undamped resonant frequency instead of the damped frequency.
if (a == length(S)) || (a == 1)
    fres = fres_undamped;
else
    fres = f(a);
end

% Find the index closest to the operating frequency to determine the steady
% state mechanical sensitivity.
err = 1e8;
for a=1:length(f)
    if (abs(physical.omega-f(a)) < err)
        hit = a;
        err = abs(physical.omega-f(a));
    end
end
Sop = abs(S(hit));

end

function S = mastrangelo(physical)
% Generate Combined Sensitivity for steady state operation based on
% Mastrangelo method.

% Generate parameters
param = genparameters(physical);

% Determine Diaphragm Impedance at operating Frequency
Zt = param.Rr + i*physical.omega*(param.Mm + param.Mr) + ...
    1/(i*physical.omega*param.Cm) + (param.Rg+param.Rh)/(1 +...
    i*physical.omega*(param.Rg+param.Rh)*param.Ca);

% Determine Sensitivity at operating Frequency
S = (physical.Vb*physical.a^2)/(i*physical.omega*physical.dg*Zt);

function Vpi = PullIn(physical)

```

```

% Accurately Determine Pull-In Voltage based on S. Chowdhury method for
% clamped square diaphragms.

% Fitting Parameters for Clamped Diaphragm
C1 = 3.45;
C2 = 1.994*(1-0.271*physical.v)/(1-physical.v);
Eeff = physical.E/(1-physical.v^2);

% Determine Pull In Voltage.
Vpi = sqrt( (6*physical.dg^2/(5*physical.eps0)) * (...
    (C1*physical.td*physical.resStress/(physical.a/2)^2)*physical.dg/3 ...
    + C2*physical.td*Eeff/(physical.a/2)^4*(physical.dg/3)^3 ) );

% Check for a Bias Voltage which exceeds the pull-in Voltage and print a
% warning if Bias is too high.
if (Vpi < physical.Vb)
    disp('---WARNING---Bias Exceeds Pull In Voltage!! ---');
end
end

function stress = coulombmohr(physical)
% Determine if the structure exists within the coulomb-mohr criteria for
% brittle rupture.
% Maximum stress for a supported square diaphragm. From "Advanced Strength
% and applied stress" by Richard G. Budynas, 1977 p.137
% Coded By: Matthew Meloche, Sept 06

% Determine the maximum operating stress
stress.max = 0.287*physical.P*(physical.a/physical.td)^2;

% Determine the rupture pressure for this diaphragm
% Derate to 50% for safety factor
sigma = physical.E*.5;
stress.rupturepressure = sigma/(0.287*(physical.a/physical.td)^2);

% Check to ensure we are operating within the rupture limit.
if stress.max > stress.rupturepressure
    disp('---CRITICAL---Structure will Rupture at operating Pressure');
end

function param = genparameters(physical)
%% Derive Lumped Parameters from Physical Data
% This code takes dimensional and structural data from a diaphragm and
% reduces it to lumped model values for simulation. This file accepts the
% struct physical from the calling function.
% Coded July 06, Matthew Meloche.
%
% Based on the model Presented in the Masters Thesis of S. Chowdhury and
% J. Sliepenbeek From Mastrangelo Paper (1998 MEMS Condrence, Heidelberg)
%

```

```

% Physical Data Structure Elements:
% physical.rho0      - Air Density
% physical.eta      - Air Viscosity
% physical.eps0     - Electrical Permittivity.
% physical.a        - Diaphragm Side Length
% physical.omega    - Operating Frequency in rad/sec
% physical.omegaLower - Lower Operating Frequency
% physical.omegaUpper - Upper Operating Frequency
% physical.td       - Diaphragm Thickness
% physical.dg       - Airgap Thickness
% physical.tb       - Perforated plate Thickness
% physical.v        - Poisson's Ratio of Diaphragm
% physical.E        - Younges Modulus of Diaphragm
% physical.c        - Velocity of Sound in Air
% physical.rho      - Density of Diaphragm Material
% physical.rbh      - Radius of perforated plate holes
% physical.holes    - ## of holes in Perforated Plate
% physical.resStress - Residual Stress in Diaphragm
% physical.Vb       - Bias Voltage
% physical.P        - Acoustic Pressure (in Pa)
% physical.elements - Elements per tier
% physical.Temp     - System Temperature in Celcius

%% Start Calculations
% Radiative Resistance and Radiative Mass (M. Thesis, S. Chowdury)
param.Rr = physical.rho0*physical.a.^4*physical.omega.^2/(2*pi*physical.c);
param.Mr = 8*physical.rho0*physical.a.^3/(3*pi*sqrt(pi));

% Mechanical Spring Constant and Mechanical Mass (M. Thesis, S. Chowdury)
rho = physical.rho*physical.td;
T = physical.resStress*physical.td;
D = physical.E*physical.td^3/(12*(1-physical.v^2));
param.Cm = 32*physical.a^2/(pi^6*(2*pi^2*D+physical.a^2*T));
param.Mm = (pi^4*rho*(2*pi^2*D+physical.a^2*T))/(64*T);

% Perforated Plate damping (M. Thesis, S. Chowdury)
AAT = physical.holes*physical.rbh^2;
alpha = AAT/physical.a^2;
param.alpha = alpha;
n = physical.holes/physical.a^2;
param.Rg = 12*physical.eta*physical.a^2/(n*physical.dg^3*pi)*...
(alpha/2-alpha^2/8-log(alpha)/4-3/8);
param.Rh = 8*physical.eta*physical.tb*physical.a^2/(pi*n*physical.rbh^4);

% Spring Constant of Air in Diaphragm (M. Thesis, S. Chowdury)
param.Ca = physical.dg/(physical.rho0*physical.c^2*alpha^2*physical.a^2);

end

function nfloordB = noise(physical,param)

```

```

% Calculate The mechanical noise floor
% From "Mechanical-Thermal Noise in micromachined Acoustic and Vibration
% Sensors" by Thomas B. Gabrielson
% Coded By Matthew Meloche, Aug 06

% Boltzman Constant
kb = 1.38e-23;
% Mechanical Resistance (Damping)
R = param.Rg+param.Rh;

Rac = R/(physical.a^2)^2;
% Cut off frequency
fc = physical.omega/(2*pi);
dFc = pi/2*fc;
% Noise Pressure from damping sources
p = sqrt(4*kb*(physical.Temp+273.15)*Rac*dFc);
% Mechanical Noise Floor in dB/spl
nfloordB = 20*log10(p/20e-6);

function S = puers(physical)
% Generate Mechanical and Electrical Sensitivities, mechanical Forces and
% Capacitance changes based on the Puers method.
% Coded by: Matthew Meloche, Aug 06.

% Generate lumped model parameters.
param = genparameters(physical);

% Determine Mechanical Sensitivity. (m/N)
% Fz = kz*z --> z/Fz = 1/kz --> Sz = 1/kz
S.Sz = 1/(1/param.Ca+1/param.Cm);
% Typical Values - 0.01 and 0.5 um/uN

% Determine The Mechanical force and the Effective Biased Displacement
K = 1/param.Cm+1/param.Ca;

% Manipulate Eqn. 9 and 2 to solve for Fz & Zm (Solve for Zm first)
CoEff = [2*K -4*K*physical.dg 2*K*physical.dg^2 -physical.eps0*...
physical.Vb^2*physical.a^2];
rts = roots(CoEff);
% find the largest stable root of the equation to Determine Zm.
% (Iterate through roots, find the largest root larger then 1/3*Vcritical)
Err= 1e20;
for a = 1:length(rts)
    if (abs(rts(a)) > 0)&&(abs(rts(a)) < 1/3*physical.dg)&& ...
        (1/3*physical.dg - abs(rts(a)) < Err)
        Err = 1/3*physical.dg-abs(rts(a));
        index=a;
    end
end
end

```

```

Zm = rts(index);
Fe = K*Zm;

% Determine Total Operating Capacitance Change
Fm = physical.P*physical.a^2;
S.deltaC_AC = physical.eps0*physical.a^2*S.Sz*(Fe+Fm)/physical.dg^2;
%
% Determine Puers Mechanical Sensitivity for DC
K = 1/param.Cm;
S.Sz_DC = param.Cm;
% Manipulate Eqn. 9 and 2 to solve for Fz & Zm (Solve for Zm first)
CoEff = [2*K -4*K*physical.dg 2*K*physical.dg^2 - ...
         physical.eps0*physical.Vb^2*physical.a^2];
rts = roots(CoEff);
% find the largest stable root of the equation to Determine Zm.
Err= 1e20;
index=1000;
for a = 1:length(rts)
    if (abs(rts(a)) > 0)&&(abs(rts(a)) < 1/3*physical.dg)&& ...
        (1/3*physical.dg - abs(rts(a)) < Err)
        Err = 1/3*physical.dg-abs(rts(a));
        index=a;
    end
end
if index==1000
    disp('WARNING--_ROOT_NOT_FOUND')
    index=1;
end
% Set Appropriate root to the impedance, and determine electrical force
% based on this spring value.
Zm = rts(index);
Fe = K*Zm;

% Determine Capacitance Change From Bias Displacement
S.deltaC_DC = physical.eps0*physical.a^2*S.Sz*Fe/physical.dg^2;
% Determine Total Operating Capacitance Change
Fm = physical.P*physical.a^2;
S.deltaC_static = physical.eps0*physical.a^2*S.Sz*(Fe+Fm)/physical.dg^2;
% Approximate Pull-in Voltage
S.Vcr = sqrt(8*physical.dg^3/(27*physical.eps0*physical.a^2*S.Sz));

```

A.3 Mainlobe -3dB Cross-Section Generation

```

% -6 dB Contour generator for Discrete Hyperbolic Paraboloid Array Factors
% Coded By: Matthew Meloche, Oct. 2006
%
% Setup Array Parameters
disp('Initializing...')
tstart = cputime();

```

```

theta = -20*pi/180:1*pi/180:20*pi/180;      % Solid Arc Under Investigation
phi = -20*pi/180:1*pi/180:20*pi/180;
a = 10 * pi/180;

Disc3=zeros(length(theta),length(phi));
Disc5=zeros(length(theta),length(phi));
Disc9=zeros(length(theta),length(phi));
Disc15=zeros(length(theta),length(phi));
Disc21=zeros(length(theta),length(phi));
Disc35=zeros(length(theta),length(phi));

disp('Generating Data')
% -----
% Generate the First Data Set, M,N (Tiers) = 35 - Simulates Continuous
% behaviour
L = 3;
Y = 3;
for m=1:length(theta)
    for n=1:length(phi)
        Disc3(m,n)=DiscSens(theta(m),phi(n),L,Y,a,35);
    end
end
% -----
% Generate the Second Data Set, M,N (Tiers) = 35 - Simulates Continuous
% behaviour
L=5;
Y=5;
for m=1:length(theta)
    for n=1:length(phi)
        Disc5(m,n)=DiscSens(theta(m),phi(n),L,Y,a,35);
    end
end
% -----
% Generate the Third Data Set, M,N (Tiers) = 35 - Simulates Continuous
% behaviour
L=9;
Y=9;
for m=1:length(theta)
    for n=1:length(phi)
        Disc9(m,n)=DiscSens(theta(m),phi(n),L,Y,a,35);
    end
end
% -----
% Generate the Fourth Data Set, M,N (Tiers) = 35 - Simulates Continuous
% behaviour
L=15;
Y=15;
for m=1:length(theta)
    for n=1:length(phi)

```

```

        Disc15(m,n)=DiscSens(theta(m),phi(n),L,Y,a,35);
    end
end
% -----
% Generate the Fifth Data Set, M,N (Tiers) = 35 - Simulates Continuous
% behaviour
L=21;
Y=21;
for m=1:length(theta)
    for n=1:length(phi)
        Disc21(m,n)=DiscSens(theta(m),phi(n),L,Y,a,35);
    end
end
% -----
% Generate the Sixth Data Set, M,N (Tiers) = 35 - Simulates Continuous
% behaviour
L=35;
Y=35;
for m=1:length(theta)
    for n=1:length(phi)
        Disc35(m,n)=DiscSens(theta(m),phi(n),L,Y,a,35);
    end
end

disp('Normalizing_and_Converting_Results_to_dB');
Disc3=10*log10(Disc3/max(max(Disc3)));
Disc5=10*log10(Disc5/max(max(Disc5)));
Disc9=10*log10(Disc9/max(max(Disc9)));
Disc15=10*log10(Disc15/max(max(Disc15)));
Disc21=10*log10(Disc21/max(max(Disc21)));
Disc35=10*log10(Disc35/max(max(Disc35)));
disp('Plotting_Results');
figure;
hold on;
[C,H]=contour(theta*180/pi,phi*180/pi,Disc3,[-6,-6]);
set(H,'linecolor','r');
[C,H]=contour(theta*180/pi,phi*180/pi,Disc5,[-6,-6]);
set(H,'linecolor','g');
[C,H]=contour(theta*180/pi,phi*180/pi,Disc9,[-6,-6]);
set(H,'linecolor','b');
[C,H]=contour(theta*180/pi,phi*180/pi,Disc15,[-6,-6]);
set(H,'linecolor','k');
[C,H]=contour(theta*180/pi,phi*180/pi,Disc21,[-6,-6]);
set(H,'linecolor','c');
[C,H]=contour(theta*180/pi,phi*180/pi,Disc35,[-6,-6]);
set(H,'linecolor','m');
legend('3_Lambda', '5_Lambda', '9_Lambda', '15_Lambda', '21_Lambda', ...
    '35_Lambda');
xlabel('Theta_(in_Degrees)');

```

```
ylabel('Phi_(in_Degrees)');
axis square;
```

A.3.1 Support Functions

```
function sens = SensWallApprox(theta, phi, L, Y, alpha)
% Continuous sensitivity function for a small alpha twisted transducer.
% Approximations have been made to limit alpha to 'small' values (~<10 deg)
% Usage:
% sens = SensWallApprox(theta, phi, L, Y, alpha)
% theta - angle off broadside in the xz plane in radians
%         (measured from the z axis)
% phi    - angle off broadside in the yz plane in radians
%         (measured from the z axis)
% L      - Length of the Array in wavelengths
% Y      - Height of the Array in wavelengths
% alpha  - transducer twist in radians

sens = 1/(L)*quad(@(x) exp(i*2*pi*x*tan(theta)).*(...
    sin(pi*Y*(tan(phi)+x*2*alpha/L)) ...
    ./((pi*Y*(tan(phi)+eps)+x*2*alpha/L))), -L/2, L/2);
```

A.4 Accuracy of Summation Vs. Integral form

```
% Integral VS. Summation calculation.
% Determine the Error present in the approximate Summation of the Morris
% Equation
clear
% Setup Array Parameters
tstart = cputime();
L = 5;
Y = 5;
theta = -20*pi/180:1*pi/180:20*pi/180;
phi = -20*pi/180:1*pi/180:20*pi/180;
a = 10 * pi/180;

% Iterate Through Original Equation And Determine Response
disp('Starting_Continuous_Calculations');
SensC = zeros(length(theta), length(phi));
for m = 1:length(theta)
    for n = 1:length(phi)
        SensC(m, n) = SensWallApprox(theta(m), phi(n), L, Y, a);
    end
end
end
SensC = SensC / max(max(SensC));

% Iterate Through Discrete Equation And Determine Response
Disc3 = zeros(length(theta), length(phi));
Disc5 = zeros(length(theta), length(phi));
Disc7 = zeros(length(theta), length(phi));
```

```

Disc15= zeros(length(theta),length(phi));
Disc21= zeros(length(theta),length(phi));
Disc35= zeros(length(theta),length(phi));
disp('Starting_Discrete_Calculations');
for m=1:length(theta)
    for n=1:length(phi)
        Disc3(m,n)=DiscSens(theta(m),phi(n),L,Y,a,3);
        Disc5(m,n)=DiscSens(theta(m),phi(n),L,Y,a,5);
        Disc7(m,n)=DiscSens(theta(m),phi(n),L,Y,a,7);
        Disc15(m,n)=DiscSens(theta(m),phi(n),L,Y,a,15);
        Disc21(m,n)=DiscSens(theta(m),phi(n),L,Y,a,21);
        Disc35(m,n)=DiscSens(theta(m),phi(n),L,Y,a,35);
    end
end

disp('Normalizing_Results');
Disc3=Disc3/max(max(Disc3));
Disc5=Disc5/max(max(Disc5));
Disc7=Disc7/max(max(Disc7));
Disc15=Disc15/max(max(Disc15));
Disc21=Disc21/max(max(Disc21));
Disc35=Disc35/max(max(Disc35));

disp('Calculating_Error');
aveError3=mean(mean(abs(Disc3-SensC)))/max(max(abs(Disc3)));
aveError5=mean(mean(abs(Disc5-SensC)))/max(max(abs(Disc5)));
aveError7=mean(mean(abs(Disc7-SensC)))/max(max(abs(Disc7)));
aveError15=mean(mean(abs(Disc15-SensC)))/max(max(abs(Disc15)));
aveError21=mean(mean(abs(Disc21-SensC)))/max(max(abs(Disc21)));
aveError35=mean(mean(abs(Disc35-SensC)))/max(max(abs(Disc35)));

MaxError3=max(max(abs(Disc3-SensC)))/max(max(abs(Disc3)));
MaxError5=max(max(abs(Disc5-SensC)))/max(max(abs(Disc5)));
MaxError7=max(max(abs(Disc7-SensC)))/max(max(abs(Disc7)));
MaxError15=max(max(abs(Disc15-SensC)))/max(max(abs(Disc15)));
MaxError21=max(max(abs(Disc21-SensC)))/max(max(abs(Disc21)));
MaxError35=max(max(abs(Disc35-SensC)))/max(max(abs(Disc35)));

AveError=[aveError3 aveError5 aveError7 aveError15 aveError21 aveError35];
MaxError=[MaxError3 MaxError5 MaxError7 MaxError15 MaxError21 MaxError35];
tiers=[3 5 7 15 21 35];

subplot(2,1,1),plot(tiers,AveError*100)
title('Average_Error');
xlabel('Number_of_Tiers');
ylabel('Percent_Error');
subplot(2,1,2),plot(tiers,MaxError*100)
title('Maximum_Error');
xlabel('Number_of_Tiers');

```

```

ylabel('Percent_Error');

figure
subplot(1,2,1),mesh(phi*180/pi,theta*180/pi,SensC);
axis square;
title('Continuous_Structure');
xlabel('theta');
ylabel('phi');

subplot(1,2,2),mesh(phi*180/pi,theta*180/pi,Disc3);
axis square;
title('3_Tier_Structure');
xlabel('theta');
ylabel('phi');

```

A.4.1 Support Functions

```

function sens = SensWallApprox(theta,phi,L,Y,alpha)
% Continuous sensitivity function for a small alpha twisted transducer.
% Approximations have been made to limit alpha to 'small' values (~<10 deg)
% Usage:
% sens = SensWallApprox(theta,phi,L,Y,alpha)
% theta - angle off broadside in the xz plane in radians
%         (measured from the z axis)
% phi    - angle off broadside in the yz plane in radians
%         (measured from the z axis)
% L      - Length of the Array in wavelengths
% Y      - Height of the Array in wavelengths
% alpha  - transducer twist in radians

sens = 1/(L)*quad(@(x) exp(i*2*pi*x*tan(theta)).*(...
    sin(pi*Y*(tan(phi)+x*2*alpha/L))./(pi*Y*(tan(phi+eps)+x*2*alpha/L))),-L/2,L/2);

function sens = DiscSens(theta,phi,L,Y,alpha,tiers)
% Discrete sensitivity function for a small alpha twisted transducer.
% Approximations have been made to limit alpha to 'small' values (~<10 deg)
% Usage:
% sens = DiscSens(theta,phi,L,Y,alpha,tiers)
% theta - angle off broadside in the xz plane in radians
%         (measured from the z axis)
% phi    - angle off broadside in the yz plane in radians
%         (measured from the z axis)
% L      - Length of the Array in wavelengths
% Y      - Height of the Array in wavelengths
% alpha  - transducer twist in radians
% tiers  - Number of tiers per axis

sens=0;
N=1/sqrt(tan(theta)^2+tan(phi)^2+1);
for m=1:tiers

```

```

    for n=1:tiers
        sens=sens+exp(i*2*pi*N*((-L/2+m*L/tiers)*tan(theta) + ...
            (-Y/2+n*Y/tiers)*tan(phi) + 2*alpha*(-L/2+m*L/tiers)*...
            (-Y/2+n*Y/tiers)/L));
    end
end
sens=sens/tiers^2;

```

A.5 Generation of Polar Plots

```

% New Array Beamshape Generator.
% Uses the ULTRA SLOW double integral form of the array factor.
% (no Simplification for best accuracy)

```

```

% 3 Lambda Sidelength. 10 degree out of plane twist

```

```

ML=3:0.1:5;

```

```

MY=3:0.1:5;

```

```

alpha=10/180*pi;

```

```

tiers=9;

```

```

pSide = 0;

```

```

theta=(-180:2:180)/180*pi;

```

```

phi = (0:1:0)/180*pi;

```

```

pMain=zeros(length(ML),1);

```

```

for index=1:length(ML)

```

```

    L=ML(index)

```

```

    Y=MY(index);

```

```

    Z = zeros(length(theta),length(phi));

```

```

    for a = 1:length(theta)

```

```

        for b = 1:length(phi)

```

```

            Z(a,b)=DiscSens(theta(a),phi(b),L,Y,alpha,tiers);

```

```

        end

```

```

    end

```

```

% Normalize

```

```

Z=Z/max(max(Z));

```

```

% Calculate percentage power in main lobe:

```

```

% Find Total Power between -90 -> +90 degrees

```

```

ledge= nmatch(theta,-pi/2);

```

```

redge= nmatch(theta,pi/2);

```

```

ptheta=theta(ledge:redge);

```

```

pZ=Z(ledge:redge);

```

```

pTotal(index)=trapz(ptheta,abs(pZ));

```

```

% Find power in main lobe (between +alpha and -alpha)
clear ptheta pZ
ledge= nmatch(theta,-alpha);
redge= nmatch(theta,alpha);
ptheta=theta(ledge:redge);
pZ =Z(ledge:redge);

pMain(index) =trapz(ptheta,abs(pZ));

%Determine total Power in Sidelobes
pSide(index) = 1 - abs(pMain(index))/abs(pTotal(index));

end

plot(ML,pSide)
xlabel('Array_Sidelength')
ylabel('Sidelobe_Power_(%)');
title(['Array_Sidelobe_Power:_ ' num2str(tiers) '_Tiers'])

disp(['Maximum_Operating_Frequency_for_' num2str(tiers) ' ...
      '_tier_array_is_' num2str(L-1) '_lambda']);
% Plot The results.
figure
mmpolar(theta',abs(Z)) % 'style','compass'
mmpolar('TTickValue',[350,10,90,270,45,315,170,190,135,225]);
mmpolar('RTickValue',[0.5012,0.2512]);

```

A.5.1 Support Functions

```

% Find Nearest Matching Value
function k = nmatch(source, target)
err=realmax;
for a= 1:length(source)
    if err>abs(source(a)-target)
        k=a;
        err=abs(source(a)-target);
    end
end
end

```

VITA AUCTORIS

Matthew Meloche was born in 1981 in Windsor, Ontario. He graduated from St. Thomas of Villanova High School in 2000. From there he went on to the University of Windsor where he obtained a B.A.Sc. in 2004. He is currently a candidate for the Master's degree in Applied Science at the University of Windsor and hopes to graduate in Summer 2007.